

博士論文

Optical Study of Magnetoelectric Coupling in
Antiferromagnetic MnTiO_3

(反強磁性体 MnTiO_3 における電気磁気結合の光学的研究)

佐藤 樹

Preface

Coupling between electric and magnetic properties of matters has long been one of the central issues in the field of solid state physics. The microscopic origin of this cross coupling is traceable to the fact that the single particle, i.e. electron, hosts both a charge and a magnetic moment. Besides the scientific interest, the engineering of such cross coupling in materials can lead to development the era-defining functional devices as shown by examples of modern magnetic storage and sensors where the various kinds of magnetoresistance effects in metals are employed.

In insulators, such cross coupling is observed as magnetoelectric effects, where electric polarization is induced by magnetic fields and magnetization by electric fields. The magnetoelectric effect offers a clue to control and visualize antiferromagnetic domains, both of which are made difficult by the absence of magnetization in antiferromagnets. It has been shown in numerous researches that two distinct antiferromagnetic states characterized by different values of electric polarization of magnetic origin are switchable by electric fields. Furthermore, magnetoelectric effects in optical frequencies lead to the interference between electric and magnetic fields of light and hence enable us to optically distinguish two antiferromagnetic states according to whether electric and magnetic fields interfere with each other constructively or destructively. Imaging studies of switching dynamics of antiferromagnetic domains in magnetoelectric insulators should provide us significant insight, which is otherwise entirely inaccessible, into dynamic properties of antiferromagnetic domains.

In this thesis, we investigate dynamic aspects of magnetoelectric effects in a collinear antiferromagnet by means of spectroscopic and imaging experiments. We show that antiferromagnetic ordering with no magnetization surely induces the nonreciprocal optical effect in visible range. Exploiting the observed magnetoelectric optical effect, we unveil dynamic properties of antiferromagnetic domain patterns in driving electric and magnetic fields by the visualization of antiferromagnetic domain patterns in the transient state of the switching process.

This thesis is organized as follows. In Ch. 1, we first introduce background knowledge about magnetoelectric effects and then state the purposes of this research. Chapter 2 is dedicated to the experimental methods. Chapters 3-5 are devoted to the findings of this thesis. In these chapters, results and discussion are shown after the brief introduction of previous researches on the topics. In Ch. 3, we introduce the target material MnTiO_3 and then present the findings about the nonreciprocal optical effects. In Ch. 4, we demonstrate the antiferromagnetic domain

imaging technique based on the optical effect studied in the previous chapter. In Ch. 5, we investigate the switching dynamics in MnTiO_3 by the direct observation of the transient states. The conclusions are drawn in Ch. 6.

Contents

1	Background	1
1.1	Introduction to magnetoelectric effect	1
1.1.1	Linear magnetoelectric effect	1
1.1.2	Example materials	3
1.1.3	Microscopic origin of ME effects	7
1.2	Application of magnetoelectric effects	9
1.2.1	Optical magnetoelectric coupling	9
1.2.2	Electric-field control of antiferromagnetic structure	11
1.3	Research purpose	13
2	Experimental Methods	15
2.1	Sample preparation	15
2.2	Magnetization and electric polarization measurements	16
2.3	Optical measurements	17
3	Magneto-chiral Dichroism in MnTiO_3	21
3.1	Introduction to magneto-chiral dichroism	21
3.1.1	Theory	21
3.1.2	Experiment	24
3.2	Introduction to MnTiO_3	26
3.2.1	Crystal structure	26
3.2.2	Magnetic structure	26
3.2.3	Magnetoelectric coupling	27
3.3	Results and discussion	29
3.3.1	In-plane magnetoelectric coupling and polarization switching	29
3.3.2	Observation of magneto-chiral dichroism	30
3.3.3	Microscopic origin of MCHD in MnTiO_3	36
3.4	Summary	39
4	Magneto-chiral Imaging of Antiferromagnetic Domain in MnTiO_3	41
4.1	Introduction to antiferromagnetic domain imaging	41
4.1.1	Orientational and antiphase domains	41

4.1.2	Antiferromagnetic-domain imaging techniques	43
4.2	Results and discussion	47
4.3	Summary	51
5	Imaging Study of Magnetoelectric Domain Reversal	53
5.1	Introduction to switching dynamics in ferroic materials	53
5.1.1	Temporal evolution of switched areas	53
5.1.2	Domain-wall velocity in driving fields	56
5.2	Results and discussion	59
5.2.1	Quasistatic domain reversal	59
5.2.2	Dynamic domain reversal	62
5.3	Summary	69
6	Conclusion	71
A	Processing for obtaining difference images	75
B	Possible microscopic descriptions of the toroidal moment in MnTiO_3	79
C	Axial degree of freedom in MnTiO_3	85

Chapter 1

Background

1.1 Introduction to magnetoelectric effect

1.1.1 Linear magnetoelectric effect

Consideration of free energy

Magnetoelectric (ME) effects are electric induction of magnetization \mathbf{M} and magnetic induction of electric polarization \mathbf{P} . Macroscopically, \mathbf{M} (\mathbf{P}) is calculated from the magnetic-field \mathbf{H} (electric-field \mathbf{E}) derivative of the free energy function \mathcal{F} as

$$\mathbf{P} = -\frac{\partial \mathcal{F}}{\partial \mathbf{E}}, \quad (1.1)$$

$$\mathbf{M} = -\frac{\partial \mathcal{F}}{\partial \mathbf{H}}. \quad (1.2)$$

\mathcal{F} is expanded in terms of external fields \mathbf{E} and \mathbf{H} as

$$\mathcal{F}(\mathbf{E}, \mathbf{H}) = \mathcal{F}_0 - \mathbf{P}_0 \cdot \mathbf{E} - \mathbf{M}_0 \cdot \mathbf{H} - \frac{1}{2} \sum_{\mu\nu} \chi_{\mu\nu}^e E_\mu E_\nu - \frac{1}{2} \sum_{\mu\nu} \chi_{\mu\nu}^m H_\mu H_\nu - \sum_{\mu\nu} \gamma_{\mu\nu} E_\mu H_\nu - \dots, \quad (1.3)$$

where 3×3 tensors χ^e and χ^m are related with, respectively, the dielectric constant and the magnetic susceptibility. γ is called ME tensor. \mathcal{F}_0 represents $\mathcal{F}(E = 0, H = 0)$. Substituting Eq. (1.3) for Eqs. (1.1) and (1.2), we obtain

$$\mathbf{P} = \mathbf{P}_0 + \chi^e \mathbf{E} + \gamma \mathbf{H} + \dots, \quad (1.4)$$

$$\mathbf{M} = \mathbf{M}_0 + \chi^m \mathbf{H} + \gamma^\top \mathbf{E} + \dots. \quad (1.5)$$

In Eq. (1.4), \mathbf{P}_0 and $\chi^e \mathbf{E}$ represent spontaneous and dielectric polarization, respectively. In Eq. (1.5), \mathbf{M}_0 and $\chi^m \mathbf{H}$ represent spontaneous and magnetic-field induced magnetization, respectively. The contributions $\gamma \mathbf{H}$ and $\gamma^\top \mathbf{E}$ in Eqs. (1.4) and (1.5) represent linear ME effects, where electric polarization and magnetization are induced in proportion to the magnetic and electric fields, respectively. Both contributions originate from the ME term \mathcal{F}_{ME} in the free

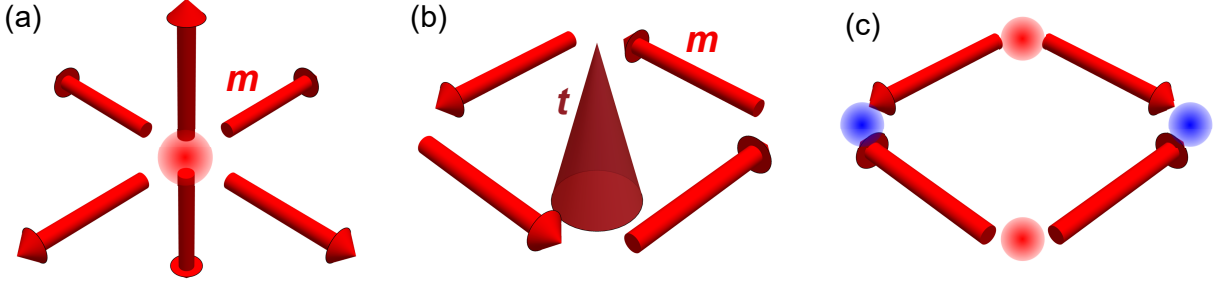


Figure 1.1: Schematic pictures of configurations of magnetic moments \mathbf{m} (red arrows) where (a) the magnetic monopole, (b) the toroidal moment, and (c) the magnetic quadrupole moment exist. Red and blue spheres in (a) and (c) denote the magnetic monopole with opposite signs. Red cone in (b) denotes the direction of the toroidal moment \mathbf{t} .

energy function,

$$\mathcal{F}_{\text{ME}} = - \sum_{\mu\nu} \gamma_{\mu\nu} E_{\mu} H_{\nu}. \quad (1.6)$$

As pointed out by Landau and Lifshitz [1], the linear ME effect occurs only when the spatial-inversion \mathcal{P} and the time-reversal \mathcal{T} symmetries are simultaneously broken. Under the spatial-inversion operation $\hat{\mathcal{P}}$, \mathbf{E} and \mathbf{P} are odd while \mathbf{H} and \mathbf{M} are even. Under the time-reversal operation $\hat{\mathcal{T}}$, \mathbf{H} and \mathbf{M} are odd while \mathbf{E} and \mathbf{P} are even. Since the free energy function \mathcal{F} is invariant for both operations $\hat{\mathcal{P}}$ and $\hat{\mathcal{T}}$, from Eq. (1.3), we can see that the ME tensor γ is odd under both \mathcal{P} and \mathcal{T} operations. Hence, γ is zero in the materials with \mathcal{P} or \mathcal{T} symmetry.

Relation to odd-parity magnetic multipoles

\mathcal{P} and \mathcal{T} symmetries are useful to classify various kinds of ferroic ordering [2]. Ferroelectric ordering is characterized by nonzero spontaneous polarization \mathbf{P}_0 which is a \mathcal{T} -even polar vector. On the contrary, ferromagnetic ordering is characterized by nonzero spontaneous magnetization \mathbf{M}_0 which is a \mathcal{T} -odd axial vector. Ferroelastic ordering and ferroaxial ordering are referred to as the ferroic ordering even to both \mathcal{P} and \mathcal{T} operations.

Simultaneous breaking of \mathcal{P} and \mathcal{T} symmetries in linear ME materials gives rise to ferroic ordering of odd-parity magnetic multipoles. In Ref. [3], definitions of the \mathcal{T} -odd pseudoscalar a , the \mathcal{T} -odd polar vector \mathbf{t} , and the magnetic quadrupole moment $q_{\mu\nu}$ are given as

$$a = \frac{1}{3} \sum_i \mathbf{r}_i \cdot \mathbf{m}(\mathbf{r}_i), \quad (1.7)$$

$$\mathbf{t} = \frac{1}{2} \sum_i \mathbf{r}_i \times \mathbf{m}(\mathbf{r}_i), \quad (1.8)$$

$$q_{\mu\nu} = \frac{1}{2} \sum_i \left(x_{i\mu} m_{\nu}(\mathbf{r}_i) + x_{i\nu} m_{\mu}(\mathbf{r}_i) - \frac{2}{3} \delta_{\mu\nu} \mathbf{r}_i \cdot \mathbf{m}(\mathbf{r}_i) \right), \quad (1.9)$$

respectively, using the spatial distribution of magnetic moments \mathbf{m} as a function of the position \mathbf{r}_i of the i -th particle. δ_{ij} denotes the Kronecker delta. Magnetic textures with nonzero a , \mathbf{t} ,

and q are illustrated in Figs. 1.1(a)-(c). a and \mathbf{t} are termed the magnetic monopole and the toroidal moment, respectively.

The connection between the ME tensor γ and the odd-parity magnetic multipoles become clearer by rewriting Eq. (1.6) as [3]

$$\mathcal{F}_{\text{ME}} = -\tilde{a}\mathbf{E} \cdot \mathbf{H} - \tilde{\mathbf{t}} \cdot (\mathbf{E} \times \mathbf{H}) - \sum_{\mu\nu} \tilde{q}_{\mu\nu}(E_\mu H_\nu + E_\nu H_\mu). \quad (1.10)$$

Here, the trace-like term $\tilde{a} = 1/3 \sum_i \gamma_{ii}$ is a \mathcal{T} -odd pseudoscalar and have the same symmetry as the magnetic monopole. The antisymmetric term $\tilde{\mathbf{t}}_\mu = 1/2 \sum_{\nu\lambda} \varepsilon_{\mu\nu\lambda} \gamma_{\nu\lambda}$ is a \mathcal{T} -odd polar vector and have the same symmetry as the toroidal moment. The remaining traceless symmetric term $\tilde{q}_{\mu\nu} = 1/2 \{\gamma_{\mu\nu} + \gamma_{\nu\mu} - (2/3)\delta_{\mu\nu} \gamma_{ii}\}$, where $\varepsilon_{\mu\nu\lambda}$ denotes the Levi-Civita symbol, has the same symmetry as the magnetic quadrupole moment. In addition to the above mentioned similarity in the symmetry, the relation between the magnetic multipoles and the ME susceptibilities has been derived in several theoretical studies [4, 5].

1.1.2 Example materials

Since the \mathcal{T} symmetry cannot be spontaneously broken without magnetic ordering, intensive studies on ME effects have been performed in magnetic materials. The ways of symmetry breaking and resultant ME effects are classified into three categories as shown in this subsection.

Simultaneous \mathcal{P} and \mathcal{T} symmetry breaking by magnetic ordering

In 1961, the first observation of the ME effect was performed on Cr_2O_3 where the \mathcal{P} and \mathcal{T} symmetries are simultaneously broken by antiferromagnetic ordering [6]. Cr_2O_3 crystallizes in the corundum structure with centrosymmetric the space group $R\bar{3}c$ [see Fig. 1.2(a)]. Due to inversion centers located at bond centers of Cr^{3+} - Cr^{3+} , γ is zero in the paramagnetic phase. Below the Néel temperature $T_N = 307$ K, Cr_2O_3 adopts easy-axis collinear antiferromagnetic ordering with the magnetic symmetry $\bar{3}'m'$ where the \mathcal{P} and \mathcal{T} symmetries are absent [see Fig. 1.2(a)]. As pointed out by Dzyaloshinskii in 1960 [7], the ME tensor γ has the following form:

$$\gamma = \begin{pmatrix} \gamma_\perp & 0 & 0 \\ 0 & \gamma_\perp & 0 \\ 0 & 0 & \gamma_\parallel \end{pmatrix}, \quad (1.11)$$

under this magnetic symmetry. From Eqs. (1.6), (1.10), and (1.11), the magnetic monopole a and the q_{z^2} -type magnetic quadrupole moment are not zero in Cr_2O_3 below T_N . Figure 1.2(b) shows the temperature dependence of these ME tensor elements obtained by measurements of electric-field induced magnetization at various temperatures [6]. As shown in Fig 1.2(b), the ME effects are clearly observed below T_N where the \mathcal{P} and \mathcal{T} symmetries are simultaneously broken by antiferromagnetic ordering.

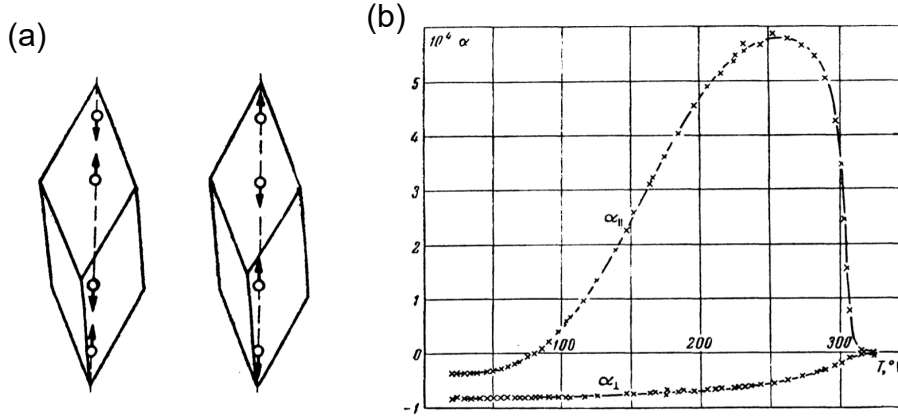


Figure 1.2: (a) Two possible antiferromagnetic ordering in rhombohedral unit cells of Cr₂O₃. Cr³⁺ ions are denoted by white circles. Inversion centers are located at the center of each cell. Black arrows represent magnetic moments. (b) Temperature dependence of the ME tensor elements in Cr₂O₃. α_{\perp} and α_{\parallel} correspond to γ_{\perp} and γ_{\parallel} in Eq. (1.11), respectively. Figures are taken from Ref. [6].

Antiferromagnetic ordering without doubling the crystallographic unit cell plays a crucial role in the scenario of the simultaneous symmetry breaking at the onset of magnetic ordering in Cr₂O₃. In centrosymmetric materials, ferromagnetic ordering, in which all magnetic moments are aligned in the same direction, do not violate the \mathcal{P} symmetry. Antiferromagnetic ordering doubling the unit cell never breaks the \mathcal{T} symmetry because the operation $\hat{\mathcal{T}}$ is equivalent to the translational operation of a lattice vector for such antiferromagnetic ordering [see Fig. 1.3(a)]. Therefore, in order for antiferromagnetic ordering to break the \mathcal{T} symmetry, a crystallographic unit cell must contain more than one magnetic atom.

The honeycomb structure which contains two atomic sites in a structural unit cell is where simple collinear antiferromagnetic ordering can simultaneously break the \mathcal{P} and \mathcal{T} symmetries. The inversion operation connecting two sublattices is no longer the symmetry operation in antiferromagnetic ordering depicted in Fig 1.3(b). In particular, the honeycomb structure is seen in various kinds of materials partly because the honeycomb network is realized by properly connecting the two-thirds of the octahedral vacancy of a hexagonal closed packing array of anions. Many linear ME materials including $A_4B_2O_9$ ($A = \text{Mn, Fe, Co}$ / $B = \text{Nb, Ta}$), MnTiO₃, and BaNi₂(PO₄)₂ have collinear antiferromagnetic ordering on the honeycomb structure [8, 9, 10, 11, 12, 13, 14]¹.

¹As will be mentioned in Ch. 3, Cr₂O₃ has the similar crystallographic structure to that of MnTiO₃.

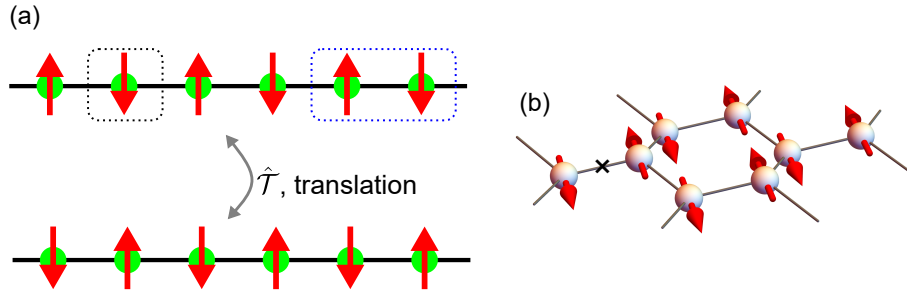


Figure 1.3: (a) Antiferromagnetic spin chain as an example of cell-doubling magnetic ordering. Black and blue dotted boxes denote crystallographic and magnetic unit cells. (b) Antiferromagnetic ordering on honeycomb structure. In (b) an inversion center is denoted by a cross mark. In (a) and (b), red arrows denote magnetic moments.

\mathcal{P} and \mathcal{T} symmetry breaking in noncentrosymmetric magnets

The \mathcal{P} and \mathcal{T} symmetries are independently broken by the noncentrosymmetric crystallographic structure and the presence of net magnetization, respectively. In 1964, the first observation of the ME effect in such noncentrosymmetric ferromagnets was performed on GaFeO_3 [15]. GaFeO_3 crystallizes in the orthorhombic polar structure with the space group $Pc2_1n$ [16]. Spontaneous polarization is oriented along the b axis. Below the critical temperature $T_c = 210$ K, GaFeO_3 adopts ferrimagnetic ordering with spontaneous magnetization along the c axis. For the resultant magnetic point group symmetry of $m'2'm$, the ME tensor has the following form:

$$\gamma = \begin{pmatrix} 0 & 0 & 0 \\ 0 & 0 & \gamma_{bc} \\ 0 & \gamma_{cb} & 0 \end{pmatrix}. \quad (1.12)$$

Judging from Eqs. (1.6), (1.10), and (1.12), the a -component of the magnetic toroidal moment t_a and the q_{bc} -type magnetic quadrupole moment are not zero in GaFeO_3 . Figure 1.4(a) shows magnetic-field induced polarization in GaFeO_3 [17]. The linear ME effect arising from γ_{bc} in Eq. (1.12) is clearly observed while γ_{cb} seems to be absent. The striking asymmetry between γ_{bc} and γ_{cb} indicates that the antisymmetric ME effect related to the toroidal moment t_a and the symmetric effect related to the q_{bc} -type quadrupole moment is comparable in GaFeO_3 .

In GaFeO_3 , the toroidal moment \mathbf{t} is induced along the outer product $\mathbf{P}_0 \times \mathbf{M}_0$ of spontaneous polarization \mathbf{P}_0 and magnetization \mathbf{M}_0 . Generally speaking, the toroidal moment is induced perpendicular to both polarization and magnetization in polar ferromagnets [see Fig. 1.4(b)], because the outer product of a \mathcal{T} -even polar vector and a \mathcal{T} -odd axial vector always becomes \mathcal{T} -odd polar vector. This relation between polarization and magnetization, and the toroidal moment can be seen from Eq. (1.8). By neglecting the spatial variation of magnetic moments and substituting $\mathbf{m}(\mathbf{r}_\alpha) = \mathbf{m}_0$ for Eq. (1.8), we obtain

$$\mathbf{t} = \frac{1}{2} \left(\sum_i \mathbf{r}_i \right) \times \mathbf{m}_0. \quad (1.13)$$

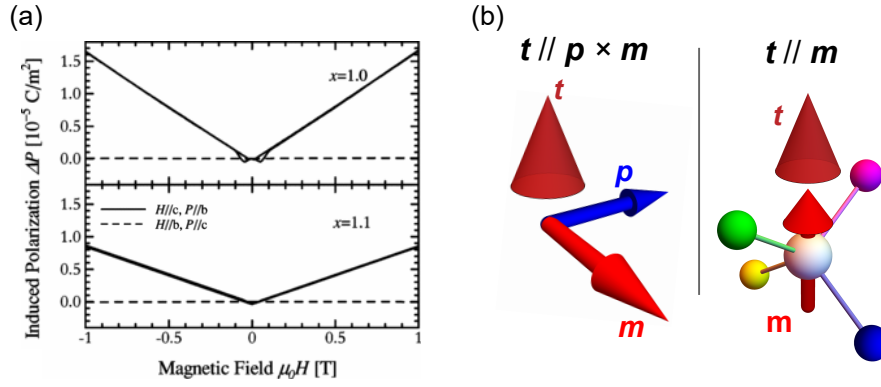


Figure 1.4: (a) Magnetic-field induced electric polarization in $\text{Ga}_{2-x}\text{Fe}_x\text{O}_3$ at 4.2 K. (b) Illustration of the relation between the toroidal moment \mathbf{t} and the magnetic dipole \mathbf{m} in (left) polar and (right) chiral materials. In the left panel, an electric dipole moment \mathbf{p} is denoted by a blue arrow. In the right panel, a tetrahedral arrangement of nonmagnetic atoms is shown by spheres. (a) is taken and arranged from Ref. [17].

With the definition of the electric dipole moments [see Eq. (1.14)], Eq. (1.13) directly leads to the relation $\mathbf{t} \parallel \mathbf{P}_0 \times \mathbf{m}_0$.

Another way of constructing the \mathcal{T} -odd polar vector quantity is to multiply the \mathcal{T} -odd axial vector by a \mathcal{T} -even pseudoscalar. Chirality in materials is characterized by the similarity to \mathcal{T} -even pseudoscalar observables such as natural optical rotation [18]. Therefore, the presence of nonzero toroidal moment along magnetization is always symmetry-allowed in chiral magnets [see Fig. 1.4(b)]. The toroidal moment induced parallel to magnetization in chiral magnets reverses the direction when the direction of magnetization or the sign of chirality reverses. Microscopically, spatial distribution of magnetic moments in atomic scale originating from the orbital hybridization between magnetic and nonmagnetic atoms might be the origin of the toroidal moment along the magnetization of the magnetic atom [19].

\mathcal{P} -symmetry breaking by magnetic ordering

Revival in the researches of ME materials in this decade or so owes itself to discoveries of large nonlinear ME effects in certain manganese oxides at the beginning of this century. Nonlinear ME effects where electric polarization is modified by the application of the magnetic field are symmetry-allowed when the \mathcal{P} and \mathcal{PT} symmetries are broken. Large effects are expected in cases where the \mathcal{P} symmetry is broken at the onset of magnetic ordering.

In 2003, Kimura *et al.* reported a colossal nonlinear ME effect in TbMnO_3 [20]. TbMnO_3 crystallizes in the orthorhombically distorted perovskite structure with the centrosymmetric space group symmetry $Pbnm$. Below the critical temperature $T_c = 27$ K, TbMnO_3 adopts cycloidal helimagnetic ordering with the magnetic propagation vector $\mathbf{q} = (0, 0.27, 1)$ [21]. The \mathcal{P} symmetry is broken by the cycloidal helimagnetic ordering and electric polarization arises along the c axis of the crystal below T_c even in the absence of magnetic fields [see Fig. 1.5(a)].

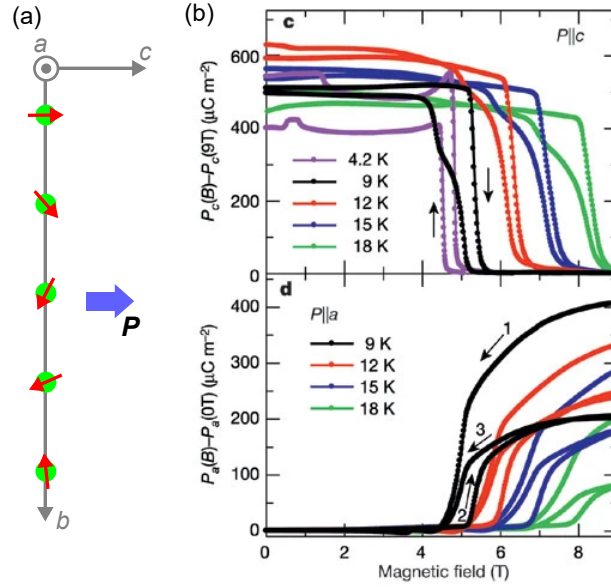


Figure 1.5: (a) Schematic illustration of the magnetic structure of TbMnO₃ below T_c and at 0 T. Magnetic moments are denoted by red arrows. The direction of electric polarization is described by a blue arrow. (b) Magnetic-field induced polarization rotation in TbMnO₃. The magnetic field is applied along the *b* axis. (b) is taken from Ref. [20].

The modulation of cycloidal magnetic ordering by the magnetic field accompanies the large nonlinear ME effect as shown in Fig. 1.5(b).

1.1.3 Microscopic origin of ME effects

Microscopically, the electric dipole moment $\hat{\mathbf{p}}$ and the magnetic dipole moment $\hat{\mathbf{m}}$ of the electronic system is given by

$$\hat{\mathbf{p}} = -e \sum_i \hat{\mathbf{r}}_i, \quad (1.14)$$

$$\hat{\mathbf{m}} = -\frac{\mu_B}{\hbar} \sum_i (\hat{\mathbf{l}}_i + g\hat{\mathbf{s}}_i), \quad (1.15)$$

using the position $\hat{\mathbf{r}}_i$ and the orbital and spin angular momentums $\hat{\mathbf{l}}_i$ and $\hat{\mathbf{s}}_i$ of the *i*-th electron, respectively. Here e , μ_B , \hbar , and g denote the elementary charge, the Bohr magneton, the Planck constant, and the g factor.

Coupling between magnetic ordering and electric polarization gives rise to the ME effects. Magnetic ordering is the arrangement of magnetic moments $\mathbf{m}(\mathbf{r})$ as a function of positions of magnetic atoms. The modification of magnetic ordering by the application of the small magnetic field $\Delta\mathbf{H}$ is expressed as

$$\mathbf{m}(\mathbf{r}, \Delta\mathbf{H}) = \mathbf{m}(\mathbf{r}, 0) + \frac{\partial \mathbf{m}(\mathbf{r}, 0)}{\partial \mathbf{H}} \Delta\mathbf{H} + \dots \quad (1.16)$$

Let us assume that the electric dipole moment \mathbf{p}_i of the *i*-th atom is given as a functional \mathbf{F}_i of magnetic ordering $\mathbf{m}(\mathbf{r})$ as $\mathbf{p}_i = \mathbf{F}_i[\mathbf{m}]$. From Eq. (1.16), the effect of the small magnetic field

\mathbf{H} on \mathbf{p}_i is written as

$$\mathbf{p}_i(\Delta\mathbf{H}) = \mathbf{p}_i(0) + \left(\int \frac{\delta \mathbf{F}_i}{\delta \mathbf{m}} \frac{\partial \mathbf{m}(\mathbf{r}, 0)}{\partial \mathbf{H}} d\mathbf{r} \right) \Delta\mathbf{H} + \dots \quad (1.17)$$

Here the second term in the right hand side of Eq. (1.17) describes the magnetic-field modification of polarization.

Coupling between magnetic ordering and electric polarization can be explained as inverse effects of various magnetic interactions. Magnetic interactions are influenced by the configuration of magnetic and nonmagnetic atoms. Since the applied electric field should shift positions of atoms, the magnetic interaction should be modified by electric fields. The above mentioned functional \mathbf{F}_i is given by computing the electric-field derivative of magnetic interactions. Most of the observed ME effects are explained in terms of the inverse effects of the magnetic exchange interaction, the Dzyaloshinskii-Moriya (DM) interaction and the single-ion anisotropy.

A contribution from the inverse effect of the exchange interaction is often referred to as the exchange striction mechanism and written as

$$\mathbf{p}_{\text{ext},i} = \sum_j \mathbf{\Pi}_{ij} \{ \mathbf{m}(\mathbf{r}_i) \cdot \mathbf{m}(\mathbf{r}_j) \}. \quad (1.18)$$

The vector $\mathbf{\Pi}_{ij}$ is not zero only when there is no inversion center between sites \mathbf{r}_i and \mathbf{r}_j . A theoretical study [22] suggests that the exchange striction mechanism accounts for the linear ME effect arising from γ_{\parallel} in Cr_2O_3 at high temperature. In Cr_2O_3 , the application of magnetic field along the c axis changes the magnetic symmetry from $\bar{3}'m'$ to 3 , where the c -component of $\mathbf{\Pi}$ is not zero for all pairs of two Cr^{3+} ions. The exchange striction mechanism also well describes electric polarization spontaneously arising at the onset of up-up-down-down antiferromagnetic ordering [23, 24].

A contribution from the inverse effect of the magnetic anisotropy is derived as the single-ion effect. In Ref. [22], the low temperature part of γ_{\parallel} in Cr_2O_3 is described in terms of the electric-field-dependent g factor. In 2007, Arima presented the microscopic description of the single-ion effect by the analysis of spin-dependent hybridization between the d orbital of a magnetic ion and the p orbital of a nonmagnetic anion [25]. This spin-dependent d - p hybridization mechanism is conveniently expressed as [26]

$$\mathbf{p}_{pd,i} = \sum_j c_{ij} \{ \mathbf{m}(\mathbf{r}_i) \cdot \mathbf{e}_{ij} \}^2 \mathbf{e}_{ij}, \quad (1.19)$$

using unit vectors \mathbf{e}_{ij} which connects a magnetic ion at \mathbf{r}_i and the j -th surrounding anion at \mathbf{r}_j . c_{ij} denotes the coupling coefficient.

A contribution from the inverse effect of the DM interaction is often referred to as the spin-current mechanism. By the analysis of the minimal model containing a nonmagnetic anion surrounded by two magnetic ions, Katsura *et al.* presented the microscopic description of the effect [27]. The spin-current mechanism is described as

$$\mathbf{p}_{sc,i} = c_{ij} \sum_j \mathbf{e}_{ij} \times \{ \mathbf{m}(\mathbf{r}_i) \times \mathbf{m}(\mathbf{r}_j) \}, \quad (1.20)$$

using the unit vector \mathbf{e}_{ij} connecting magnetic ions at positions \mathbf{r}_i and \mathbf{r}_j and the coupling coefficients c_{ij} . This mechanism successfully explains electric polarization arising from cycloidal magnetic ordering.

1.2 Application of magnetoelectric effects

1.2.1 Optical magnetoelectric coupling

Formulation

Here we review the formulation of the linear ME effect in a visible electromagnetic wave given in Ref. [28]. The interaction between materials and the oscillating electric (magnetic) field \mathbf{E}^ω (\mathbf{B}^ω) with angular frequency ω is given by regarding the light-matter interaction V as time-dependent perturbation to the system. The scalar and vector potentials ϕ and \mathbf{A} , respectively, which satisfy

$$\mathbf{E}^\omega = -\nabla\phi - \frac{\partial\mathbf{A}}{\partial t}, \quad (1.21)$$

$$\mathbf{B}^\omega = \nabla \times \mathbf{A} \quad (1.22)$$

are written as

$$\phi(\mathbf{r}) = \phi(\mathbf{r}_0) - \mathbf{r} \cdot \mathbf{E}^\omega(\mathbf{r}_0) - \frac{1}{2} \sum_{\mu\nu} x_\mu x_\nu \left. \frac{\partial E_\nu^\omega}{\partial x_\mu} \right|_{\mathbf{r}=\mathbf{r}_0} + \dots, \quad (1.23)$$

$$A_\mu(\mathbf{r}) = \frac{1}{2} \sum_{\nu\lambda} \varepsilon_{\mu\nu\lambda} x_\lambda B_\nu^\omega(\mathbf{r}_0) + \frac{1}{3} \sum_{\nu\lambda\rho} \varepsilon_{\mu\lambda\rho} x_\nu x_\rho \left. \frac{\partial B_\lambda^\omega}{\partial x_\nu} \right|_{\mathbf{r}=\mathbf{r}_0} + \dots. \quad (1.24)$$

By substituting Eqs. (1.23) and (1.24) for the Hamiltonian $\mathcal{H} = \frac{1}{2m_e}(\hat{\mathbf{p}}_{\text{kin}} - e\mathbf{A})^2 - e\phi$, where m_e and $\hat{\mathbf{p}}_{\text{kin}}$ denote the mass of electron and the momentum operator, respectively, and using Eqs. (1.14) and (1.15), we obtain the light-matter interaction V as

$$V = -e\phi(\mathbf{r}_0) - \hat{\mathbf{p}} \cdot \mathbf{E}^\omega(\mathbf{r}_0) - \hat{\mathbf{m}} \cdot \mathbf{B}^\omega(\mathbf{r}_0) - \frac{1}{3} \sum_{\mu\nu} \hat{\Theta}_{\mu\nu} \left. \frac{\partial E_\nu^\omega}{\partial x_\mu} \right|_{\mathbf{r}=\mathbf{r}_0} + \dots. \quad (1.25)$$

$\hat{\Theta}_{\mu\nu}$ stands for the electric quadrupole moment defined as $\hat{\Theta}_{\mu\nu} = -\frac{e}{2} \sum_i (3x_{i\mu}x_{i\nu} - \delta_{\mu\nu}x_i^2)$.

One of the most prominent consequences of the optical ME effect is the electromagnetic wave generated by \mathbf{B}^ω -induced oscillating polarization. The oscillating electric dipole \mathbf{p}^ω with angular frequency ω under the radiation with the photon energy $\hbar\omega$ is written as

$$\mathbf{p}^\omega = \chi^e \mathbf{E}^\omega + \gamma \mathbf{B}^\omega + \frac{1}{3\omega} \sum_{\mu\nu} \mathbf{A}'_{\mu\nu} \frac{\partial \dot{E}_\nu^\omega}{\partial x_\mu} + \dots, \quad (1.26)$$

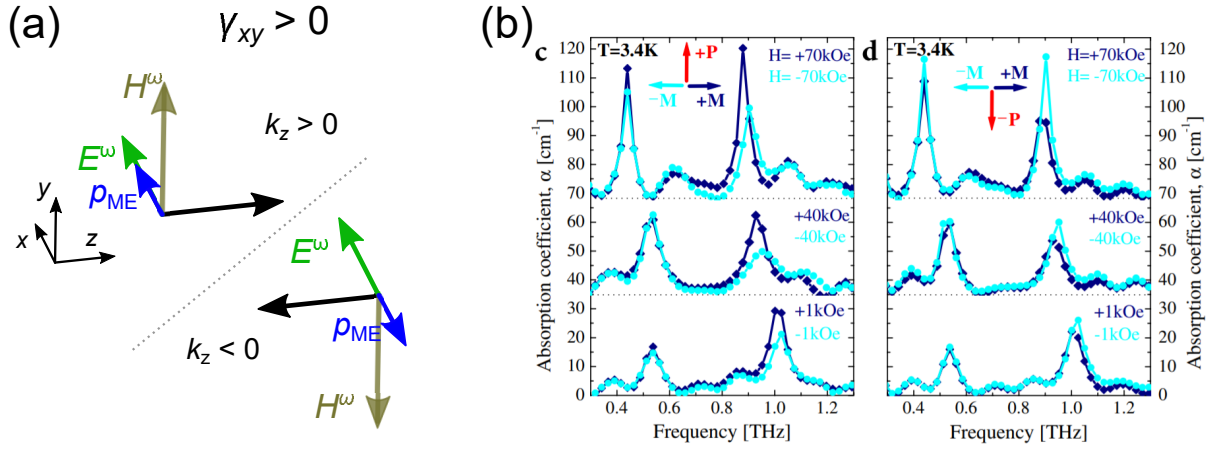


Figure 1.6: (a) Illustration of the origin of the direction-dependent interference between E^ω and H^ω -induced polarization. (b) Absorption spectra of $\text{Ba}_2\text{CoGe}_2\text{O}_7$ for the microwave propagating along the $[1\bar{1}0]$ direction. (b) is taken and arranged from Ref. [29].

using susceptibilities

$$\chi_{\mu\nu}^e = 2 \sum_n \frac{\Delta_n}{(\Delta_n^2 - \hbar^2\omega^2) - i\hbar\omega\delta_n - \frac{1}{4}\delta_n^2} \text{Re}(\langle g|\hat{p}_\mu|e_n\rangle \langle e_n|\hat{p}_\nu|g\rangle), \quad (1.27)$$

$$\gamma_{\mu\nu} = 2 \sum_n \frac{\Delta_n}{(\Delta_n^2 - \hbar^2\omega^2) - i\hbar\omega\delta_n - \frac{1}{4}\delta_n^2} \text{Re}(\langle g|\hat{p}_\mu|e_n\rangle \langle e_n|\hat{m}_\nu|g\rangle), \quad (1.28)$$

$$A'_{\mu\nu} = -2 \sum_n \frac{\Delta_n}{(\Delta_n^2 - \hbar^2\omega^2) - i\hbar\omega\delta_n - \frac{1}{4}\delta_n^2} \text{Re}(\langle g|\hat{p}|e_n\rangle \langle e_n|\hat{\Theta}_{\mu\nu}|g\rangle). \quad (1.29)$$

Here $|g\rangle$ and $|e_n\rangle$ denote the ground state and the n -th excited state with the excitation energy Δ_n of the system, respectively. δ_n represents the corresponding damping factor for the excitation. Equation (1.28) represents the ME effects in optical frequencies. From Eqs. (1.28), the microscopic origin of the optical ME effects is traceable to the interplay between the electric-dipole and magnetic-dipole transitions to the excited state. The prominent effects are usually seen in resonating frequency $\hbar\omega \sim \Delta_n$, where the denominator in Eq. (1.28) takes the minimum value. The nature of the relevant excitation to the $|e_n\rangle$ state highly depends on the photon energy.

Magnetolectric optical effects

Off diagonal ME coupling arising from the ME tensor element $\gamma_{\mu\nu}$ ($\nu \neq \mu$) shows up as the nonreciprocal optical effect where the optical properties of materials depends on the direction of light. The mechanism of nonreciprocity is illustrated in Fig. 1.6(a). We take polarized light with $E^\omega \parallel e_x$ travelling through an ME material with $\gamma_{xy} > 0$ in the z direction as example. When E_x^ω is positive, H_y^ω is also positive for light with $k_z > 0$ because E^ω , H^ω , and the propagation vector \mathbf{k} must satisfy the relation $\mathbf{k} \times E^\omega = \omega H^\omega$. Here the oscillating magnetic field $H_y^\omega > 0$ induces oscillating electric polarization p_{ME} along the x axis. $\gamma_{xy} > 0$ leads to $p_{ME,x} > 0$. Consequently, the oscillating electric field and induced polarization constructively interfere with each other in

this case. If we keep the direction of \mathbf{E}^ω as $E_x^\omega > 0$, the reversal of \mathbf{k} from $k_z > 0$ to $k_z < 0$ means the reversal of \mathbf{H}^ω from $H_y^\omega > 0$ to $H_y^\omega < 0$, which accompanies the reversal of induced polarization. Hence, oscillating electric field and induced polarization destructively interfere for light beam with $k_z < 0$. The direction-dependent interference leads to the nonreciprocal optical effects. In the similar way, even when the direction of light is fixed, the optical ME coupling shows up as the difference in optical properties for the change in ME susceptibilities γ .

In THz frequency, incident light resonates with collective lattice and magnetic excitations. In 2011, Kézsmárki *et al.* reported magnetoelectric optical effects in $\text{Ba}_2\text{CoGe}_2\text{O}_7$ in THz frequency [29]. In the experiment, the direction of the toroidal moment \mathbf{t} was controlled by the manipulation of net polarization \mathbf{P} and magnetization \mathbf{M} [see the inset of Fig. 1.6(b)]. From Eqs. (1.6) and (1.10), the reversal of the toroidal moment leads to the sign change in the corresponding antisymmetric components in the ME tensor. As shown in Fig. 1.6(b), the difference in the absorption coefficients was observed for the sign change in γ .

The pronounced magnetoelectric optical effects have been also reported in visible range where incident light resonates with the intra-atomic $d-d$ excitations. Directional dichroism of light in visible range is reviewed in Ch. 3. In addition to absorption [30, 31], directional refraction and luminescence are also observed in an ME weak ferromagnet CuB_2O_4 [32, 33].

1.2.2 Electric-field control of antiferromagnetic structure

ME coupling enables electric control of antiferromagnetic structures. Antiferromagnetic materials embody various advantageous features for spintronic application such as zero stray fields, robustness against external magnetic fields, and ultrafast dynamics in THz ranges [34]. To exploit the full functionality of antiferromagnets, the manipulation of magnetic ordering is inevitable. However, the lack of interaction between antiferromagnetic ordering with zero magnetization and external magnetic field disrupts the use of conventional ways of manipulating magnetic structures employed in ferromagnetic materials.

Voltage control of antiferromagnetic structures in ME antiferromagnets is achieved by the manipulation of ferroelectric polarization of spin origin. When several types of distinct antiferromagnetic ordering give rise to different values of electric polarization, the electric-field control of polarization leads to control of the antiferromagnetic structure. This methodology works well in antiferromagnets where the \mathcal{P} symmetry is broken at the onset of magnetic ordering. Ferroic nature of magnetically induced polarization enables nonvolatile control of antiferromagnetic ordering where the manipulated antiferromagnetic structure retains even after turning off electric fields.

In linear ME antiferromagnets where the \mathcal{P} and \mathcal{T} symmetries are simultaneously broken by magnetic ordering, antiferromagnetic structures are controlled by the application of both electric and magnetic fields. Two distinct antiferromagnetic structures connected by the \mathcal{T} operation host γ of opposite signs because γ is also odd under the \mathcal{T} operation. In a uniform magnetic

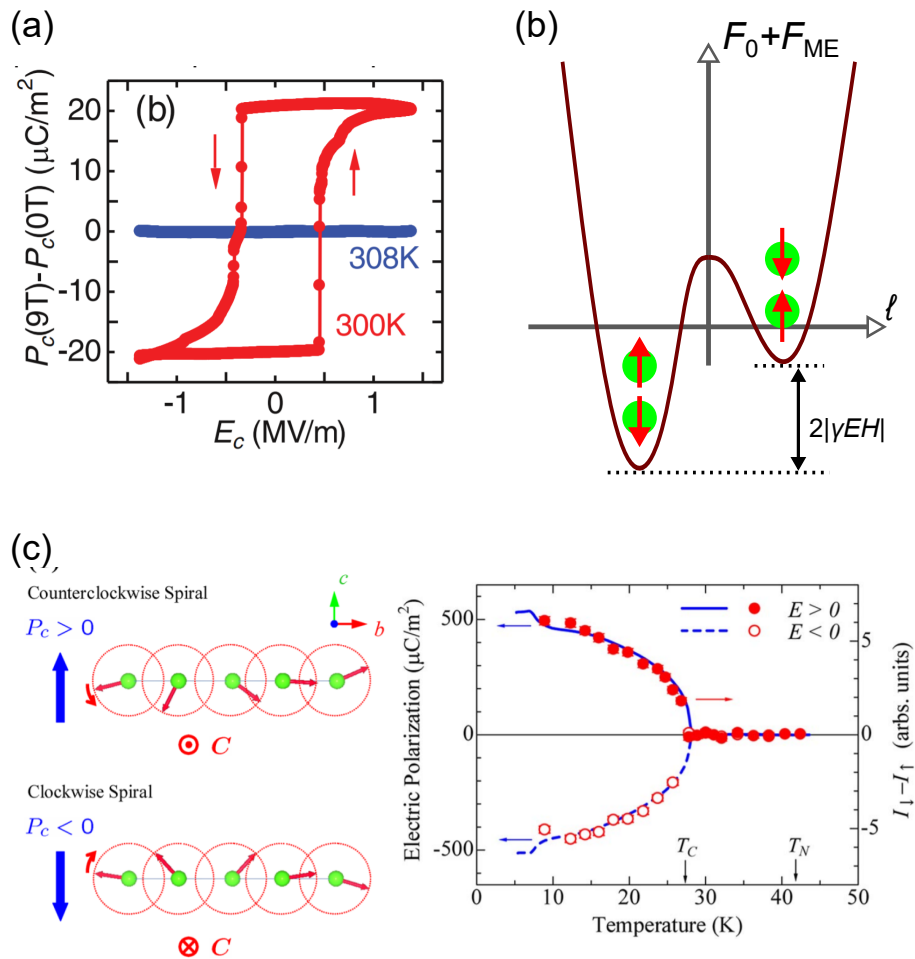


Figure 1.7: (a) Electric-field induced reversal of magnetic-field induced polarization in Cr_2O_3 . (b) Free energy as a function of ME tensor γ . Red arrows denote relevant antiferromagnetic states. (c) (left) Schematic illustrations of two kinds of cycloidal structure in TbMnO_3 . (right) Temperature dependence of polarization and the difference in magnetic scattering. Subscript \uparrow and \downarrow denote the direction of neutron spin. (a) and (c) are taken and arranged from Refs. [35] and [36], respectively.

field, the direction of magnetic-field induced polarization is opposite for such antiferromagnetic states. Here, ferroelectric switching of magnetic-field induced polarization is nothing but voltage control of the antiferromagnetic structure in a magnetic field. Magnetoelectric switching of antiferromagnetic states in Cr_2O_3 was demonstrated in 1966 by monitoring the volume fraction of the two antiferromagnetic states by the measurement of γ over the whole sample [37]. Recent investigation of the ferroelectric hysteresis loop of magnetically induced polarization in Cr_2O_3 [35] reveals that the electric field of 0.5 MV/m is large enough to switch antiferromagnetic states in a magnetic field of 9 T and at 300 K [see Fig 1.7(a)]. The field controllability of antiferromagnetic ordering has stimulated the engineering of magnetoelectric random access memory using Cr_2O_3 [38].

Electric-field control of antiferromagnetic ordering in linear ME antiferromagnets is also regarded as the ferroic control of odd-parity magnetic multipoles. Figure 1.7(b) shows the relevant free energy profile as a function of the antiferromagnetic order parameter l . When antiferromagnetic ordering gives rise to the nonzero linear ME tensor γ , the components of γ are proportional to l . Below T_N , $\mathcal{F}_0 + \mathcal{F}_{\text{ME}}$ is a double-well potential with two minima corresponding to two distinct antiferromagnetic states. Considering the coupling between ME tensor γ and magnetic multipoles [see Eqs. (1.6) and (1.10)], the double-well potential in Fig. 1.7 can be viewed as the expansion of the free energy by relevant multipoles. The conjugate field EH lifts the degeneracy between two states and enables ferroic switching of magnetic multipoles. We note that the exact form of the conjugate field for each multipole is seen from Eq. (1.10).

In nonlinear ME antiferromagnets where spontaneous polarization arises at the onset of magnetic ordering, antiferromagnetic structures are manipulated only by the electric field. In 2007, Yamasaki *et al.* demonstrated electric-field control of the cycloidal magnetic structure in TbMnO_3 . In TbMnO_3 where the helimagnetic structure is stabilized by magnetic frustration, and not by the DM interaction, two kinds of cycloidal structure with opposite helicity [see Fig. 1.7(c)] is degenerated in the absence of electric fields. From Eq. (1.20), the two kinds of cycloidal structures give rise to electric polarization in opposite directions. In the experiment, the helicity of the cycloidal structure was manipulated by the electric field and detected by means of the neutron diffraction [36].

1.3 Research purpose

Antiferromagnets with little or no spontaneous magnetization are attracting growing attention by virtue of no stray field and potential high-speed dynamics. The absence of spontaneous magnetization makes it difficult to control and visualize antiferromagnetic domain structures. As we have reviewed in this chapter, ME coupling enables electric control of antiferromagnetic structures and gives rise to the nonreciprocal optical effects which potentially enable imaging of antiferromagnetic domain patterns. However, the nonreciprocal magnetoelectric optical effects in the visible range in collinear antiferromagnets with no magnetization have remained

elusive. The discovery of the magnetoelectric optical effect in such antiferromagnets should literally shed light on the details in the antiferromagnetic domain-wall dynamics, which cannot be tracked without imaging experiments.

The purposes of this study are (1) to show that collinear antiferromagnetic ordering with zero magnetization can be a source of a nonreciprocal optical effect, (2) to demonstrate the domain-imaging technique based on the magnetoelectric optical effects, and (3) to investigate the electric-and-magnetic-field induced switching dynamics in the antiferromagnet by the imaging study. To achieve these purposes, we have focused on MnTiO_3 where the toroidal moment is activated by the combination of collinear antiferromagnetic ordering and the locally broken \mathcal{P} symmetry at the atomic sites.

Chapter 2

Experimental Methods

2.1 Sample preparation

Homogenized mixture of the stoichiometric ratio of MnO and TiO₂ was pressed into rods under the hydrostatic pressure of 24 MPa. The rods were then calcined at 1200 °C for 24 hours [see Fig. 2.1(a)] in flowing Ar atmosphere with Ti powder placed beside the rods as a getter of oxygen. Single crystals of MnTiO₃ were grown by the floating zone method in flowing Ar atmosphere. The seed and feed rods were counter rotated and the typical growth rate was 2 mm/h.

Obtained single crystals [see Fig. 2.1(b)] were characterized by x-ray diffraction. The phase purity of a representative sample was confirmed by powder x-ray diffraction using a Rigaku SmartLab diffractometer with Cu K_α radiation. The crystal orientation was determined by Laue x-ray diffraction in the Institute for Solid State Physics (ISSP). A typical Laue pattern of the *c* plane of the crystal is shown in Fig. 2.2. Oriented crystals were cut into plates for each experiment.

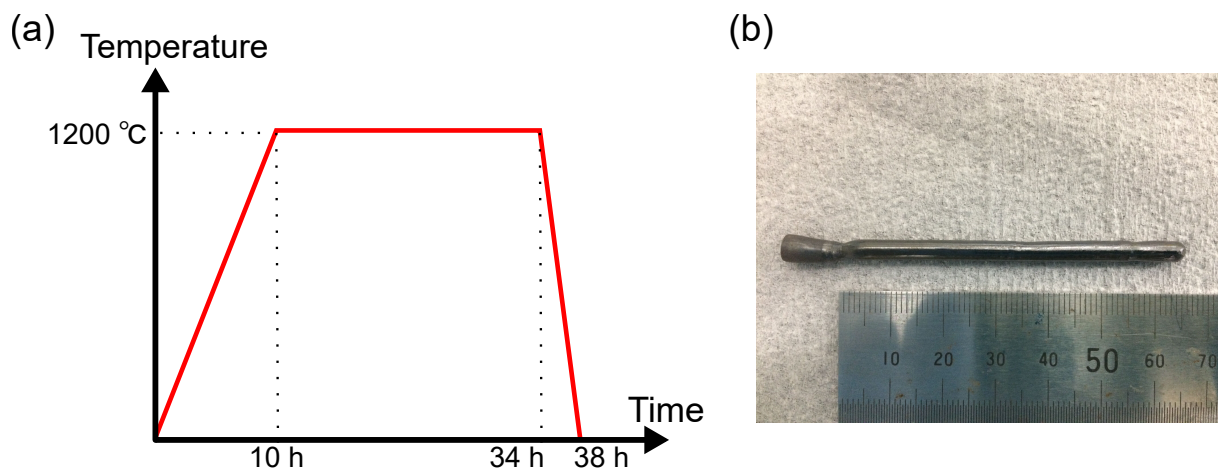


Figure 2.1: (a) Heating profile. (b) Obtained single-crystalline rod of MnTiO₃.

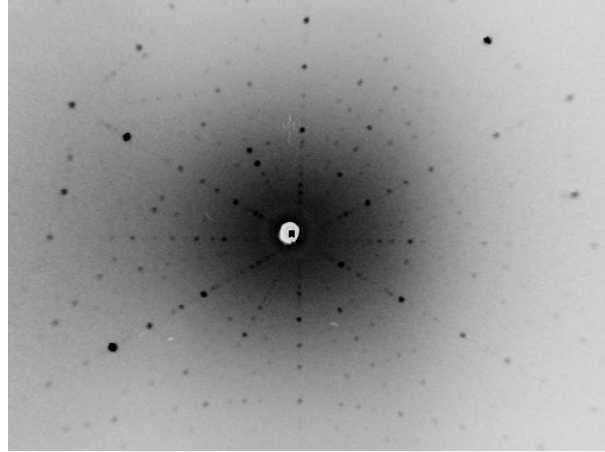


Figure 2.2: Laue pattern of the c plane of a single crystal of MnTiO_3 . Three fold symmetry is apparent.

2.2 Magnetization and electric polarization measurements

Magnetization

Magnetization was measured using a superconducting quantum interference device (MPMS-XL, Quantum Design). Magnetic susceptibility χ was obtained by dividing the magnetization by the magnetic field.

Electric polarization

The temperature (T), magnetic-field (\mathbf{H}), and electric-field (\mathbf{E}) dependence of electric polarization (\mathbf{P}) was measured using a 9-T superconducting magnet system (Physical Property Measurement System, Quantum Design, and MagLab, Oxford Instruments). For the change of the parameter X ($X = T, \mathbf{H}, \mathbf{E}$), the displacement current $\mathbf{I}(t)$ flows as,

$$\mathbf{I}(t) = S \frac{\partial \mathbf{P}}{\partial X} \frac{dX}{dt}, \quad (2.1)$$

as a function of time t . Here S is the area of the electrode formed on the surface of the sample. The change in electric polarization was obtained by integrating the displacement current with respect to t as

$$P(X_2) - P(X_1) = \int_{t_1}^{t_2} I(t) dt, \quad (2.2)$$

where X_i stands for $X(t_i)$. In case we know that electric polarization is zero under the condition described by the parameter $X = X_1$, $P(X_2)$ can be extracted from Eq. (2.2).

The displacement current was measured in the two-terminal setup depicted in Fig. 2.3. The electrode was formed by silver paste on both surfaces of the plate-shaped sample. The displacement current was measured by electrometers (6517A and 6517B, Keithley). In measurements of the T - and H - dependence of polarization, ferroelectric domains were poled in the poling process

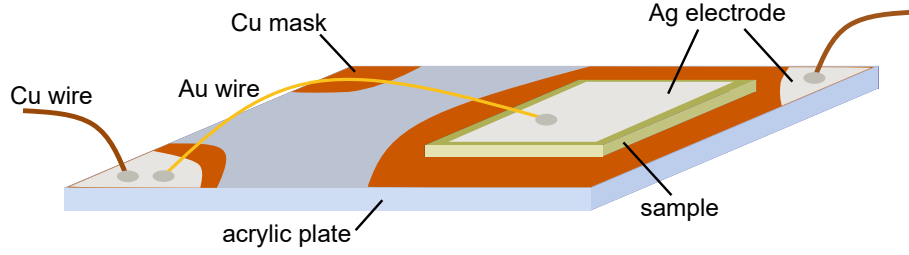


Figure 2.3: Illustration of the two-terminal setup for the electric polarization measurements. Plate-shaped sample with electrode formed on both surfaces is placed on an insulating acrylic plate partially masked by copper.

where electric and magnetic fields were simultaneously applied. Details about the poling process are given in the following section.

2.3 Optical measurements

Absorption spectroscopy

Optical absorption measurements were carried out in a cryostat equipped with a 15-T magnet at High Field Laboratory for Superconducting Materials in Tohoku University. A crystal of MnTiO_3 was shaped into a plate with large c planes and polished to reduce the thickness d to $90 \mu\text{m}$. The thin plate of MnTiO_3 is transparent and has yellowish red color as shown in Fig. 2.4(a).

The whole optical setup is schematically illustrated in Fig. 2.4(b). Unpolarized light from a halogen lamp was introduced to propagate along the c axis of the crystal. The threefold rotational symmetry around the c axis of the crystal allows no optical anisotropy in the c plane. The transmitted light was analyzed by a spectrometer (iHR550, HORIBA) equipped with a charge-coupled device (CCD) detector. In our measurements using a grating of 150 gr/mm , the spectral resolution was typically better than 1 nm . The electric and magnetic fields were applied along the c axis of the crystal. For the application of the electric field, gold with a thickness of 250 \AA was sputtered onto both c planes to form electrodes. The propagation direction of light was switched between $k_c > 0$ and $k_c < 0$ by interchanging the light source and the light detector.

By the Beer-Lambert law, the transmitted light intensity I is expressed as

$$I = I_0 e^{-\alpha d}, \quad (2.3)$$

using the incident light intensity I_0 and the absorption coefficient α . The absorption coefficient α is computed from I_0 and I as

$$\alpha = \ln \left(\frac{I_0}{I} \right) d. \quad (2.4)$$

I_0 was measured by collecting light without setting the sample in optical setup. The incident light spectrum is displayed in Fig. 2.4(c) for the incident photon energy of $\hbar\omega = 1.8 - 3 \text{ eV}$.

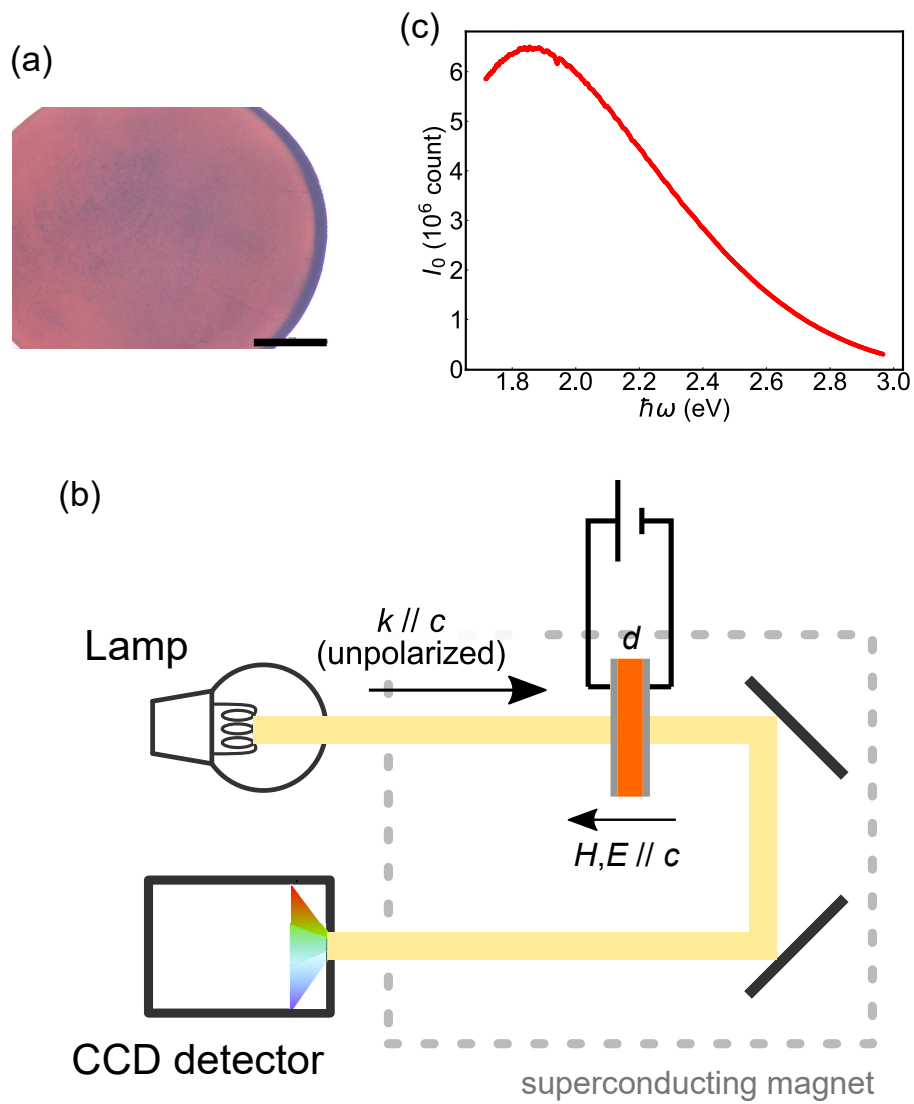


Figure 2.4: (a) *c*-plane photograph of the MnTiO₃ crystal. Black bar corresponds to 1 mm. (b) Schematic illustration of the setup for absorption spectroscopy. (c) Incident light spectrum.

I_0 takes its maximum around 1.8 eV and we did not suffer from the shortage of incident light below 2.8 eV.

Antiferromagnetic domain imaging

The optical setup for domain imaging experiments is schematically illustrated in Fig. 2.5(a). Light from a halogen lamp was monochromatized by the blazed grating monochromator (M25, Bunkoiki) and was introduced to propagate along the c axis of the crystal. Transmitted light was detected by a CCD camera (Alta U6, Apogee Instruments). To reduce the influence of the roughness of the surfaces of the crystal and the spatially inhomogeneous distribution of incident light, we obtained difference images by subtracting a reference image without domain patterns from each image.¹ The output light from the monochromator is not completely unpolarized. In several experiments, polarizer was placed before the sample to obtain linearly polarized light. Unless otherwise noticed, the imaging experiments were carried out at a photon energy $\hbar\omega = 2.16$ eV.

Figures 2.5(b) shows the cross-sectional view of the sample mounted on the copper plate. As in the absorption measurement, single crystals of MnTiO_3 were cut into plates with large c planes and thinned to 0.1-0.15 mm. Both surfaces of the thin-plate sample were carefully polished using the lapping films of the particle size $0.3 \mu\text{m}$ to reduce the contribution from scattering to the transmitted-light profile. For imaging experiments in the electric field, gold with a thickness of 175 \AA was sputtered onto both c planes to form electrodes. The crystal was placed on the holed copper plate. Figure 2.5(c) shows the photograph of the setup of the sample. Since all the sample was larger than the optical window in the copper plate, the edge of the field of view lay in the crystals. The crystal was cooled down in a ^4He closed-cycle refrigerator. Electric and magnetic fields were applied along the c axis of the crystal using a high voltage supply (Model 2657A, Keithley) and an electromagnet, respectively. A high voltage supply was often used to generate the pulsed electric field. Figure 2.5(d) shows the shape of the output voltage pulse for several programmed values of the pulse width Δt_{set} . The rise and fall times are around 2 and 1 ms, respectively, for every value of Δt_{set} . In the following, values of Δt_{set} is simply used to represent the pulse duration. As shown in Fig. 2.5(e), the effect of the shutter of the camera appears in several cases.

¹See the Appendix A for the details about image processing.

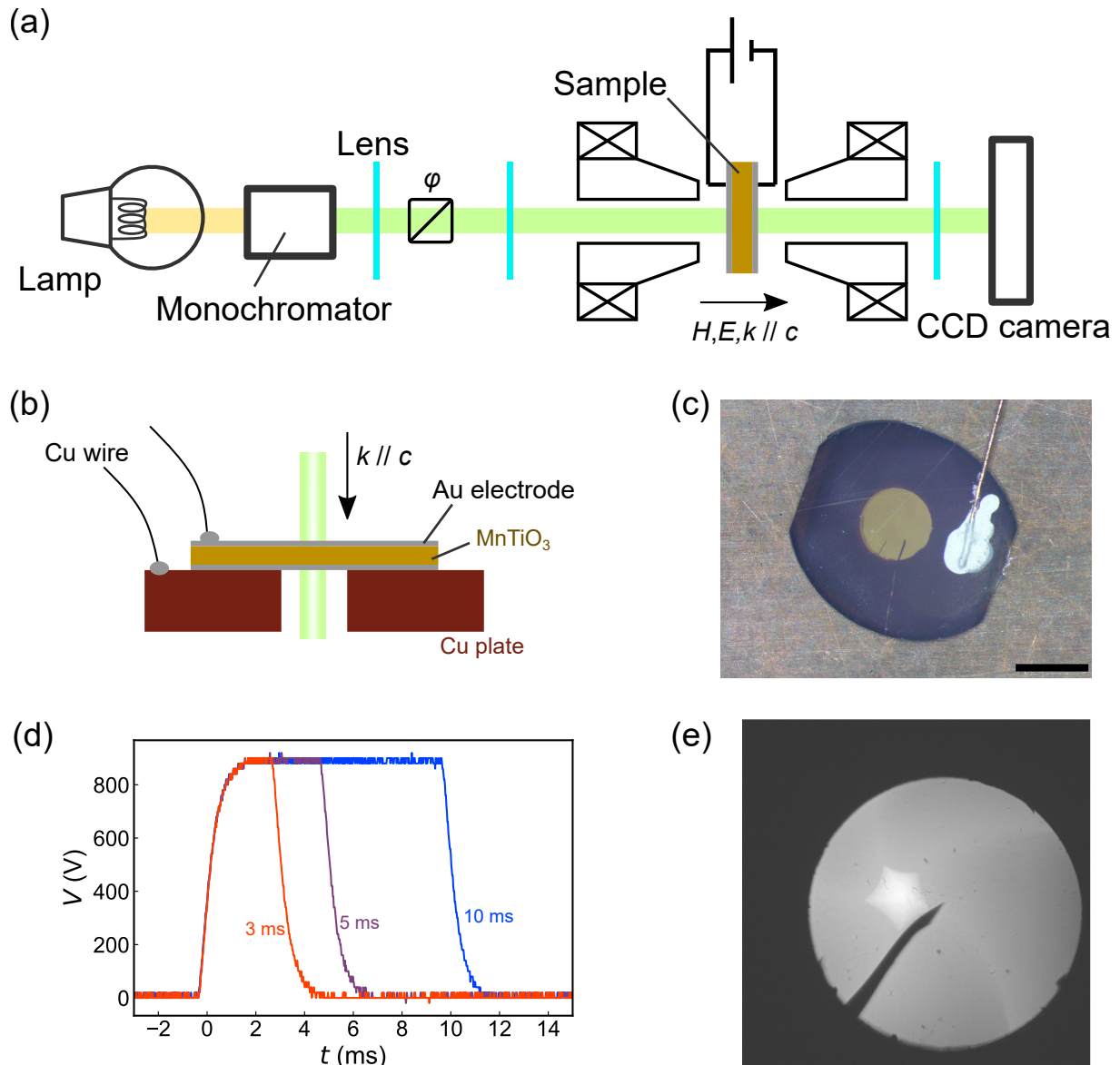


Figure 2.5: (a) Schematic illustration of the setup for the antiferromagnetic domain imaging experiment. See Ch. 4 for the definition of φ . (b) Illustration of the cross sectional view and (c) photograph of the sample placed on the copper plate. In (c), black bar corresponds to 1.4 mm. Circular-shaped optical window in the copper plate placed at the center of the sample appears yellow. (d) Shape of the output pulsed applied voltage for several values of the pulse width. (e) Obtained image where patterns originating from the shutter of the camera is apparent.

Chapter 3

Magneto-chiral Dichroism in MnTiO_3

Magneto-chiral dichroism (MCHD) is the directional dichroism of unpolarized light. Nonreciprocal propagation of light is caused by the toroidal moment \mathbf{T} acting like a rectifier for the light beam. It is now established that the directional dichroism is observed in chiral magnets where \mathbf{T} is induced in proportion to magnetization \mathbf{M} and in polar magnets where \mathbf{T} is induced in proportion to the outer product $\mathbf{P} \times \mathbf{M}$ of electric polarization \mathbf{P} and magnetization. In both cases, intensity of the MCHD signal is proportional to net magnetization of materials. It has remained elusive whether antiferromagnetic ordering with no magnetization can be a source of MCHD in the visible range.

Here, we present the observation of MCHD in a collinear antiferromagnet with zero net magnetization. We show MCHD in antiferromagnetic MnTiO_3 as the difference in absorption coefficients between two configurations where the light beam is parallel and antiparallel to \mathbf{T} . Based on the detailed investigation of the temperature and external-field dependence of the difference spectra, we conclude that observed MCHD spontaneously arises from antiferromagnetic ordering without magnetization. Through the manipulation of \mathbf{T} , binary switching of the absorption coefficient is achieved.

In Sec. 3.1, previous studies of MCHD in noncentrosymmetric magnets are introduced, following phenomenological and microscopic descriptions of MCHD. In Sec. 3.2, magnetic and ME properties of the target material MnTiO_3 are introduced. Section 3.3 is results and discussion. The findings are summarized in Sec. 3.4.

3.1 Introduction to magneto-chiral dichroism

3.1.1 Theory

Phenomenological description

As thoroughly investigated in Ref. [39], symmetry breaking induces specific optical effects. The lack of \mathcal{P} and \mathcal{T} symmetries induces natural circular dichroism (NCD) and magnetic circular dichroism (MCD), respectively. Nonreciprocal directional dichroism (NDD) of unpolarized light

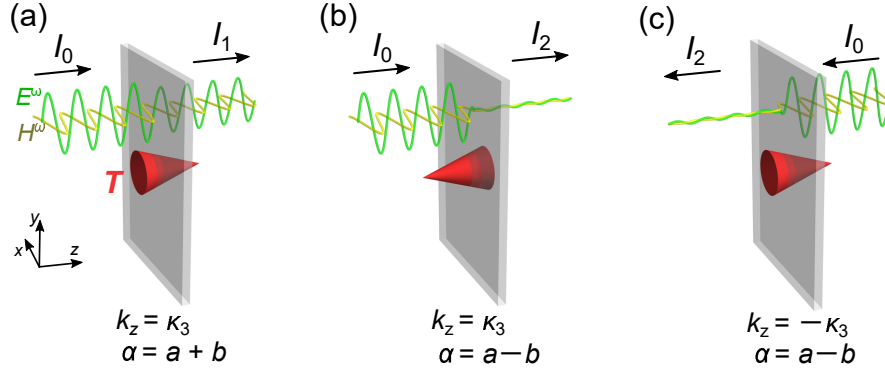


Figure 3.1: Schematic illustrations of MCHD. Red cones represent the toroidal moments \mathbf{T} . Once we set the direction of \mathbf{T} in (a), the directions of (b) and (c) are determined since \mathbf{T} is odd under the \mathcal{P} operation. See the main text for the relation among (a), (b), and (c).

was first discussed as MCHD in the context of the correlation between NCD and MCD induced by simultaneous breaking of \mathcal{P} and \mathcal{T} symmetries [40].

The \mathcal{P} - and \mathcal{T} -odd contribution in the absorption coefficient α is the origin of MCHD. When the propagation vector of incident unpolarized light \mathbf{k} is fixed as $\mathbf{k} = \kappa_3 \mathbf{e}_z$, we can decompose the absorption coefficient α into

$$\alpha = \alpha_{++} + \alpha_{--}, \quad (3.1)$$

where α_{++} (α_{--}) is even (odd) under both \mathcal{P} and \mathcal{T} operations on the sample and the applied static fields on the sample. When incident light of the intensity I_0 propagates through the sample with thickness d and the absorption coefficient $\alpha = a + b$, where $\alpha_{++} = a$ and $\alpha_{--} = b$, the transmitted light intensity I_1 becomes $I_1 = I_0 e^{-(a+b)d}$ [see Fig. 3.1(a)]. After the application of the \mathcal{P} operation on the sample and the static external fields, the absorption coefficient changes to $\alpha = a - b$ while the propagation vector of incident light is unchanged from $\mathbf{k} = \kappa_3 \mathbf{e}_z$ [see Fig. 3.1(b)]. In this situation, the transmitted light intensity becomes $I_2 = I_0 e^{-(a-b)d}$. Figure 3.1(c) displays the situation where the \mathcal{P} operation is applied on the whole system depicted in Fig. 3.1(b) including the sample and incident and transmitted light. The absorption coefficient is invariant under this global \mathcal{P} operation and remains $\alpha = a - b$. The propagation vector \mathbf{k} is reversed in Fig. 3.1(c), compared with those in Figs. 3.1(a) and (b). Since the operation $\hat{\mathcal{P}}^2$ is the identical transformation, in Fig. 3.1(c), the sample is in the same state as in Fig. 3.1(a). From the comparison between Figs. 3.1(a) and (c), we can see that α_{--} is odd under the reversal of the propagation vector of light; the transmitted light intensity changes from I_1 to I_2 just by the change of k_z from κ_3 to $-\kappa_3$. We note that the above discussion holds for the \mathcal{T} operation.

α_{--} and odd-parity magnetic multipoles have a similar symmetry; both quantities are nonzero only when \mathcal{P} and \mathcal{T} symmetries are simultaneously broken. Among three types of magnetic multipoles discussed in Ch. 1, the toroidal moment \mathbf{T} has the exactly same symmetry as MCHD. Let us take MCHD for light propagating along the z direction as example. Since MCHD is the optical effect of unpolarized light, MCHD is symmetric under the C_∞ rotation

around the z axis. Furthermore, MCHD is odd under the two-fold rotation around the x axis which reverses the propagation vector of light. The lowest rank odd-parity magnetic multipole which meets these symmetry requirements is the toroidal moment along the z axis. The directions of toroidal moments are displayed in Figs. 3.1(a)-(c). Here, MCHD is viewed as the rectification effect caused by the toroidal moment, where the absorption coefficient changes depending on the configurations between \mathbf{k} and \mathbf{T} as

$$\alpha(\mathbf{k} \uparrow \uparrow \mathbf{T}) \neq \alpha(\mathbf{k} \uparrow \downarrow \mathbf{T}). \quad (3.2)$$

Here by $\mathbf{k} \uparrow \uparrow \mathbf{T}$ ($\mathbf{k} \uparrow \downarrow \mathbf{T}$), we denote that \mathbf{k} is parallel (antiparallel) to \mathbf{T} .

Formulation

Following the earlier calculation of the magnetic-field induced shift in the absorption coefficient in chiral paramagnets [40] which corresponds MCHD, the formulation of MCHD based on molecular property tensors was presented by Barron *et al.* in 1984 [41]. For unpolarized light propagating along the z direction, α_{++} and α_{--} in Eq. (3.1) are given by

$$\alpha_{++} \propto \text{Im} [\chi_{xx}^e + \chi_{yy}^e], \quad (3.3)$$

and

$$\alpha_{--} \propto \frac{2}{c} \text{Im} \left[\frac{\omega}{3} \{ (A'_{xz})_x + (A'_{yz})_y \} + (\gamma_{xy} - \gamma_{yx}) \right], \quad (3.4)$$

using the dielectric tensor χ^e , the ME tensor γ , and the imaginary quadrupole tensor \mathbf{A}' [see Eqs. (1.27), (1.28), and (1.29)]. For visible light with the photon energy ranging around 1-3 eV, MCHD owes itself to the interference between the electric dipole ($E1$) and the magnetic dipole ($M1$) transitions¹. Substituting Eq. (1.28) for Eq. (3.4), the contribution from the $E1$ - $M1$ interference to α_{--} is given as

$$\begin{aligned} \alpha_{E1-M1} &\propto \frac{2}{c} \text{Im} [\gamma_{xy} - \gamma_{yx}] \\ &= \frac{2}{c} \sum_n \alpha_{E1-M1}^n, \end{aligned} \quad (3.5)$$

where

$$\alpha_{E1-M1}^n = \frac{2\Delta_n \hbar \omega \delta_n}{(\Delta_n^2 - \hbar^2 \omega^2)^2 + \hbar^2 \omega^2 \delta_n^2} \{ \text{Re} (\langle g | \hat{p}_x | e_n \rangle \langle e_n | \hat{m}_y | g \rangle) - \text{Re} (\langle g | \hat{p}_y | e_n \rangle \langle e_n | \hat{m}_x | g \rangle) \}. \quad (3.6)$$

From Eq. (3.4), the microscopic origin of MCHD is traceable to off-diagonal antisymmetric ME coupling in xy -plane, which is related with the z -component of the toroidal moment T_z .

¹MCHD in the x-ray frequency originates from the interference between the $E1$ and the electric quadrupole ($E2$) transitions [42].

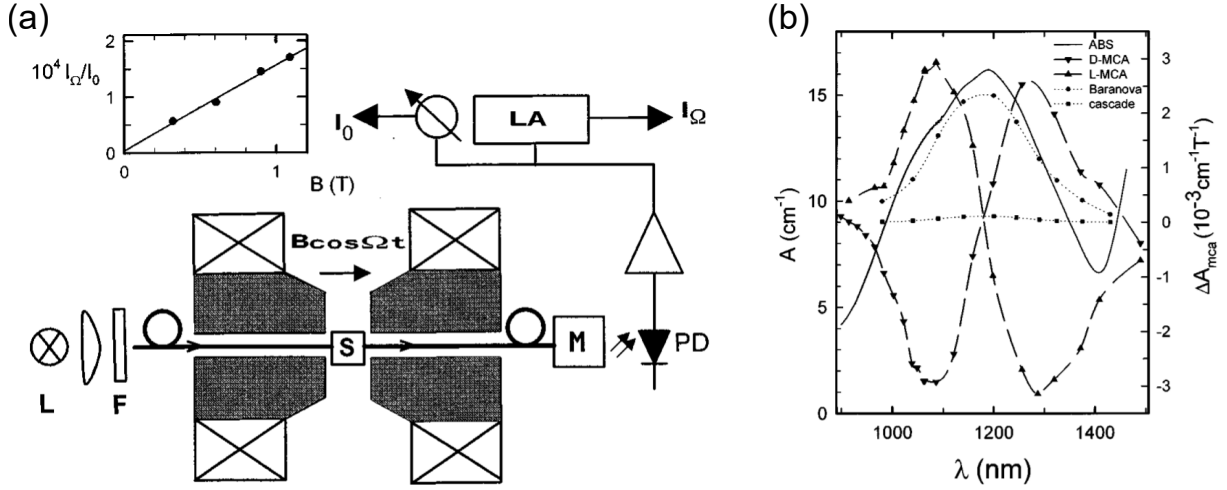


Figure 3.2: (a) Experimental setup for the first experimental observation of MCHD in $\alpha\text{-NiSO}_4\cdot 6(\text{H}_2\text{O})$. L, S, PD, and LA denote the lamp, the sample, the photodiode and the lock-in amplifier, respectively. (b) Absorption (ABS) and MCHD spectra. MCHD spectra is denoted by MCA with the chirality of the sample. Figures are taken from Ref. [43].

3.1.2 Experiment

MCHD in noncentrosymmetric magnets

MCHD was first observed in a chiral material where \mathbf{T} is induced in proportion to \mathbf{M} . For the observation of MCHD, the difference between $\alpha(\mathbf{k} \uparrow \uparrow \mathbf{T})$ and $\alpha(\mathbf{k} \uparrow \downarrow \mathbf{T})$ was measured by switching the direction of \mathbf{M} with keeping \mathbf{k} fixed. The magnetization direction is reversed by switching the direction of magnetic field.

After the observation of the magneto-chiral effect in the form of the directional asymmetry in luminescence [44], Rikken and Raupach reported the first observation of MCHD in $\alpha\text{-NiSO}_4\cdot 6(\text{H}_2\text{O})$ [43]. $\alpha\text{-NiSO}_4\cdot 6(\text{H}_2\text{O})$ crystallizes in a chiral tetragonal structure. Two enantiomers denoted by L and D belong to the space group $P4_12_12$ and $P4_32_12$ [45]. Figure 3.2(a) shows their experimental setup. Experiment was carried out at room temperature where $\alpha\text{-NiSO}_4\cdot 6(\text{H}_2\text{O})$ is in the paramagnetic phase. Unpolarized incident light travelled through the sample and transmitted light intensity were measured by a photodiode. The oscillating magnetic field with frequency Ω was applied along the direction of light. The direction of light was fixed along the c axis of the crystal. Since the toroidal moment also oscillated with Ω , the MCHD signal showed up as the component in transmitted light intensity modulated at Ω . MCHD spectra is shown in Fig. 3.2(b) along with the absorption spectrum. MCHD is observed for both enantiomers. The sign reversal of MCHD for the reversal of chirality is consistent with the \mathcal{P} -odd nature of α_{--- . As shown in the inset of Fig. 3.2(a), the magnitude of MCHD is in proportion to the applied magnetic field.

The nature and origin of MCHD were further clarified by the observation of MCHD in several ferro- and ferrimagnets where \mathbf{M} is not proportional to \mathbf{H} . In 2010, Train *et al.* observed MCHD

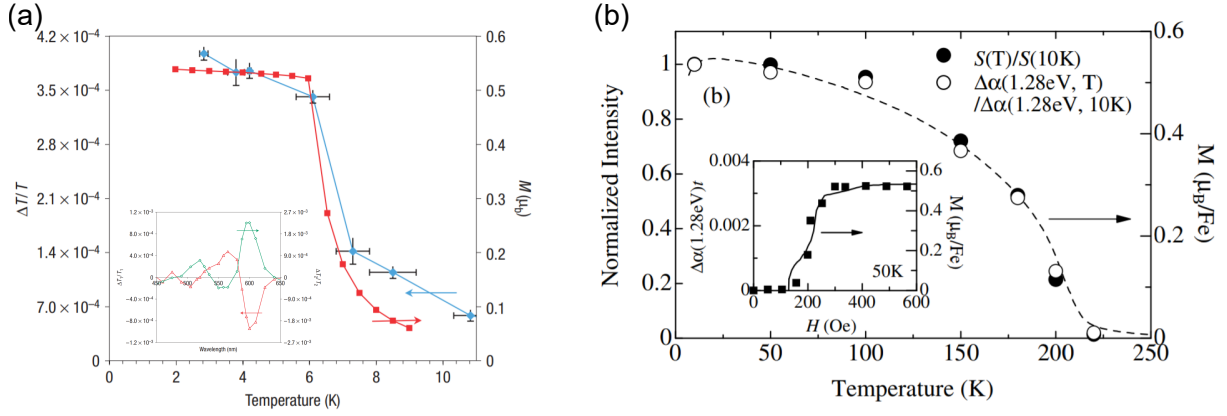


Figure 3: (a) Temperature dependence of the magnitude of the MCHD signal $\Delta T/T$ (red line) and magnetization (blue line) of $[\text{N}(\text{CH}_3)(n\text{-C}_3\text{H}_7)_2((S)\text{-s-C}_4\text{H}_9)][(\Delta)\text{-Mn}(\Lambda)\text{-Cr}(\text{ox})_3]$. Spectra of MCHD is shown in the inset. (b) Temperature dependence of magnetization (dashed line) and the normalized intensity of NDD (black and white circles) in GaFeO_3 . Magnetic field dependence of the magnitude of the NDD signal is shown in the inset. (a) is taken and arranged from Ref. [46]. (b) is taken from Ref. [47].

in chiral ferromagnets below the critical temperature T_c [46]. The temperature dependence of MCHD in a chiral ferromagnet, which was measured as the difference between $\alpha(\mathbf{k} \uparrow \mathbf{H})$ and $\alpha(\mathbf{k} \downarrow \mathbf{H})$, is shown in Fig. 3.3(a). The magnitude of MCHD signal is saturated below $T_c = 7$ K, where switched magnetization is no more than spontaneous magnetization. The result indicates that MCHD in chiral magnets is induced in proportion to magnetization \mathbf{M} , not necessarily to \mathbf{H} .

NDD of unpolarized light arising from the antisymmetric ME coupling has also been studied in an achiral polar magnet GaFeO_3 , where \mathbf{T} is induced in proportion to $\mathbf{P} \times \mathbf{M}$. As described in Sec. 1.1.2, in GaFeO_3 , the combination of spontaneous polarization $\mathbf{P} \parallel \mathbf{b}$ and magnetization $\mathbf{M} \parallel \mathbf{c}$ yields toroidal moment \mathbf{T} along a axis below T_c . In Ref. [47], NDD in GaFeO_3 was measured as the difference between $\alpha(H_c > 0)$ and $\alpha(H_c < 0)$ with keeping $\mathbf{k} \parallel \mathbf{a}$ fixed. As shown in the inset of Fig. 3.3(b), the difference between $\alpha(H_c > 0)$ and $\alpha(H_c < 0)$ was observed with H_c of larger than coercive field where \mathbf{T} is switched. Figure 3.3(b) shows the temperature dependence of the magnitude of the NDD signal and magnetization. The magnitude of NDD behaves similarly to magnetization for the change of temperature; both are negligible above T_c and grows monotonically with decreasing temperature from T_c . In the polar magnet GaFeO_3 , NDD arises when the propagation vector \mathbf{k} is perpendicular to magnetization \mathbf{M} , in sharp contrast with the cases in chiral magnets. The observed NDD in chiral and polar magnets in different configurations are explained in a unified way by regarding the toroidal moment, not magnetization itself, as the rectifier for unpolarized light. These toroidal-moment induced MCHD arises from antisymmetric ME coupling in optical frequency.

MCHD in antiferromagnets

Aside from above mentioned noncentrosymmetric ferro- and ferrimagnets, the toroidal moment can also be activated by spontaneous magnetic ordering in several linear ME antiferromagnets [48, 49, 50, 51, 9]. NDD spontaneously activated by antiferromagnetic ordering with non-zero \mathbf{T} is studied for THz range [52]. Recent observations of MCHD for visible range in chiral antiferromagnets such as CsCuCl₃ and Ni₃TeO₆ [53, 54] is of no antiferromagnetic origin, because the observed MCHD in those chiral antiferromagnets is proportional to the field-induced magnetization as is in the chiral paramagnet. In spite of the novel applications such as electric-field control of color and optical imaging of antiferromagnetic domains [55], MCHD spontaneously arising from antiferromagnetic ordering for visible range is still uncovered.

3.2 Introduction to MnTiO₃

3.2.1 Crystal structure

MnTiO₃ crystallizes in the ilmenite structure in which two-thirds of the octahedral sites of a hexagonal closed packing array of O²⁻ ions are occupied by Mn²⁺ and Ti⁴⁺ cations in an ordered manner [see Figs. 3.4(a) and (b)] [56]. Buckled honeycomb layers of Mn²⁺ with $S = 5/2$ and those of nonmagnetic Ti⁴⁺ alternately stack along the c axis, resulting in the space group $R\bar{3}$. In each honeycomb layer, inversion centers are located at the bond centers of Mn²⁺-Mn²⁺ and Ti⁴⁺-Ti⁴⁺, but not at the atomic sites [see Fig. 3.4(c)]. Mn²⁺ cations are coordinated by six oxygen ions to form octahedral MnO₆ clusters. Mn²⁺ and Ti⁴⁺ cations are located at the Wyckoff position $6c$, where the site symmetry is C_3 .

3.2.2 Magnetic structure

Below the Néel temperature $T_N = 65$ K, MnTiO₃ adopts easy-axis collinear antiferromagnetic ordering in the absence of magnetic field [see Fig. 3.4(c)]. Antiferromagnetic ordering without doubling the unit cell is characterized by a magnetic propagation vector $\mathbf{q}_m = (101)$ [56]. At 4.2 K, the spin-flop transition occurs at the magnetic field $\mu_0 H_c^{\text{SF}}$ of 6 T along the c axis [57]. For $H_c < H_c^{\text{SF}}$, the order parameter is the c component L_c of staggered magnetization $\mathbf{L} = \mathbf{M}_A - \mathbf{M}_B$, where \mathbf{M}_i denotes sublattice magnetization of the sublattice labeled i ($i = A, B$) in Fig. 3.4(c). $L_c > 0$ and $L_c < 0$ states are translationally inequivalent. The magnetic symmetry is $\bar{3}'$. \mathcal{P} and \mathcal{T} symmetries in the paramagnetic phase are simultaneously broken by antiferromagnetic ordering. Since Mn²⁺ on sublattices A and B have magnetic moments in the opposite directions, there no longer exists inversion centers below T_N ; the inversion operation around bond centers transforms the $L_c > 0$ state to the $L_c < 0$ state. The operation $\hat{\mathcal{T}}$ which reverses the direction of magnetic moments also transforms the $L_c > 0$ state to the $L_c < 0$ state. Though \mathcal{P} and \mathcal{T} symmetries are broken, spontaneous polarization and magnetization are zero

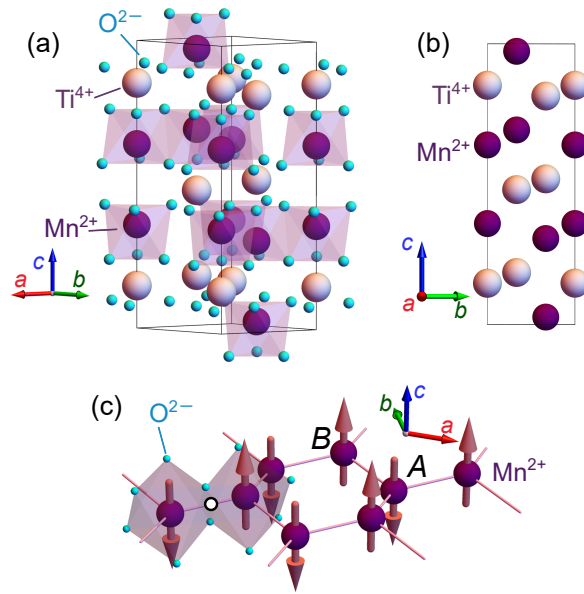


Figure 3.4: (a) Crystallographic structure of and (b) cation ordering in MnTiO₃. (c) Antiferromagnetic ordering in the honeycomb layer of Mn²⁺ consisting of two distinct sublattices labelled *A* and *B*. Arrows represent magnetic moments. A white circle denotes an inversion center.

below T_N due to the preserved \mathcal{PT} symmetry in the antiferromagnetic phase.

3.2.3 Magnetoelectric coupling

The \mathcal{P} - and \mathcal{T} -symmetries-breaking magnetic symmetry $\bar{3}'$ of antiferromagnetic MnTiO₃ allows ME coupling. Taking the x , y , and z axes parallel to the a , b^* , and c axes, respectively, the ME tensor γ for this magnetic symmetry has the form:

$$\gamma = \begin{pmatrix} \gamma_{\perp} & \gamma_t & 0 \\ -\gamma_t & \gamma_{\perp} & 0 \\ 0 & 0 & \gamma_{\parallel} \end{pmatrix}. \quad (3.7)$$

The c component of magnetic-field induced polarization $P_c = \gamma_{\parallel} H_c$ is displayed in Fig. 3.5(a). P_c is absent above T_N and in 0 T. The magnetic-field induced contribution appears below T_N . As shown in Fig. 3.5(b), P_c is induced in proportion to H_c below H_c^{SF} at 50 K. In-plane ME effects $P_a = \gamma_{\perp} H_a$ and $P_a = \gamma_t H_{b^*}$ are not reported yet.

Optical ME coupling arising from the antisymmetric component γ_t in Eq. (3.7) is the microscopic origin MCHD. From Eqs. (1.6) and (1.10), γ_t is proportional to the c component of the toroidal moment T_c as

$$\gamma_t = bT_c, \quad (3.8)$$

where b denotes the coupling constant. The other two components γ_{\perp} and γ_{\parallel} are related with the magnetic monopole and the q_{z^2} -type magnetic quadrupole [see Eqs. (1.6) and (1.10)]. Since

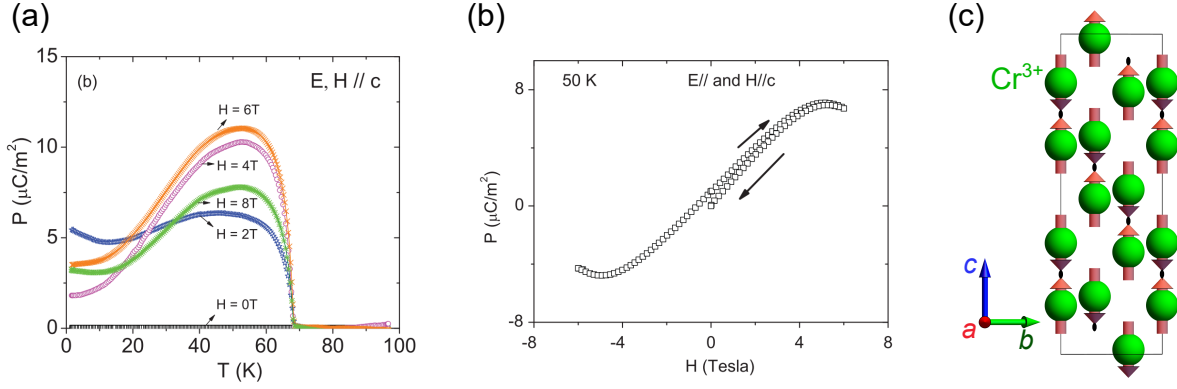


Figure 3.5: (a) Temperature and (b) magnetic-field dependence of P_c in MnTiO₃ in $\mathbf{H} \parallel \mathbf{c}$ [13]. (c) Antiferromagnetic structure of Cr₂O₃ projected along the a axis. Black symbols denote twofold rotation axes along the a axis. (a) and (b) are taken from Ref. [13].

the ME tensor elements are odd to operations $\hat{\mathcal{P}}$ and $\hat{\mathcal{T}}$ as the order parameter L_c is in MnTiO₃, the leading term in the expansion of γ_{\perp} , γ_t , and γ_{\parallel} by L_c becomes

$$\begin{cases} \gamma_{\perp} = g_{\perp} L_c \\ \gamma_t = g_t L_c \\ \gamma_{\parallel} = g_{\parallel} L_c \end{cases}, \quad (3.9)$$

with the temperature dependent expansion coefficients g_{\perp} , g_t , and g_{\parallel} . From Eq. (3.9), two antiferromagnetic states with L_c of opposite signs are characterized by the ME tensor of opposite signs. Combining Eqs. (3.8) and (3.9), relation between the toroidal moment and the order parameter is obtained as

$$T_c = \frac{g_t}{b} L_c. \quad (3.10)$$

In MnTiO₃, the c -component of the toroidal moment is proportional to that of the staggered magnetization.

Cation ordering between Mn²⁺ and Ti⁴⁺ is crucial for the presence of γ_t in MnTiO₃. The corundum structure can be regarded as the disordered ilmenite structure. For example, in Cr₂O₃ with the corundum structure, two distinct cation sites in the ilmenite structure are both occupied by Cr³⁺. In this case, collinear antiferromagnetic ordering similar to that in MnTiO₃ [see Fig. 3.5(c)] [58, 59], gives rise to the ME tensor in Eq. (1.11), where the antisymmetric term is absent. Comparing Fig. 3.5(c) with Fig. 3.4(c), the two-fold rotational axis along the a axis, which transforms γ_t to $-\gamma_t$ and $T_c > 0$ to $T_c < 0$, is broken in MnTiO₃ with the ilmenite structure.

3.3 Results and discussion

3.3.1 In-plane magnetoelectric coupling and polarization switching

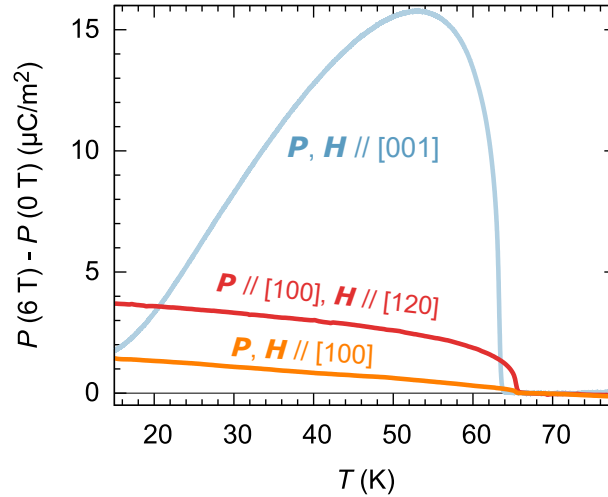


Figure 3.6: Temperature dependence of magnetic-field induced electric polarization P in MnTiO_3 in the absence of electric field E . To extract the magnetically induced P , P in 0 T is subtracted from that in $\mu_0 H_c = 6$ T. Before each measurement, the sample was cooled down from 90 K in the poling electric field $E_{\text{poling}} > 0.08$ MV/m. Data are from Ref. [60].

The temperature dependence of magnetic-field induced electric polarization in MnTiO_3 is shown in Fig. 3.6. Aside from the previously reported component $P_c = \gamma_{\parallel} H_c$ [13], magnetic-field induced polarization arising from the in-plane ME coupling $P_a = \gamma_{\perp} H_a$ and $P_a = \gamma_t H_b^*$ is observed. The values of the in-plane ME susceptibilities at 55 K are estimated to be $\gamma_{\perp} = 0.1$ and $\gamma_t = 0.7$ ps/m, which are smaller than the out-of-plane susceptibility $\gamma_{\parallel} = 3.2$ ps/m. Reflecting the uniaxial magnetic anisotropy, the temperature dependence of γ_t and γ_{\perp} is different from that of γ_{\parallel} ; the former grows monotonically with cooling, while the latter takes its maximum at 53 K and goes down to zero with decreasing temperature below 53 K. The anisotropy of the ME effect is similar to that in Cr_2O_3 with similar crystallographic and antiferromagnetic structures, where anisotropic ME coupling is explained based on the magnetic anisotropy [22].

The linear relationship between P_c and H_c for two distinct states with $\gamma_{\parallel} > 0$ and $\gamma_{\parallel} < 0$ is shown in Fig. 3.7(a). Prior to the measurement for $E_{\text{poling}} > 0$ ($E_{\text{poling}} < 0$), an electric field E_{poling} of 1.1 MV/m (-1.1 MV/m) was applied along the c axis in a magnetic field $\mu_0 H_c = 6$ T at 55 K. Considering the relevant free energy component $\mathcal{F}_{\text{ME}} = -\gamma_{\parallel} E_c \mu_0 H_c$ [see Eq. 1.6], $\gamma_{\parallel} > 0$ and $\gamma_{\parallel} < 0$ states are favored for $E_c H_c > 0$ and $E_c H_c < 0$, respectively. As seen in Eq. (1.10) the conjugate field for the toroidal moment \mathbf{T} is $\mathbf{E} \times \mathbf{H}$ [3, 61]. In MnTiO_3 , $E_c H_c$ -induced switching of $\mathbf{T} \parallel \mathbf{c}$ is made possible by the coupling between T_c and the q_{22} -type magnetic quadrupole and magnetic monopole, whose conjugate field includes the product $E_c H_c$. After the poling process, the electric field was turned off and polarization was measured in magnetic-field decreasing

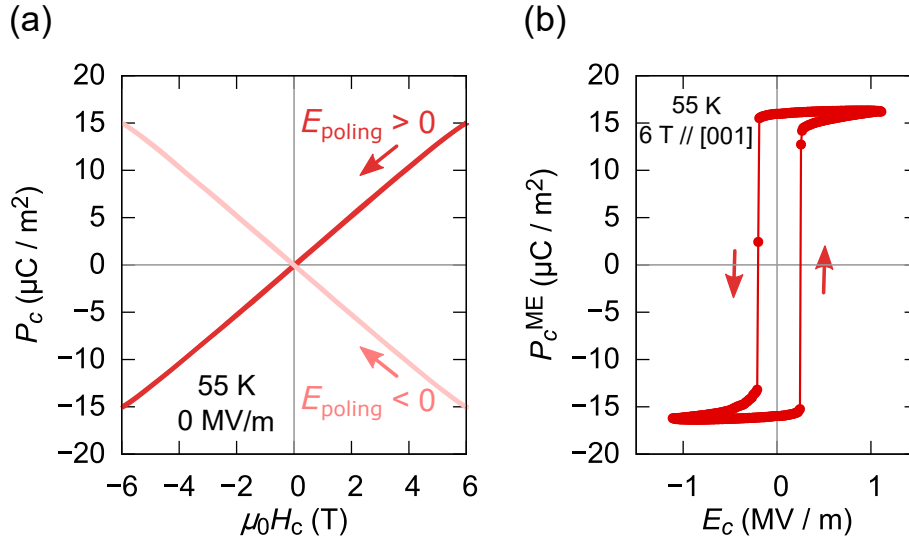


Figure 3.7: (a) Magnetic-field dependence of P_c in MnTiO₃ in the absence of E . (b) Ferroelectric hysteresis loop of the magnetically induced component of P_c in $\mu_0 H_c = 6 \text{ T}$. The electric field-induced polarization, i.e. the dielectric polarization, is assumed to be linear to E_c and subtracted from the measured P_c . Data are from Ref. [60].

runs. The magnetic-field induced polarization $15 \mu\text{C}/\text{m}^2$ at $\mu_0 H_c = 6 \text{ T}$ and 55 K is in good agreement with magnetic-field induced P_c at 55 K in Fig. 3.6. The linear P_c - H_c relationship up to $\mu_0 H_c = 6 \text{ T}$ at 55 K indicates the absence of the spin-flop transition below 6 T, which should accompany the change in magnetic symmetry from $\bar{3}'$ to $\bar{1}'$ and consequent discontinuous jump in magnetic-field induced polarization. Considering the coupling between γ_{\parallel} and L_c [see Eq. (3.9)], the sign reversal of γ_{\parallel} indicates that obtained two P_c - H_c curves correspond to $L_c > 0$ and $L_c < 0$ states. The E_c -driven reversal of magnetically induced polarization in $\mu_0 H_c = 6 \text{ T}$ is further investigated. Ferroelectric switching of $P_c^{\text{ME}} = \mu_0 H_c$ is shown in Fig. 3.7(b). The value of residual polarization of $15 \mu\text{C}/\text{m}^2$ at $E_c = 0 \text{ MV/m}$ in Fig. 3.7(b) is consistent with that of P_c induced by the magnetic field of $\mu_0 H_c = 6 \text{ T}$. It is clearly shown that, at 55 K, an electric field of 0.25 MV/m isothermally switches the magnetically induced polarization. The value of the coercive electric field is comparable to that in Cr₂O₃ [35]. Figure 3.7(b) evidences L_c and T_c not only γ are isothermally switchable by reversing the direction of the electric field in a fixed magnetic field ².

3.3.2 Observation of magneto-chiral dichroism

Absorption spectra

Figure 3.8(a) shows the absorption spectrum of MnTiO₃. As reported previously [62], two absorption bands are observed; a peak at 2.15 eV and the monotonic increase above 2.4 eV. The former peak position of around 2.15 eV is comparable with that in other manganese compounds

²See the Appendix B for the possible origin of the toroidal moment in MnTiO₃.

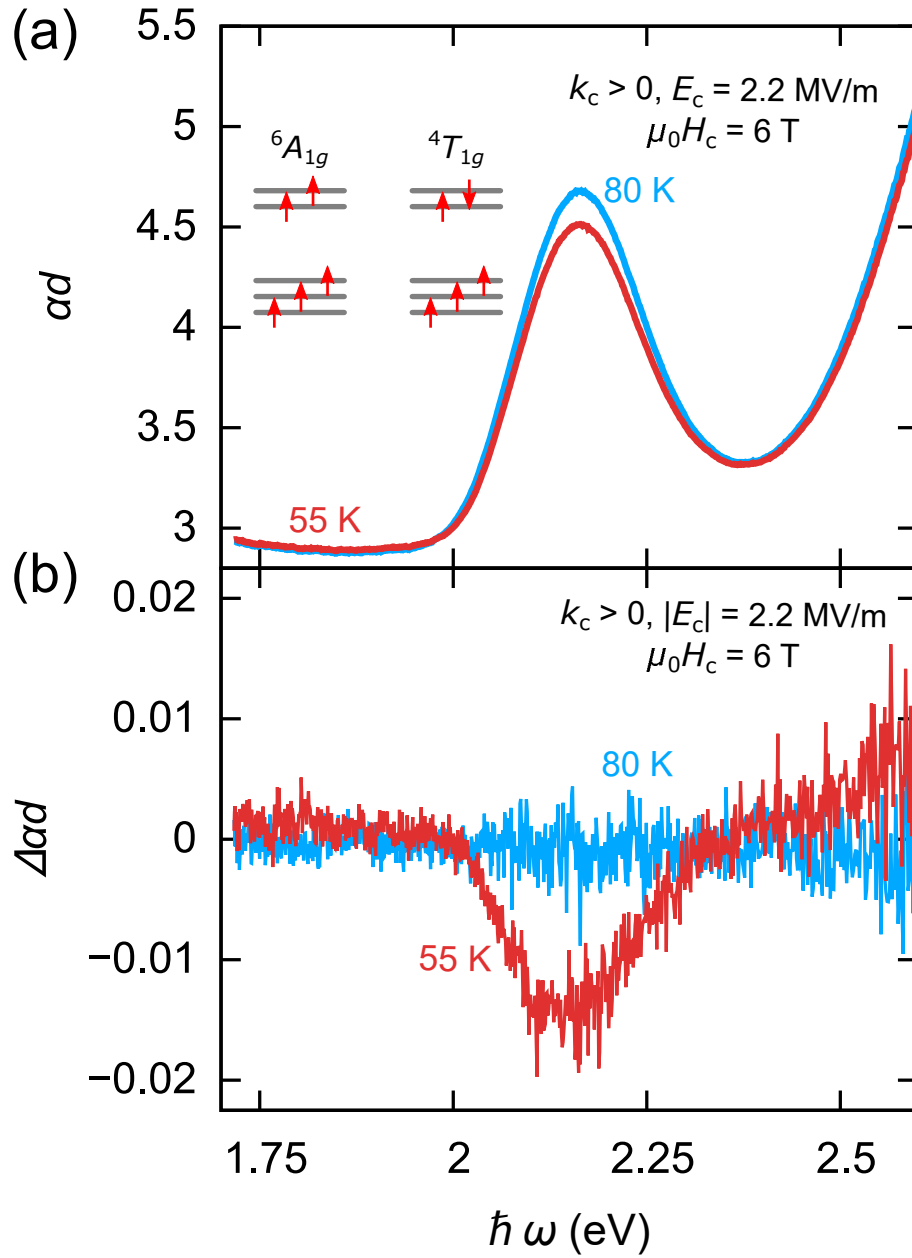


Figure 3.8: (a) Absorption spectra of MnTiO₃ at 55 K and 80 K in $\mu_0 H_c = 6$ T and $E_c = 2.2$ MV/m. Schematic electronic diagrams for the ${}^6A_{1g}$ ground state and the ${}^4T_{1g}$ excited state are shown in the inset. $\hbar\omega$ denotes the photon energy. (b) Difference spectra $\Delta\alpha d = \alpha d(E_c > 0) - \alpha d(E_c < 0)$ at 55 K and 80 K in $\mu_0 H_c = 6$ T. Data are from Ref. [60].

of 1.9 - 2.2 eV where Mn²⁺ ions are octahedrally coordinated by six anions [63, 64, 65]. The absorption peak is assigned to the intra-atomic $d-d$ excitation from the ${}^6A_{1g}$ ground state to the ${}^4T_{1g}$ excited state of octahedrally coordinated Mn²⁺ with five electrons in d orbitals [66]. The peak width of more than 0.1 eV would be due to the vibronic contribution to the transition, where the relevant zero-phonon line is reported at 1.88 eV [62]. The increase in α above 2.4 eV is ascribed to the transition to the ${}^4T_{2g}$ excited state possibly overlapped with the charge transfer excitation from O $2p$ to Mn $3d$ [62].

Verification of MCHD signal

To verify the MCHD in MnTiO₃, we investigate the difference in the absorption coefficient between two configurations $\alpha(\mathbf{T} \uparrow \uparrow \mathbf{k})$ and $\alpha(\mathbf{T} \uparrow \downarrow \mathbf{k})$. We switch the direction of \mathbf{T} with keeping \mathbf{k} fixed by the reversal of E_c between ± 2.2 MV/m in a magnetic field of $\mu_0 H_c = 6$ T. Figure 3.8(b) shows the difference spectra $\Delta\alpha d = \alpha d(E_c > 0) - \alpha d(E_c < 0)$. The electric field of 2.2 MV/m is large enough to fully switch \mathbf{T} [see Fig. 3.7(b)]. In Fig. 3.8(b), at 55 K, the dip is observed around 2.15 eV. Since the difference between $\alpha d(E_c > 0)$ and $\alpha d(E_c < 0)$ is absent at 80 K $> T_N$, it is clear that antiferromagnetic ordering is crucial for the electrochromic effect at 55 K.

To confirm that the observed electrochromic effect reflects the difference between $\alpha(\mathbf{k} \uparrow \uparrow \mathbf{T})$ and $\alpha(\mathbf{k} \uparrow \downarrow \mathbf{T})$, we investigate the difference spectra with changing the direction of \mathbf{k} and \mathbf{H} . As shown in Figs. 3.9(a) and (b), the electrochromic effect changes its sign under the reversal of the magnetic field. For $k_c > 0$, in $\mu_0 H_c = -6$ T, the peak of $\Delta\alpha d$ is observed at 2.15 eV, at which energy the dip appears in $\mu_0 H_c = 6$ T [see Fig. 3.9(a)]. The reversal of the electrochromic effect for the reversal of H_c indicates the following relation

$$\begin{aligned} \Delta\alpha(H_c > 0) &= -\Delta\alpha(H_c < 0) \\ \Leftrightarrow \alpha(E_c > 0, H_c > 0) - \alpha(E_c < 0, H_c > 0) &= -\alpha(E_c > 0, H_c < 0) + \alpha(E_c < 0, H_c < 0) \neq 0. \end{aligned} \quad (3.11)$$

Since the E_c of 2.2 MV/m is large enough to switch T_c in $\mu_0 H_c = 6$ T at 55 K, the sign of T_c is in one-to-one correspondence with the sign of the product $E_c H_c$. Assuming bg_{\parallel}/gt to be positive [see Eqs. (3.8), and (3.9)], the $T_c > 0$ state is realized for $E_c H_c > 0$, while the $T_c < 0$ state is realized for $E_c H_c < 0$. Here the relation Eq. (3.11) leads to

$$\Delta\alpha(H_c > 0) = \alpha(T_c > 0) - \alpha(T_c < 0) \neq 0 \quad (3.12)$$

for $k_c > 0$.

Comparing Figs. 3.9(a) and (b), we can see that the observed electrochromic effect also changes its sign for the reversal of the propagation vector \mathbf{k} . In $\mu_0 H_c = 6$ T, for $k_c < 0$ the peak of $\Delta\alpha d$ is observed at 2.15 eV, at which energy the dip appears for $k_c > 0$. Incorporating the

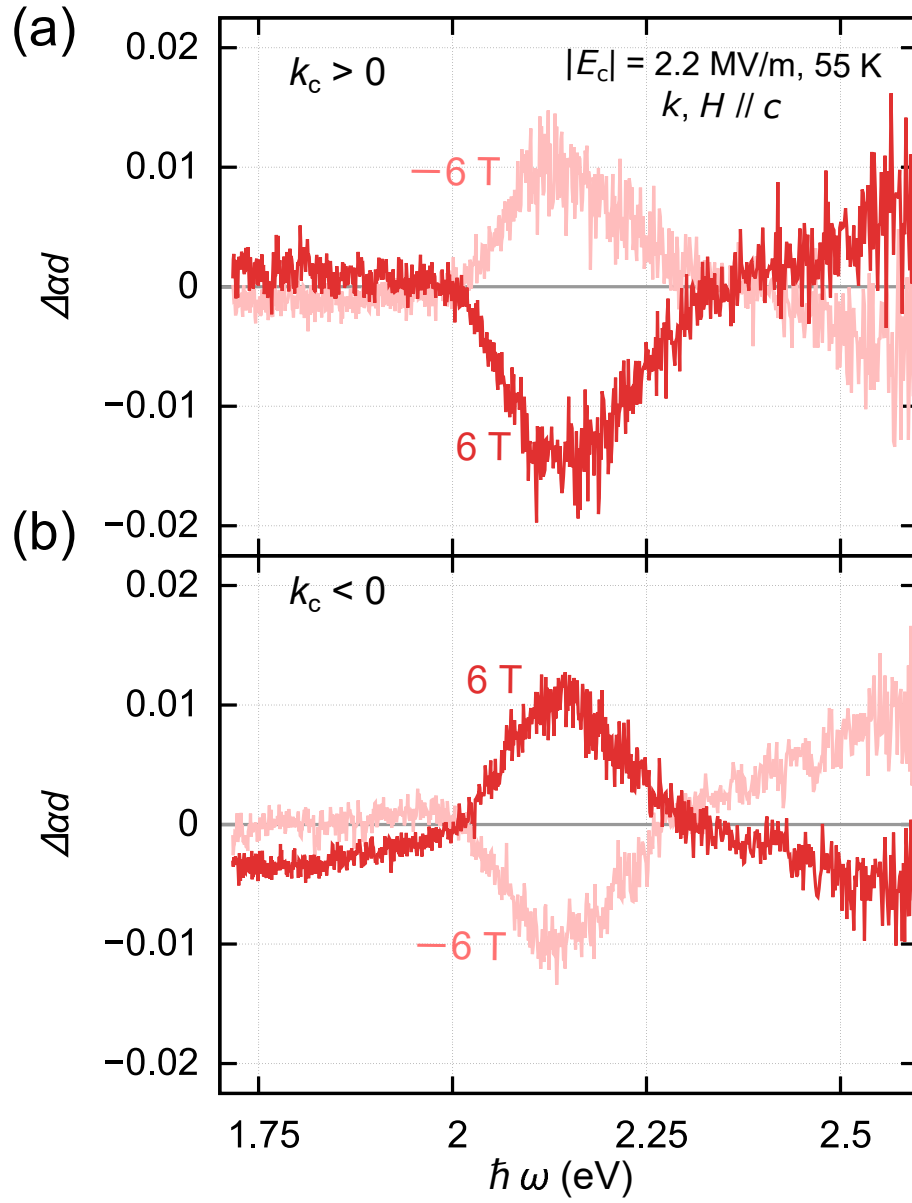


Figure 3.9: The variation of the difference spectra $\Delta\alpha d = \alpha d(E_c > 0) - \alpha d(E_c < 0)$ for the reversal of magnetic field and the propagation vector of light \mathbf{k} at 55 K. Data are from Ref. [60].

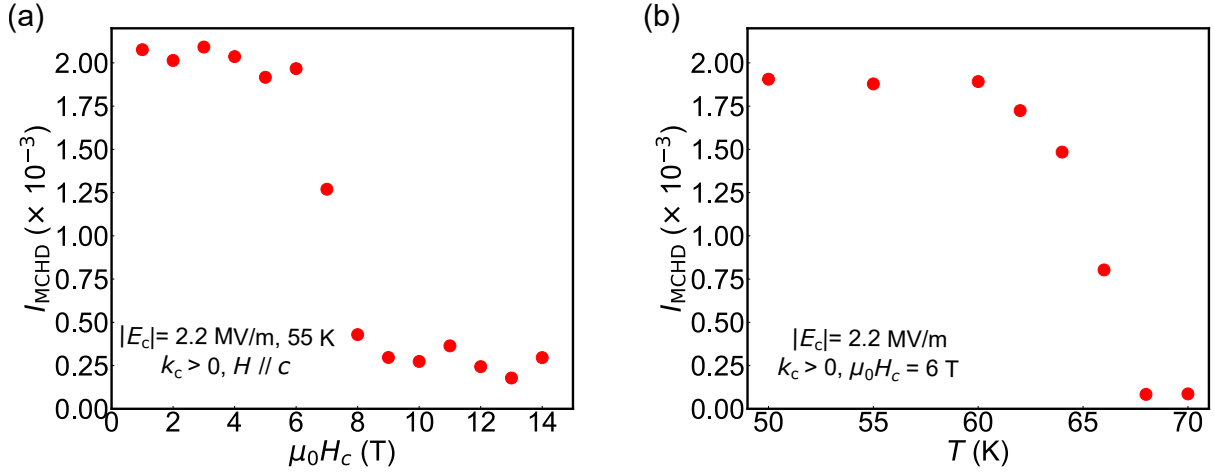


Figure 3.10: (a) Magnetic-field and (b) temperature dependence of the MCHD intensity I_{MCHD} around 2.15 eV.

the reversal of $\Delta\alpha d$ for the reversal of \mathbf{k} , Equation (3.12) becomes

$$\begin{aligned} \Delta\alpha(H_c > 0, k_c > 0) &= -\Delta\alpha(H_c > 0, k_c < 0) \\ \Leftrightarrow \alpha(T_c > 0, k_c > 0) - \alpha(T_c < 0, k_c > 0) &= -\alpha(T_c > 0, k_c < 0) + \alpha(T_c < 0, k_c < 0) \neq 0 \end{aligned} \quad (3.13)$$

Equation (3.13) represents nothing but the directional dichroism; the absorption coefficient depends whether \mathbf{k} is parallel or antiparallel to the toroidal moment \mathbf{T} . At this stage, we conclude that the observed \mathbf{k} - and \mathbf{H} - odd electrochromic effects in MnTiO₃ are ascribed to the MCHD.

Detailed investigation of MCHD

The magnetic-field and temperature dependence of the magnitude of the MCHD signal I_{MCHD} is shown in Figs. 3.10(a) and (b). I_{MCHD} is computed as $I_{\text{MCHD}} = |\int_{2.0\text{eV}}^{2.3\text{eV}} \Delta\alpha d\omega|$, using $\Delta\alpha d = \alpha d(E_c > 0) - \alpha d(E_c < 0)$. Judging from Fig. 3.10(a), the magnitude of the MCHD signal at 55 K is independent of the magnetic field below $\mu_0 H_c^{\text{SF}} = 6.4$ T. The spin-flop transition at H_c^{SF} accompanies a discontinuous decrease in I_{MCHD} . Staggered ordering of the c -component of magnetic moments, which is absent above $\mu_0 H_c^{\text{SF}}$, would be a major source of MCHD in MnTiO₃.

We compare the temperature dependence of the MCHD signal with the relevant antisymmetric ME effect in DC frequency. As seen in Fig. 3.10(b), I_{MCHD} decreases as the temperature increases from 60 K to T_N . Below 60 K, I_{MCHD} looks independent on the temperature. The behavior of I_{MCHD} below 60 K is not in agreement with that of $P_a = \gamma_t H_{b^*}$, which monotonically increases as decreasing temperature below T_N down to 15 K [see Fig. 3.6]. Substituting $\omega = 0$ for Eq. (1.28), the ME tensor γ in DC frequency is approximately obtained as,

$$\gamma_{\mu\nu}(\omega = 0) \propto \sum_n \frac{2\text{Re}(\langle g|\hat{p}_\mu|e_n\rangle \langle e_n|\hat{m}_\nu|g\rangle)}{\Delta_n}. \quad (3.14)$$

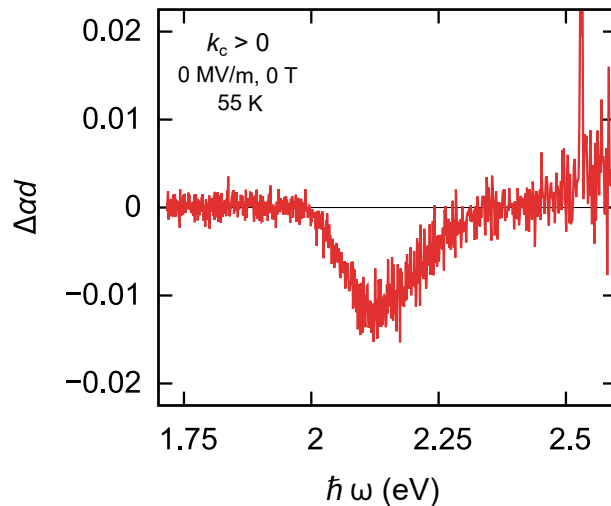


Figure 3.11: Difference spectrum at 55 K measured in the absence of external electric and magnetic fields. Data are from Ref. [60].

From Eq. (3.14), the monotonic growth of γ_t with decreasing the temperature is ascribed to the growth of $\text{Re}(\langle g|\hat{p}_\mu|e_n\rangle\langle e_n|\hat{m}_\nu|g\rangle)$ at lower temperature. At this stage, the discrepancy in the temperature dependence of the MCHD signal and the antisymmetric ME effect $P_a = \gamma_t H_b^*$ is attributable to the existence of temperature dependency of in the phenomenological damping parameter δ_n in Eq. (3.6). The vibronic contribution to the damping parameter should be suppressed at low temperatures. The temperature invariant behavior in I_{MCHD} below 60 K would be the result of monotonic growth of the $\text{Re}(\langle g|\hat{p}_x|e_n\rangle\langle e_n|\hat{m}_y|g\rangle) - \text{Re}(\langle g|\hat{p}_y|e_n\rangle\langle e_n|\hat{m}_x|g\rangle)$ compensated by the suppression of δ_n . We note that vibronic coupling is recently found to play a key role for MCHD [67].

To confirm that MCHD in MnTiO_3 is a spontaneous effect arising from antiferromagnetic ordering and not a field-induced effect, we investigate the MCHD signal in the absence of electric and magnetic fields. Figure 3.11 shows the difference spectra $\Delta\alpha d = (\alpha_+ - \alpha_-)d$ at 55 K measured in the absence of electric and magnetic fields. Before measuring α_+d (α_-d), the electric field of $E_c = 2.2$ MV/m was applied in a magnetic field of $\mu_0 H_c = 1$ (-1) T. Judging from I_{MCHD} at 1 T in Fig. 3.10(a), E_c of 2.2 MV/m is large enough to reverse the direction of \mathbf{T} even in the magnetic field of $\mu_0 H_c = 1$ T. $\alpha_+ - \alpha_-$ represents the difference in the absorption coefficient between $\mathbf{k} \uparrow \uparrow \mathbf{T}$ and $\mathbf{k} \uparrow \downarrow \mathbf{T}$ configurations in the absence of external fields. The dip at 2.15 eV in Fig. 3.11 clearly evidences that MCHD in MnTiO_3 is observed in the absence of external fields. MCHD in a collinear antiferromagnet is a spontaneous effect which originates from antiferromagnetic ordering and appears in zero net magnetization, in sharp contrast with the magnetic-field induced MCHD in chiral antiferromagnets [53, 54]. Using the sample thickness $d = 90$ μm , the difference $\Delta\alpha d \sim 0.01$ at 2.15 eV in Fig. 3.11 corresponds to α_{--} of 0.56 cm^{-1} .

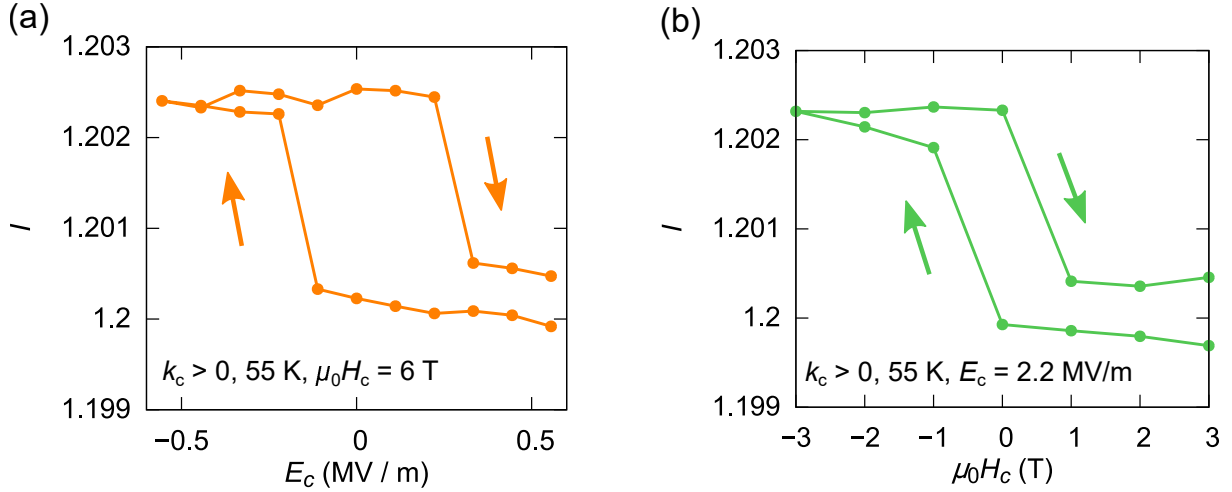


Figure 3.12: (a) Electric and (b) magnetic fields dependence of the αd integrated over 2.0 - 2.3 eV, $I = \int_{2.0\text{eV}}^{2.3\text{eV}} \alpha d\omega$. Data are from Ref. [60].

Binary switching of color

In Figs. 3.12 (a) and (b), we demonstrate binary switching in the absorption coefficient around 2.15 eV, where the MCHD is evidently seen, by the isothermal cyclic reversal of electric and magnetic fields. The integrated absorption intensity I is switched between $I \sim 1.202$ and $I \sim 1.200$ by switching the direction of \mathbf{T} for $k_c > 0$. The electric and magnetic fields control of the absorption coefficient is achieved through the control of \mathbf{T} . In Fig. 3.12 (a), the coercive electric field to switch I is around 0.25 MV/m at 55 K in $\mu_0 H_c = 6$ T, comparable with the value in the $P_c^{\text{ME}} - E_c$ loop [see Fig. 3.7(b)]. For the magnetic-field induced switching of I at 55 K in $E_c = 2.2$ MV/m, the coercive magnetic field is around 0.5 T. Threshold fields to switch I is consistent with each other; both indicates that the product $E_c H_c$ of roughly 1 TW/m^2 is required to switch \mathbf{T} , which corresponds to ME free energy $\gamma_{\parallel} E_c H_c$ of 1 neV/f.u. in Eq. (3.7). Above the threshold field, I is nearly independent of the strength of the external electric and magnetic fields.

3.3.3 Microscopic origin of MCHD in MnTiO₃

Microscopic origin of MCHD in MnTiO₃ is discussed in view of chirality and magnetization of each MnO₆ cluster. We neglect the contribution from TiO₆ cluster because the intra-atomic $d-d$ excitation is absent in Ti⁴⁺ with d^0 electronic configuration. As shown in Fig. 3.4(c), each antiferromagnetic honeycomb layer consists of two kinds of sublattices labeled A and B . Considering the site symmetry C_3 at Mn²⁺ sites, each MnO₆ cluster in itself has chirality. Two edge-sharing MnO₆ clusters, one on sublattice A and the other on sublattice B , are connected with each other by \mathcal{P} operation which inverts chirality. When we regard the chirality of MnO₆ clusters on sublattice A as left-handed, MnO₆ clusters on sublattice B has right-handed structure [see Fig. 3.13]. Below T_N , each MnO₆ cluster can be viewed as a chiral object magnetized along

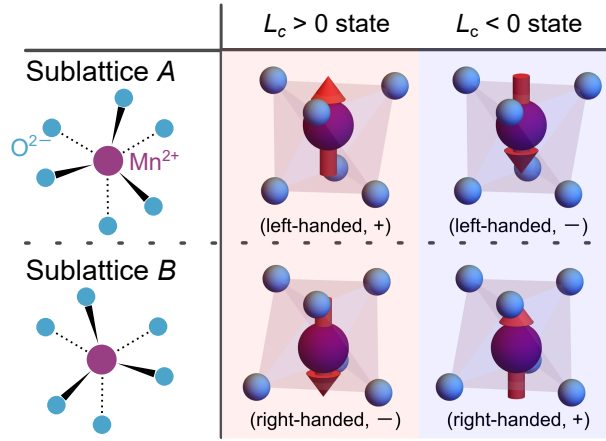


Figure 3.13: Relation among the coordination environment, local magnetization (+/-), and the sign of MCHD of each MnO_6 cluster. Pairs of two MnO_6 clusters with the same sign of MCHD are shaded with the same color. Schematic top view of each MnO_6 cluster along the c axis is shown in the left column. Purple and blue spheres represent Mn^{2+} and O^{2-} ions, respectively. Arrows on Mn^{2+} ions represent magnetic moments. Chirality of each cluster is denoted by left- and right- handed, regarding that MnO_6 cluster on sublattice A has left-handed structure.

ordered moments of Mn^{2+} ions. Once the sign of the order parameter L_c is fixed, the direction of the magnetic moments is in one-to-one correspondence with the sublattice which MnO_6 cluster belongs to [see Fig. 3.13]; MnO_6 clusters with opposite chirality always magnetized in opposite direction. As pointed out in Ch. 1, in chiral materials, the toroidal moment \mathbf{T} is induced parallel to magnetization as $\mathbf{T} = \eta_{TM}\mathbf{M}$, where the sign of coefficient η_{TM} reverses for the reversal of chirality. Staggered ordering of magnetic moments in concert with staggered ordering of chirality make all the MnO_6 clusters host \mathbf{T} of the same direction, which constructively contribute to the MCHD in antiferromagnetic MnTiO_3 . The toroidal moment on each MnO_6 cluster switches the direction for the reversal of the order parameter L_c and the MCHD signal consequently changes its sign, as illustrated in Fig. 3.14. We note that polarity of MnO_6 clusters along the c axis does not give rise to MCHD because the product $\mathbf{P} \times \mathbf{M}$ is zero when magnetic moments are along the c axis.

Contribution from each MnO_6 cluster to MCHD is understood by the analysis of the d - d excitation. MCHD in MnTiO_3 is prominently seen for the incident photon energy $\hbar\omega$ of around 2.15 eV, which resonate with the intra-atomic d - d excitation in octahedrally coordinated Mn^{2+} ions. The observed peak-shaped spectra of MCHD coincides with what is expected from Eq. (3.5). Localized nature of the excitation allows us to discuss the transition taking only the d^5 electronic configuration of the single Mn^{2+} ion into account. The group theoretical consideration tells us a little detail about the excited and ground states involved in the $E1$ - $M1$ interference responsible for MCHD. The $S = 5/2$ ground state ${}^6A_{1g}$ belong to the irreducible representation (irrep) A of the point group C_3 . For light propagating along the c axis, both $E1$ and $M1$ terms $\hat{\mathbf{p}} \cdot \mathbf{E}^\omega$ and $\hat{\mathbf{m}} \cdot \mathbf{B}^\omega$ [see Eq. (1.25)], respectively, belong to irrep E in C_3 . Therefore, for

$\text{Re}(\langle g|\hat{p}_x|e_n\rangle\langle e_n|\hat{m}_y|g\rangle) - \text{Re}(\langle g|\hat{p}_y|e_n\rangle\langle e_n|\hat{m}_x|g\rangle)$ to be not zero, the $|e_n\rangle$ must belong to irrep E of C_3 . The relevant $S = 3/2$ excited state $|e_n\rangle$ for $\Delta_n = 2.15$ eV belongs to irrep T_{1g} of the point group O_h . If the MnO_6 cluster is an undistorted regular octahedron, this ${}^4T_{1g}$ states are triply degenerated in orbital degree of freedom³. In the trigonal C_3 symmetry at the Mn^{2+} sites in MnTiO_3 , the degeneracy is lifted and the ${}^4T_{1g}$ states split into two levels; one belongs to irrep E of C_3 and the other belongs to irrep A of C_3 . MCHD at 2.15 eV originates from the transition to the 4E states of C_3 which is derived from the ${}^4T_{1g}$ state of O_h .

Orbital part of the magnetic dipole operator $\hat{\mathbf{m}}_L = -\mu_B\hat{\mathbf{l}}/\hbar$ usually accounts for the $M1$ transition of the $d-d$ excitation. Hereafter, by $|e_{n,\alpha}^0\rangle$ we denote the n -th eigenstate of $\mathcal{H}_{\text{el-el}} + \mathcal{H}_{\text{CEF}}$, where $\mathcal{H}_{\text{el-el}}$ and \mathcal{H}_{CEF} denote the on-site Coulomb interaction and the crystal field. $\alpha = 1 \cdots N_n$ stand for the degeneracy. $n = 0$ corresponds to the ground state. Since $\mathcal{H}_{\text{el-el}} + \mathcal{H}_{\text{CEF}}$ commutes with the position operator $\hat{\mathbf{r}}$, real part of $\langle e_{i\alpha}| \hat{p}_\mu | e_{j\beta} \rangle \langle e_{j\beta} | \hat{m}_{L\nu} | e_{i\alpha} \rangle$ is always zero for all possible i, j, α, β, μ , and ν .

By taking spin-orbit coupling \mathcal{H}_{SO} into account, $\langle e_{i\alpha}| \hat{p}_\mu | e_{j\beta} \rangle \langle e_{j\beta} | \hat{m}_{L\nu} | e_{i\alpha} \rangle$ can become not zero. By the first order perturbation of \mathcal{H}_{SO} , the eigenstate $|e_{i\alpha}^0\rangle$ of $\mathcal{H}_{\text{el-el}} + \mathcal{H}_{\text{CEF}}$ is modified as⁴

$$|e_{n\alpha}^0\rangle \rightarrow |e_{n\alpha}\rangle = |e_{n\alpha}^0\rangle + \sum_{m \neq n} \sum_{\beta} \frac{\langle e_{m,\beta}^0 | \mathcal{H}_{\text{SO}} | e_{n,\alpha}^0 \rangle}{\Delta_n^0 - \Delta_m^0} |e_{m,\beta}^0\rangle. \quad (3.15)$$

Here, Δ_n^0 and Δ_m^0 are unperturbed eigenenergies for $|e_{n\alpha}^0\rangle$ and $|e_{m\beta}^0\rangle$, respectively. Substituting Eq. (3.15) for $|e_n\rangle$ in Eq. (3.6) and $\hat{\mathbf{m}}_L$ for $\hat{\mathbf{m}}$, we obtain

$$\alpha_{E1-M1}^n = \sum_m \alpha_{E1-M1}^{nm}, \quad (3.16)$$

where

$$\begin{aligned} \alpha_{E1-M1}^{nm} \propto & \sum_{m,\alpha\beta} \frac{2\Delta_n^0 \hbar \omega \delta_n}{(\Delta_n^0)^2 - \hbar^2 \omega^2} \frac{1}{\Delta_n^0 - \Delta_m^0} \{ \text{Re}(\langle e_0^0 | \hat{p}_x | e_{m,\beta}^0 \rangle \langle e_{m,\beta}^0 | \mathcal{H}_{\text{SO}} | e_{n,\alpha}^0 \rangle \langle e_{n,\alpha}^0 | \hat{m}_y | e_0^0 \rangle) \\ & - \text{Re}(\langle e_0^0 | \hat{p}_y | e_{m,\beta}^0 \rangle \langle e_{m,\beta}^0 | \mathcal{H}_{\text{SO}} | e_{n,\alpha}^0 \rangle \langle e_{n,\alpha}^0 | \hat{m}_x | e_0^0 \rangle) \\ & + \text{Re}(\langle e_0^0 | \hat{p}_x | e_{n,\alpha}^0 \rangle \langle e_{n,\alpha}^0 | \mathcal{H}_{\text{SO}} | e_{m,\beta}^0 \rangle \langle e_{m,\beta}^0 | \hat{m}_y | e_0^0 \rangle) \\ & - \text{Re}(\langle e_0^0 | \hat{p}_y | e_{n,\alpha}^0 \rangle \langle e_{n,\alpha}^0 | \mathcal{H}_{\text{SO}} | e_{m,\beta}^0 \rangle \langle e_{m,\beta}^0 | \hat{m}_x | e_0^0 \rangle) \}. \end{aligned} \quad (3.17)$$

In the calculation of α_{E1-M1}^{nm} , $|e_0^0\rangle$ is substituted for $|g\rangle$ and $\text{Re}[\langle e_0^0 | \hat{p}_\mu | e_{i\alpha}^0 \rangle \langle e_{i\alpha}^0 | \hat{m}_{L\nu} | e_0^0 \rangle]$ is used. From Eq. (3.17), α_{E1-M1}^{nm} satisfies

$$\delta_n \alpha_{E1-M1}^{nm} \left(\omega = \frac{\Delta_n^0}{\hbar} \right) = -\delta_m \alpha_{E1-M1}^{mn} \left(\omega = \frac{\Delta_m^0}{\hbar} \right). \quad (3.18)$$

The contribution α_{E1-M1}^{nm} (α_{E1-M1}^{mn}) appears in α_{E1-M1}^n (α_{E1-M1}^m) which describes the contribution to MCHD from the transition to n - (m -) th excited state. MCHD originating from the

³As long as we focus on a single MnO_6 cluster, the site symmetry at the Mn^{2+} site is determined by the configuration of surrounding six oxygens and not affected by other octahedrons.

⁴The normalization factor is neglected for simplicity.

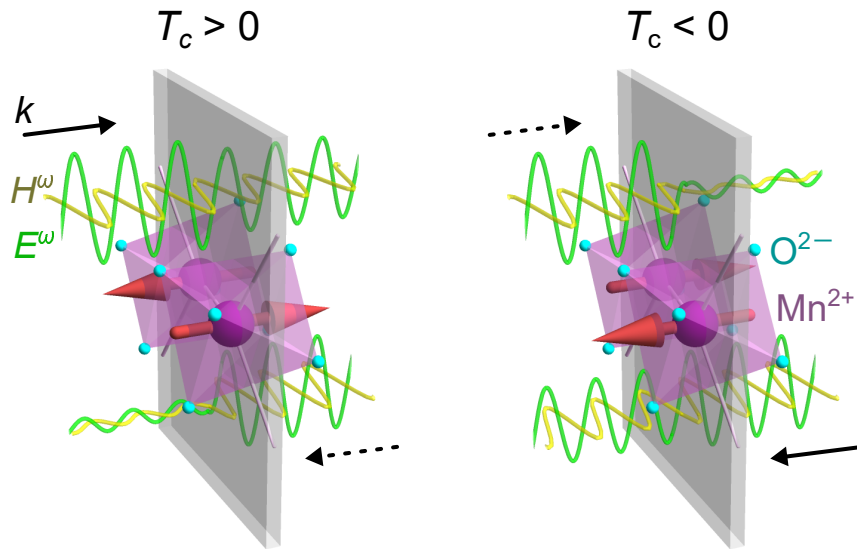


Figure 3.14: Schematic illustration of MCHD in MnTiO_3 for two distinct antiferromagnetic states $L_c > 0$ and $L_c < 0$. Red arrows denote magnetic moments. The sign of order parameter $L_c = [\mathbf{M}_A - \mathbf{M}_B]_c$ is in one-to-one correspondence with that of T_c .

transition to $|e_n\rangle$ and $|e_m\rangle$ should be almost entirely opposite in sign when the MCHD is predominantly described using the three levels $|g\rangle$, $|e_{n\alpha}\rangle$, and $|e_{m\beta}\rangle$. In Figs. 3.9(a) and (b), MCHD of opposite sign to that at 2.15 eV is seen above 2.3 eV. The reversal of sign in MCHD at 2.15 eV and above 2.3 eV indicates that the hybridization by \mathcal{H}_{SO} between ${}^4T_{1g}$ and ${}^4T_{2g}$ states of O_h is key to describe observed MCHD in MnTiO_3 .

3.4 Summary

In this chapter, we have investigated the MCHD in a collinear antiferromagnet MnTiO_3 . MCHD in MnTiO_3 is observed as the difference in the absorption coefficient between two configurations $\mathbf{k} \uparrow \uparrow \mathbf{T}$ and $\mathbf{k} \uparrow \downarrow \mathbf{T}$, following the verification of the in-plane off-diagonal ME couplings. Observed MCHD is a spontaneous effect arising in the absence of external electric and magnetic fields. Exploiting MCHD and the controllability of the toroidal moment \mathbf{T} , we have achieved binary switching of the absorption intensity. The origin of MCHD is staggered ordering of magnetic moments in phase with that of chirality of MnO_6 octahedrons in honeycomb antiferromagnetic structure.

Chapter 4

Magneto-chiral Imaging of Antiferromagnetic Domain in MnTiO_3

The knowledge of patterns and dynamics of magnetic domain structures is of great importance for manipulation of magnetic properties of materials. Several kinds of techniques have been and are being developed for observation of antiferromagnetic domain structures concurrently with the discovery and implementation of functionalities of antiferromagnetic materials. Due to the absence of magnetization, observation of antiferromagnetic domain structures is rather difficult than that of ferromagnetic ones, which is made possible by magneto-optical effects with which we can probe the direction and orientation of spontaneous magnetization. Novel \mathcal{T} -odd optical effects of antiferromagnetic origin should enable us to visualize spatial distribution of direction of staggered magnetization, even in the absence of magnetization.

Here, we demonstrate MCHD-based imaging of antiferromagnetic domain patterns in MnTiO_3 . Antiferromagnetic domain structures are clearly visualized exploiting the asymmetry in absorption coefficients between two distinct antiferromagnetic states with staggered magnetization in opposite directions. The MCHD-based imaging technique is featured with light-polarization independence and the absence of multiphoton optical processes, both of which lead to the reduced exposure time compared with that required in previously reported techniques.

In Sec. 4.1, we introduce two categories of antiferromagnetic domains and present pros and cons of several established imaging techniques of these domain structures. In Sec. 4.2, we demonstrate the MCHD-based imaging technique and report several features of antiferromagnetic domains in MnTiO_3 . The findings are summarized in Sec. 4.3.

4.1 Introduction to antiferromagnetic domain imaging

4.1.1 Orientational and antiphase domains

Two distinct regions are in different antiferromagnetic domains when magnetic order parameters take different values in two regions. In the most general form, magnetic order parameters \mathbf{O} are

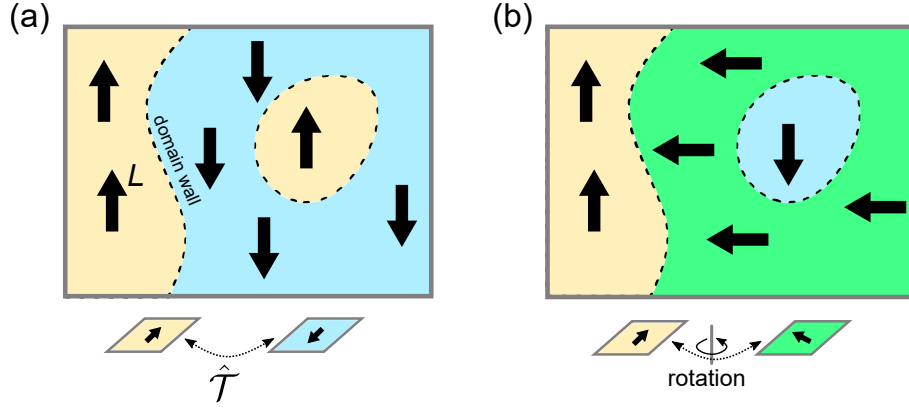


Figure 4.1: Schematic illustrations of the (a) antiphase and (b) orientational domains and domain walls (dashed lines). Black arrows denote staggered magnetization \mathbf{L} . By antiphase (orientational) domains, we denote two different domains separated by the antiphase (orientational) domain walls. Time-reversal and rotation operations which relates distinct domains are depicted in (a) and (b).

written as

$$\mathbf{O} = \sum_{\alpha} \sum_{\mathbf{r}} \mathbf{m}(\mathbf{r}) e^{i\mathbf{q}_{\alpha} \cdot \mathbf{r}}, \quad (4.1)$$

using the magnetic propagation vector \mathbf{q}_{α} and magnetic moments \mathbf{m} as a function of the position \mathbf{r} . For collinear commensurate antiferromagnets with magnetic unit cells containing N magnetic atoms, it is convenient to use staggered magnetization, or the Néel vector,

$$\mathbf{L} = \sum_{\alpha=1}^N c_{\alpha} \mathbf{m}(\mathbf{r}_{\alpha}), \quad (4.2)$$

as magnetic order parameters instead of \mathbf{O} . \mathbf{r}_{α} denotes the position of the α -th magnetic atoms in the magnetic unit cell. Here the coefficients c_{α} originate from $e^{i\mathbf{q}_{\alpha} \cdot \mathbf{r}}$ terms in Eq. (4.1).

Domain walls are $D - 1$ dimensional objects which separates two distinct domains in D dimensions [see Fig. 4.1]. In antiferromagnets where staggered magnetization \mathbf{L} is properly defined, there are two kinds of domain walls: antiphase and orientational domain walls. The antiphase domain wall separates two domains characterized by Néel vectors in opposite directions [see Fig. 4.1(a)]. Antiphase domain walls are seen in antiferromagnets with uniaxial magnetic anisotropy. The orientational domain wall separates two domains characterized by Néel vectors in different orientations [see Fig. 4.1(b)]. Orientational domain walls are seen in antiferromagnets with multiaxial or easy-plane magnetic anisotropy.¹

Antiphase and orientational domains are distinguished from the symmetry aspect. Antiphase domains are connected by the \mathcal{T} operation which inverts the direction of magnetic moments [see Fig. 4.1(a)]. Orientational domains are connected by the rotation operation which changes orientation of \mathbf{L} [see Fig. 4.1(b)]. We note that, as mentioned in Ch. 1, the \mathcal{T} operation is

¹Antiphase domain walls are seen in antiferromagnets with multiaxial or easy-plane magnetic anisotropy, too, while the orientational domain wall is not seen in uniaxial antiferromagnets.

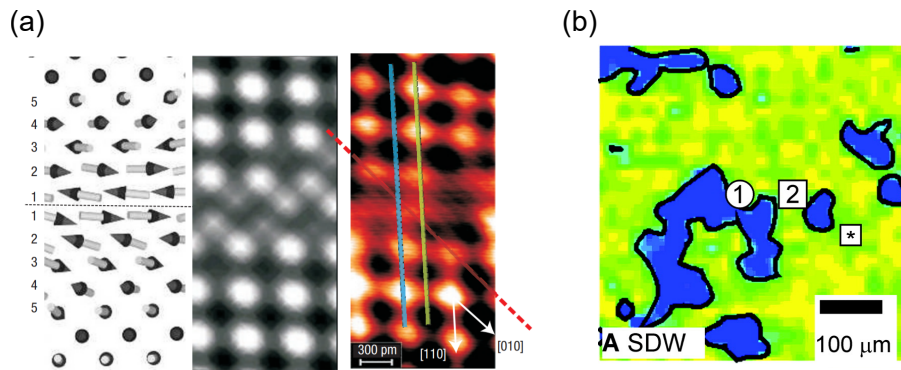


Figure 4.2: (a) (right) SP-STM image of the $[001]$ plane of Fe monolayer. (middle) Simulated SP-STM image for the spin texture shown in the left panel. Arrows in the left panel denote spins. (b) Maps of the intensity of the reflection at $(0,0,1 - \delta)$ in antiferromagnetic chromium at 130 K. (a) and (b) are taken from Refs. [68] and [71], respectively.

equivalent with a certain translational operation in collinear antiferromagnets with the magnetic unit cell larger than the crystallographic unit cell [see Fig. 1.3(a)]. Antiferromagnets where the \mathcal{T} operation is not equivalent to any translational operation are suitable for the implementation to magnetic storage because $\mathbf{L} = +\mathbf{l}$ and $\mathbf{L} = -\mathbf{l}$ states can be distinguished by bulk properties.

4.1.2 Antiferromagnetic-domain imaging techniques

Scanning imaging techniques

With respect to the size of the probed area in a single measurement, we classify magnetic-domain imaging techniques into two categories: scanning imaging techniques and optical imaging techniques. Scanning imaging techniques are featured by the probed area in a single measurement much smaller than a area of the single magnetic domain. The best spatial resolution among all the imaging techniques is achieved in scanning imaging techniques using nanometric tips as probes, at the expense of temporal resolution and the bulk sensitivity. As shown in Fig. 4.2(a), with the spin-polarized scanning tunneling microscopy (SP-STM), spin textures on the outermost surface of a sample are visualized with atomic resolution [68]. The middle panel of Fig. 4.2(a) shows a simulated SP-STM image of the spin texture depicted in the left panel. The image should look brighter (darker) if spins direct this (the other) side of the paper. The obtained SP-STM image of an antiferromagnetic Fe monolayer on W is in great agreement with the simulated image [see Fig. 4.2(a)]. Antiphase domains and a domain wall is clearly captured. The microscopic technique probes individual moments $\mathbf{m}(\mathbf{r})$ in Eqs. (4.1) and (4.2) and in principle applicable to distinguish all kinds of magnetic domains. For antiferromagnetic insulators to which STM techniques are not applicable, other microscopic techniques including the magnetoelectric force microscopy and the NV center magnetometry have been developed [69, 70].

Scanning imaging experiments are also performed at synchrotron facilities by using focused

x-ray beams as a probe [71, 72]. In x-ray microscopy imaging, different from imaging experiments with visible electromagnetic waves, spatial inhomogeneity in detected signals in a single measurement provides us information in reciprocal space, which is not accessible in other kinds of imaging experiments. In 2003, Evans *et al.* demonstrated scanning x-ray microdiffraction imaging of body-centered chromium. Below the Néel temperature 311 K, chromium adopts spin-density-wave (SDW-) type antiferromagnetic ordering characterized by the magnetic propagation vector $(0,0,1-\delta)$, with δ of around 0.05. With decreasing temperature from 311 K, orientation of spin \mathbf{S} changes at $T_{\text{SF}} = 123$ K from $\mathbf{S} \perp \mathbf{q}$ to $\mathbf{S} \parallel \mathbf{q}$ [73]. Figure 4.2(b) shows the image obtained at 130 K. In Fig. 4.2(b), blue (yellow) regions are featured with higher (lower) intensity of the reflection at $(0,0,1-\delta)$. Blue regions are interpreted as antiferromagnetic domains with $\mathbf{q} \parallel [001]$ and $\mathbf{S} \perp \mathbf{q}$ and yellow ones are characterized with other orientations of \mathbf{q} or \mathbf{S} .

Optical imaging techniques

By optical imaging techniques, areas large enough to cover several magnetic domains are probed in a single exposure. Usually, better temporal resolution is achieved with optical imaging techniques than that in scanning imaging techniques. The optical effects which we employ in imaging of a specific domain is determined based on the broken symmetry at the onset of the domain formation.



Figure 4.3: (a) Orientational antiferromagnetic domain pattern in NiO visualized by LB-based imaging. (b) SHG image of a antiphase domain pattern in Cr₂O₃. Sample size is 6×3 mm². (c) NLD image of an antiphase domain pattern in Pb(TiO)Cu₄(PO₄)₄. (a), (b), and (c) are taken from Refs. [74], [75], and [76], respectively.

Magnetic linear birefringence (LB) and dichroism (LD) are utilized to visualize orientational domain patterns. A certain rotational symmetries around the axis perpendicular to \mathbf{L} is broken in domains on both sides of an orientational domain wall. The lack of C_n ($n \geq 3$) rotational symmetry along the z direction results in the anisotropy in the dielectric tensor as $\chi_{xx}^e(\omega) \neq \chi_{yy}^e(\omega)$. Such anisotropy gives rise to LD and LB. Magnetic contributions to LD and LB shows up as the difference in the complex refractive index Δn as

$$\Delta n = n_{\parallel} - n_{\perp}, \quad (4.3)$$

where n_{\parallel} (n_{\perp}) represents the refractive index when magnetic moments are parallel (perpendicular) to the polarization of light. The difference in n enables us to detect the orientation, not the direction, of \mathbf{L} . In 1960, Roth performed magnetic-LB based imaging of orientational domains of cubic NiO. NiO is a collinear antiferromagnet with multiaxial magnetic anisotropy. The obtained domain pattern in NiO is shown in Fig. 4.3(a). The stripe-like domain pattern is clearly visualized exploiting the optical phase retardation depending on the relative orientation between \mathbf{L} and the polarization of light.

Optical imaging of antiphase domain patterns is rather difficult compared with that of orientational domain patterns. When two antiferromagnetic states are connected to each other by a translational operation, the domain pattern is nearly indistinguishable. Even when the \mathcal{T} symmetry is broken in the magnetic point group which describes symmetry of the magnetic texture, optical imaging of antiferromagnetic antiphase domain patterns is not straightforward because MCD, which is activated by the lack of the \mathcal{T} symmetry and exploited to visualize ferromagnetic domains, is absent in antiferromagnets with zero magnetization due to the \mathcal{PT} or two-fold symmetry.

In ME antiferromagnets, the \mathcal{P} symmetry, not only the \mathcal{T} symmetry, is broken at the onset of the formation of antiphase domains. The second harmonic generation (SHG) signal is significantly influenced by breaking of the \mathcal{P} symmetry. SHG is a nonlinear optical process where the frequency doubled light with photon energy $2\hbar\omega$ is generated in response to the incident light beam with $\hbar\omega$. In materials where the \mathcal{P} symmetry is broken, electric-dipole (ED) contribution to the SHG signal arises in addition to the magnetic-dipole (MD) contribution, latter of which is always symmetry-allowed. In 1995, Fiebig *et al.* demonstrated the first optical imaging of the antiphase domain pattern in a linear ME antiferromagnet Cr_2O_3 exploiting SHG. For circularly polarized light with intensity I_{σ} propagating along the c axis of Cr_2O_3 below T_N , intensity of the SHG signal I_{SHG} is given as

$$I_{\text{SHG}} \propto I_{\sigma}^2 (|\chi_{\text{MD}}|^2 + |\chi_{\text{ED}}|^2 - \Delta), \quad (4.4)$$

where

$$\Delta = 2 [\text{Re}(\chi_{\text{MD}})\text{Im}(\chi_{\text{ED}}) - \text{Im}(\chi_{\text{MD}})\text{Re}(\chi_{\text{ED}})]. \quad (4.5)$$

Here χ_{ED} (χ_{MD}) denote complex susceptibilities of ED- (MD-) SHG [77]. Since χ_{ED} is odd and χ_{MD} is even under the \mathcal{P} operation, the sign of Δ in Eq. (4.5) is different for antiphase domains connected by the \mathcal{P} operation. The remaining terms in Eq. (4.4) which are quadratic in χ_{ED} and χ_{MD} is always positive. Figure 4.3(b) shows the obtained domain pattern in Cr_2O_3 . The antiferromagnetic domain pattern clearly shows up as the spatial inhomogeneity in the SHG signal. After this demonstration of SHG-based imaging in Cr_2O_3 , SHG has been employed to visualize domains in numerous ME antiferromagnets where the formation of the antiphase domain accompanies \mathcal{P} -symmetry breaking [49, 61, 78, 79, 80] and become established as a

major technique to visualize antiphase domains in ME antiferromagnets. However, the nonlinear optical process requires the long-time irradiation of the light beam with a high photon density, which often poses problems of temporal resolution worse than a few minutes and heating of specimens.

Utilizing linear optical ME coupling arising from the simultaneous breaking of the \mathcal{P} and \mathcal{T} symmetries is a promising way of imaging antiphase domains in ME antiferromagnets with reducing the exposure time compared with SHG-based imaging. In 2020, Kimura *et al.* demonstrated optical imaging of antiphase domains in an ME antiferromagnet Pb(TiO)Cu₄(PO₄)₄ using the magnetic-quadrupole induced nonreciprocal linear dichroism (NLD) [76]. Pb(TiO)Cu₄(PO₄)₄ is a noncoplanar antiferromagnet with the nonzero $q_{a^2-b^2}$ -type magnetic quadrupole²[81]. Two antiferromagnetic states on both sides of antiphase domain walls are featured with the different signs of $q_{a^2}(= -q_{b^2})$ [see Eq. (1.9)]. NLD is the directional dichroism of linearly polarized light, where absorption intensity for the polarized light depends on the sign of the magnetic quadrupole moment. The NLD signal is odd under \mathcal{P} and \mathcal{T} operations. Figure 4.3(c) shows the obtained image in Pb(TiO)Cu₄(PO₄)₄. The antiphase domain pattern is clearly seen as the spatial inhomogeneity of transmitted light intensity. In this NLD-based imaging, exposure time of less than 0.5 s is achieved.

MCHD is another linear optical effect with which we can visualize antiphase domain patterns in ME antiferromagnets. MCHD-based imaging technique has not been developed because materials where spontaneous MCHD is observed has been limited to ferromagnets where magnetic domain patterns are easily visualized with MCD-based imaging. Since MCHD is the optical rectification effect caused by the toroidal moment \mathbf{T} , the spatial distribution of \mathbf{T} should be visualized in MCHD-based imaging. Antiphase magnetic domains are in one-to-one correspondence with the ferrotoroidic domains in several collinear ME antiferromagnets. MCHD-based imaging, which is applicable to antiferromagnets where the toroidal moment is not zero, regardless the presence of the quadrupole moments, would be a complementary technique to NLD-based ones.

²In Pb(TiO)Cu₄(PO₄)₄, we denote 180° domain by antiphase domains.

4.2 Results and discussion

Demonstration of MCHD-based domain imaging

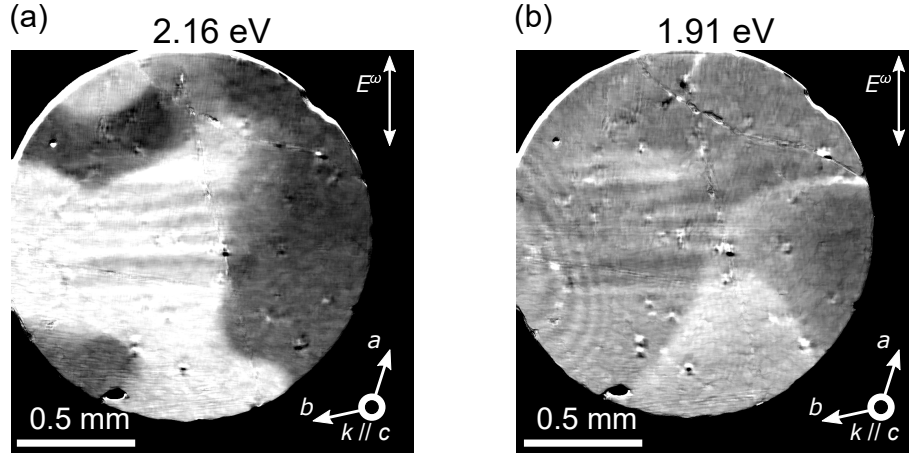


Figure 4.4: Difference images at 60.0 K for incident light with (a) $\hbar\omega = 2.16$ eV and (b) $\hbar\omega = 1.91$ eV. Images at 65.0 K are used as the reference. E^ω denotes the polarization of incident light. The exposure time is 2 s for (a) and 0.25 s for (b).

Figures 4.4(a) and (b) show difference images of a MnTiO_3 crystal at 60.0 K ($< T_N = 65$ K) without gold electrodes. Before recording the images, the sample was cooled down from 120 K to 3 K. To realize the multidomain state, we applied no electric and magnetic fields during the cooling process. Both images were recorded at 60 K in a subsequent warming run in the absence of electric and magnetic fields. Figures 4.4(a) and (b) were recorded in the different warming run. The rate of temperature change at 65 K in the cooling runs was 5-6 K/min and that at 60 K in the warming runs was 0.6 K/min. In Fig. 4.4(a), a pronounced domain pattern is observed in the circular field of view. The incident photon energy of $\hbar\omega = 2.16$ eV lies at the peak of the MCHD spectra [see Fig. 3.11]. Figure 4.4(b) is a difference image recorded with $\hbar\omega = 1.91$ eV, at which energy MCHD is absent. Only the interference fringes and the shutter of the camera is seen in Fig. 4.4(b).

Using original images recorded in the same warming run as Fig. 4.4(a), we investigated the temperature dependence of the difference of transmitted light intensity per pixel between brighter and darker regions. We chose square-shaped regions labeled A and B [see Fig. 4.5(a)] as the representatives of brighter and darker areas in the difference image taken with $\hbar\omega$ of 2.16 eV, respectively. I_X ($X = A, B$) is computed as

$$I_X = \int_X d\mathbf{r} I(\mathbf{r}) / \int_X d\mathbf{r}, \quad (4.6)$$

using transmitted light intensity I as a function of the pixel position \mathbf{r} . $\int_X d\mathbf{r}$ denotes the integral over a region labeled X . The temperature dependence of $\Delta I_{AB}/I_{AB} = (I_A - I_B)/(I_A + I_B)$ is shown in Fig. 4.5(a). The value of $\Delta I_{AB}/I_{AB}$ of -1.8% in the paramagnetic phase above 65 K is

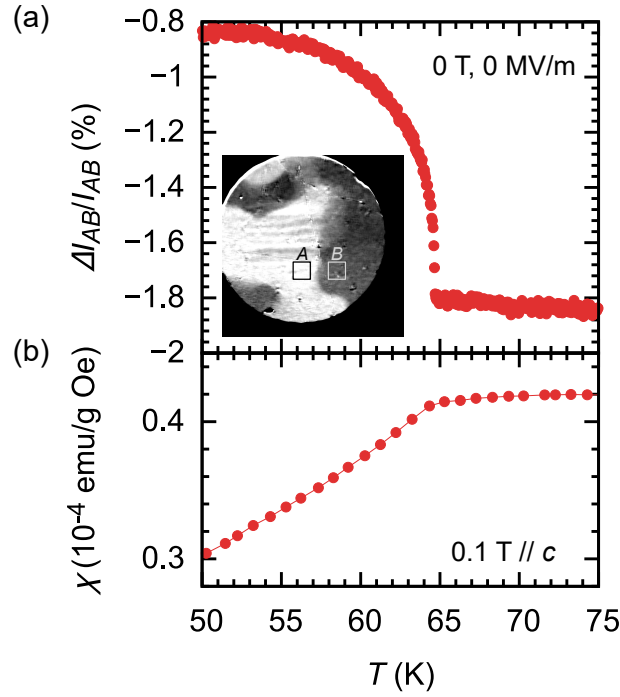


Figure 4.5: (a) Temperature dependence of $\Delta I_{AB}/I_{AB}$ for $\hbar\omega = 2.16$ eV in the absence of electric and magnetic fields. Inset shows the position and size of square-shaped brighter A region and darker B region in the difference image at 60 K. (b) Temperature dependence of the magnetic susceptibility χ along the c axis.

attributable to the contribution from the spatially inhomogeneous distribution of incident light. In addition to this nonmagnetic contribution, the magnetic contribution is seen in $\Delta I_{AB}/I_{AB}$ below T_N ; antiferromagnetic ordering at 65 K, which is characterized by the anomaly in the temperature dependence of the magnetic susceptibility χ in Fig. 4.5(b), accompanies the rise in $\Delta I_{AB}/I_{AB}$. The positive magnetic contribution in $\Delta I_{AB}/I_{AB}$ below T_N accounts for why A region is brighter than B region in the difference image at 60 K despite the $\Delta I_{AB}/I_{AB}$ is negative.

The difference in brightness between A and B regions is accountable to the difference in the absorption coefficients of antiferromagnetic origin. The magnetically induced change in $\Delta I_{AB}/I_{AB}$ at 55 K is as large as 1%. Incorporating the inhomogeneous distribution of light, I_A and I_B is expressed as $I_0(1 - \epsilon)e^{-\alpha_A d}$ and $I_0(1 + \epsilon)e^{-\alpha_B d}$, respectively. $I_0(1 - \epsilon)$ and $I_0(1 + \epsilon)$ denote incident light intensity for A and B regions, respectively. α_X ($X = A, B$) denotes the absorption coefficients for the region labeled X . $\Delta I_{AB}/I_{AB}$ becomes

$$\begin{aligned} \frac{\Delta I_{AB}}{I_{AB}} &= \frac{I_0(1 - \epsilon)e^{-\alpha_A d} - I_0(1 + \epsilon)e^{-\alpha_B d}}{I_0(1 - \epsilon)e^{-\alpha_A d} + I_0(1 + \epsilon)e^{-\alpha_B d}} \\ &\sim -\epsilon - \frac{(\alpha_A - \alpha_B)d}{2}. \end{aligned} \quad (4.7)$$

The second term $-(\alpha_A - \alpha_B)d/2$ represents the difference in absorption coefficients originating from the difference in antiferromagnetic order parameters between two regions, while the nonmagnetic contribution of -1.8% is represented by the temperature-invariant first term $-\epsilon$. Using

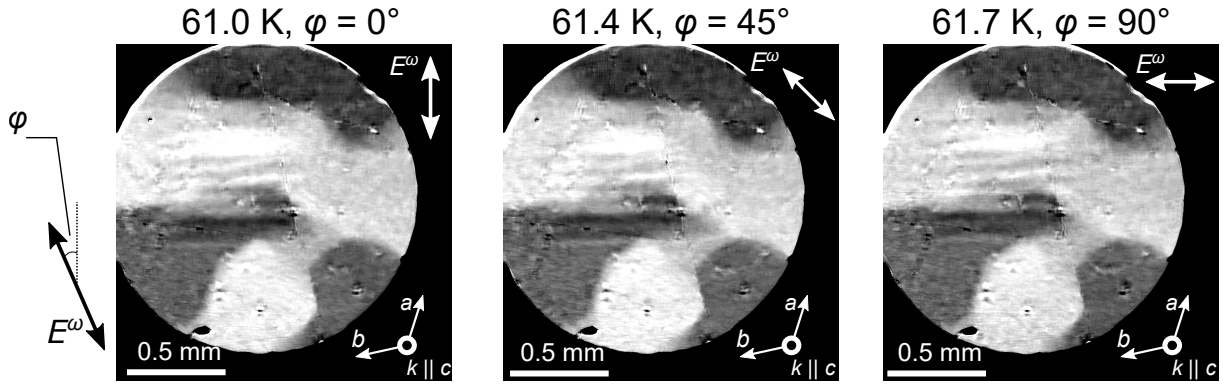


Figure 4.6: Light-polarization-direction dependence of difference image. Images at 65.0 K ($\varphi = 0^\circ$), 65.4 K ($\varphi = 45^\circ$), and 65.7 K ($\varphi = 90^\circ$) are used as references, respectively.

the sample thickness of $d = 150 \mu\text{m}$, $-(\alpha_A - \alpha_B)d/2$ of 1% at 55 K corresponds to $(\alpha_B - \alpha_A)/2$ of 0.67 cm^{-1} , which is comparable to α_{--} of 0.56 cm^{-1} at 55 K for $\hbar\omega = 2.16 \text{ eV}$ derived in Ch. 3. The approximation in Eq. (4.7) is valid since ϵ and $(\alpha_A - \alpha_B)d/2$ is far smaller than one. Judging from Fig. 4.5(a), the magnetic contribution $(\alpha_A - \alpha_B)d/2$ is saturated at 50 K as decreasing temperature from T_N , as the magnitude of the MCHD signal does in Fig. 3.10(b).

Since MCHD is the directional dichroism of unpolarized light, obtained pattern by imaging technique based on MCHD should not depend on the direction of polarization of incident light. Figure 4.6 shows difference images recorded with linearly polarized incident light for several polarization directions φ . All the images were recorded in series in an identical warming run, which was a different run from that of Figs. 4.4(a) and (b). Temperature profile is the same as that of Figs. 4.4(a) and (b). We obtained the same pattern for all the polarization direction, which is in contrast with the cases for the imaging technique based on LB and NLD.

From above examination of several images obtained with varying photon energy, temperature, and the polarization direction of incident light, we conclude that domain patterns in difference images in Fig. 4.4(a) and Fig. 4.6 below T_N map the spatial distribution of α_{--} in Eq. (3.1). Since the propagation vector \mathbf{k} of incident light is fixed along the c axis in the present imaging experiment, the spatial distribution of α_{--} reflects the c -component T^c of the toroidal moment, i.e. the ferrotoroidic domain pattern, over the sample. Brighter and darker regions in difference images are in $T^c > 0$ and $T^c < 0$ states. Considering the coupling between \mathbf{L} and \mathbf{T} in MnTiO_3 [see Eq. (3.10)], observed ferrotoroidic domain pattern is nothing but the antiferromagnetic domain pattern.

Structural and thermal properties of domain patterns

Observed patterns represent the projection along the c axis of the original domain distribution in three dimensions because the present MCHD-based domain imaging is performed in transmission geometry. Judging from the estimated value of $(\alpha_A - \alpha_B)/2$, domain walls seem to be oriented perpendicular to the c plane of the crystal. Let us assume that $\alpha_{++} = a$ and $\alpha_{--} = b$ ($-b$)

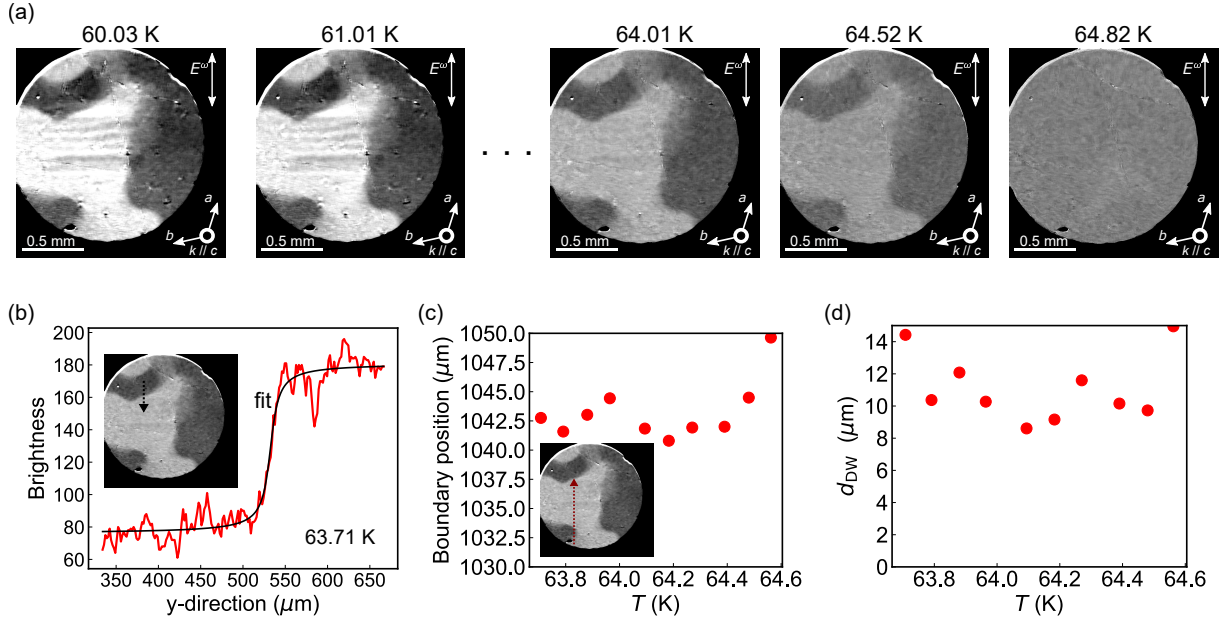


Figure 4.7: (a) Difference images at several temperatures. Images at 65.0 K is used as reference. All the images are recorded in the same warming run as Fig. 4.4(a) and Fig. 4.5(a). (b) Line intensity profile in the difference image at 63.71 K along the path denoted by a dotted arrow in the inset. (c)-(d) Temperature dependence of the domain-boundary (c) position and (d) thickness. In the inset of (c), the definition of the boundary position is illustrated by red arrows.

for $T^c > 0$ ($T^c < 0$) states. When the X ($X = A, B$) region in the inset of Fig. 4.5(a) is the $r_X : 1 - r_X$ mixture of $T^c > 0$ and $T^c < 0$ states, α_X becomes

$$\alpha_X = a + (2r_X - 1)b. \quad (4.8)$$

By substituting Eq. (4.8), $(\alpha_A - \alpha_B)/2$ becomes $(r_A - r_B)b$. Observed $(\alpha_A - \alpha_B)/2$ of over 100% of the value of α_{--} at 55 K indicates that r_A and r_B are nearly equal to one and zero, respectively.

The typical size of the antiferromagnetic domains in MnTiO₃ is of 0.1-1 mm in width [see Fig. 4.4(a) and Fig. 4.6], which is similar to those in bulk samples of several kinds of collinear antiferromagnet such as Cr₂O₃ and LiCoPO₄ [61, 75]. The three-fold symmetry is unrecognizable in the antiferromagnetic domain pattern of MnTiO₃, in spite of the trigonal symmetry of the underlying crystallographic lattice. The absence of the trigonal symmetry in magnetic domain patterns indicates that the strength of the exchange interaction in c plane is so isotropic that orientation of domain walls is not bounded as long as it lies parallel to the c axis.

Antiferromagnetic domain patterns are erased by warming up the sample above T_N . As for the shape and positions of domain boundaries, there is no similarity between the two images recorded in the different warming runs [see Fig. 4.4(a) and Fig. 4.6]. While the similar domain patterns are reported to repeatedly arise even after erasing pattern in ME antiferromagnets such as Cr₂O₃ [75] and Pb(TiO)Cu₄(PO₄)₄ [76], such memory effects in domain formation is absent in MnTiO₃.

The domain structure is stable up to just below T_N . Temperature dependence of domain patterns near the critical temperature is shown in Fig. 4.7(a). The obtained difference images become less contrasted with approaching T_N , reflecting the temperature dependence of the magnitude of the MCHD signal. Domain patterns seem invariant under the change of temperature from 60 K to 64.5 K. We examine the line profiles of difference images for qualitative discussion. Figure 4.7(b) shows the line profile along the path highlighted in the inset which intersects the domain boundary. To extract the position and the width of the domain boundary, the line profile is fit by the relation

$$I_{\text{path}}(y) = A \arctan\left(\frac{y - y_{\text{DW}}}{d_{\text{DW}}}\right) + c. \quad (4.9)$$

Here, $I_{\text{path}}(y)$ represents brightness of the difference image at the position y along the path. A , y_{DW} , d_{DW} , and c are fitting constants. y_{DW} and d_{DW} denote the position and the thickness of the domain boundary, respectively. Figures 4.7(c) and (d) show the temperature dependence of the domain-boundary position and the thickness, respectively. To cope with the thermal shift in the sample position, the positions of boundary are measured from the edge of the sample [see the inset of Fig. 4.7(c)]. No systematic change is observed in Fig. 4.7(c), which qualitatively evidences the thermal stability of domain patterns. From Fig. 4.7(d), the change in the domain-wall thickness larger than $10 \mu\text{m}$ is not observed. We note that thickness of magnetic domain walls is typically smaller than a micro meter [82] which is smaller than the spatial resolution of the present imaging experiments.

4.3 Summary

In this chapter, we have demonstrated the antiferromagnetic domain imaging technique based on MCHD. Antiphase domains in antiferromagnetic MnTiO_3 are clearly visualized exploiting the asymmetry in absorption coefficients between two antiferromagnetic states with $L_c > 0$ and $L_c < 0$. The present imaging technique do not require polarized light and is performed with exposure time of at most 2 s. Observed submillimeter-sized domain patterns are not constrained by the trigonal symmetry of the crystal. Shape and position of the domain boundary are found to persist up to just below T_N and completely erased by warming up the sample above T_N .

Chapter 5

Imaging Study of Magnetoelectric Domain Reversal

Switching between two metastable antiferromagnetic states is achieved by external-field-driven displacement of boundary which spatially separates two different antiferromagnetic domains. Dynamic properties of domain walls such as velocity and mobility are key factors which determine switching speed. Since domain walls are a kind of defects which occupy far smaller volume than domains themselves do, their behavior can hardly be tracked by measurements of the macroscopic physical properties. Direct observation of the temporal evolution of domain patterns is one of the most powerful techniques to investigate the role of domain walls in the switching process.

Here, we investigate domain-wall dynamics in the ME antiferromagnet MnTiO_3 by means of MCHD-based imaging of the domain patterns in transient states. Millisecond dynamics of the domain patterns in the abruptly switched electric fields is clearly captured exploiting the memory effect in the switching process. Based on the velocity-force relationships of domain walls obtained at several temperatures, the temperature dependence of domain-wall mobility and the pinning field are found to be responsible for the enhancement of switching speed near the critical temperature.

In Sec. 5.1, recent studies about switching dynamics in ME antiferromagnets are introduced based on the previous researches in other ferroic materials. In Sec. 5.2, the imaging study of the domain switching process in MnTiO_3 is presented. Following the observation of quasistatic and millisecond dynamics of the domain patterns, domain-wall dynamics is focused on. Results and discussion are summarized in Sec. 5.3.

5.1 Introduction to switching dynamics in ferroic materials

5.1.1 Temporal evolution of switched areas

In ferroic materials characterized by a order parameter X , two states with $X > 0$ and $X < 0$ are switched by reversal of the conjugate field Y which satisfies $X = -\frac{\partial \mathcal{F}}{\partial Y}$. The $X > 0$ state is energetically favored in $Y > 0$ and the $X < 0$ state is favored in $Y < 0$. (X, Y) is (M, H) for

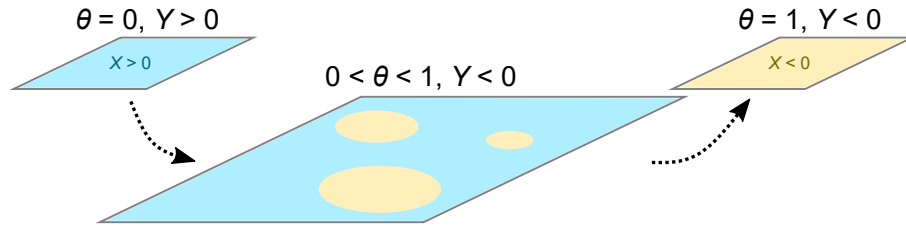


Figure 5.1: Illustration of the transient state in the switching process. Initial and reversed domain is blue and brown colored, respectively.

ferromagnets and (P, E) for ferroelectric materials. As mentioned in Ch. 1, (X, Y) is $(\gamma_{ij}, E_i H_j)$ for linear ME antiferromagnets where the antiferromagnetic order parameter is switched by the simultaneous application of electric and magnetic fields.

The switching process from the $X > 0$ state to the $X < 0$ state is composed of the nucleation of the $X < 0$ domain followed by the expansion of the nucleated domain achieved by the domain-wall displacement. Even when the external field is abruptly switched from $Y > 0$ to $Y < 0$, it takes some time for the switching process to be accomplished. The faster manipulation of the ferroic order parameter is achieved by the reduction in the switching time. In this subsection, we first show how several factors including domain-wall velocity are employed to theoretically describe the temporal evolution of the volume fraction of switched domains and then introduce several corresponding experimental studies.

Theory

By $\theta(t)$, we denote the fraction of the $X < 0$ domain at time t after the external field is abruptly switched from $Y > 0$ to $Y < 0$ at $t = 0$ [see Fig. 5.1]. $\theta(0) = 0$ and $\theta(\infty) = 1$. In 1962, Fatuzzo presented a theoretical framework where $\theta(t)$ was calculated from the nucleation rate and the initial radius of domains and the domain-wall velocity [83]. While the formulation in Ref. [83] was done to describe the temporal evolution of $\theta(t)$ in ferroelectric materials, the theory is valid for other kinds of ferroic materials.

The areas $A_-(t)$ of the $X < 0$ domain at time t is computed as

$$A_-(t) = \int_0^t ds S(t-s) \left. \frac{dN}{dt} \right|_{t=s}, \quad (5.1)$$

using the number of $X < 0$ domains $N(t)$. $S(t)$ denotes an area of a $X < 0$ domain at time t after its nucleation. Assuming that the nucleation of domains is a random statistical process [84] which happens with the probability R , we set $N(t)$ to obey the following equation;

$$\frac{dN}{dt} = R(N_0 - N) \Leftrightarrow N(t) = N_0 (1 - e^{-Rt}). \quad (5.2)$$

Here, N_0 denotes the number of all possible nucleation sites. Once we suppose domains to be circular, the area $S(t)$ is computed as $S(t) = \pi r(t)^2$, using the radius $r(t)$ of the domain. Using

the domain-wall velocity v_{DW} , $r(t)$ is written as

$$r(t) = r_0 + v_{\text{DW}}t, \quad (5.3)$$

where r_0 denotes the initial radius of the domain just after the nucleation.

To obtain the fraction $\theta(t)$, the overlap among switched domains, which is neglected in the derivation of Eq. (5.1), must be taken into account. Based on the discussion in Ref. [85], it is pointed out [83] that the relation between θ and A_- becomes

$$\theta = 1 - \exp \left[- \left(A_- - \frac{\pi r_0^2 N(t)}{S_{\text{all}}} + \frac{\pi r_0^2 N_0 R t}{S_{\text{all}}} \right) \right]. \quad (5.4)$$

S_{all} denotes the area of the sample. By substituting Eqs. (5.1)-(5.3) for Eq. (5.4), θ is computed as

$$\theta(\tau) = 1 - \exp \left[-2k^2 \left\{ 1 - \left(\tau + \frac{1}{k} \right) + \frac{1}{2} \left(\tau + \frac{1}{k} \right)^2 - e^{-\tau} \left(1 - \frac{1}{k} \right) + \frac{1}{2k^2} (1 - \tau) \right\} \right], \quad (5.5)$$

using dimensionless parameters $k = v_{\text{DW}}/Rr_0$ and $\tau = Rt$ ¹.

According to the above formulation, the form of $\theta(\tau)$ is determined by the single parameter k which is proportional to the domain-wall velocity v_{DW} . By the definition of k , the switching process predominantly described by the domain-wall motion corresponds to $k \gg 1$ and that described by the nucleation of the numerous domains corresponds to smaller values of k . We note that it is difficult to experimentally obtain the parameter k for the switching process with $k \gg 1$ because $\theta(\tau)$ curves do not vary so much for the change of k .

Experiments

Equation (5.5) successfully explains the temporal evolution of the switched areas observed in ferroic materials. Figure 5.2(a) shows the time dependence of the magnetization reversal process of two ferromagnets where the switching processes are governed by the different mechanisms. In ferromagnets, the temporal evolution of θ is investigated by time-resolved measurements of magnetization. The switching process in a GdFe sample was well described by θ with $k \sim 2000$ and that in a TbCo sample was described with $k \sim 0$ [86]. Magnetic domain patterns visualized exploiting the magneto-optical Kerr effect [see the inset of Fig. 5.2(a)] clearly evidence that the switching process in the GdFe with larger k is driven by the domain-wall motion and that in the TbCo is described by the nucleation of numerous domains. The validity of Eq. (5.5) was also confirmed in ferroelectric materials by time-resolved measurements of displacement currents [83].

So far, several studies have shown that the electric-field induced switching of the cycloidal magnetic textures typically takes more than a millisecond [79, 87, 88, 89]. In 2011, Hoffmann *et al.* visualized the transient state in the switching process of the cycloidal ME antiferromagnet

¹In the derivation of Eq. (5.5), S_{all} is equated to $N_0 \pi r_0^2$.

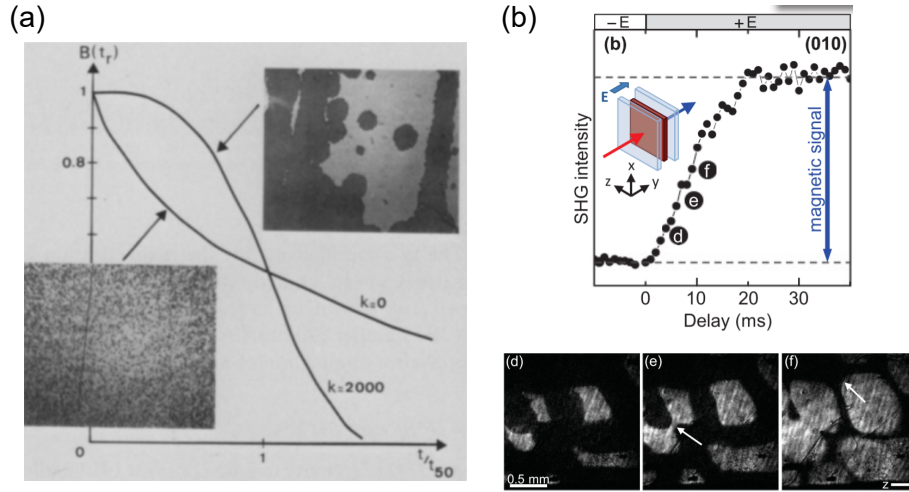


Figure 5.2: (a) Time dependence of the magnetization process of a GdFe sample ($k \sim 2000$) and a TbCo sample ($k \sim 0$). B in the vertical axis stands for the volume fraction of the original domain. t_{50} in the horizontal axis is defined so that $B(t_{50})$ to be 0.5. Magnetic domain patterns in the transient state is shown in the inset. (b) SHG-based imaging of the switching process in MnWO_4 at 11.8 K ($< T_N = 12$ K). (a) and (b) are taken from Refs. [86] and [79], respectively.

MnWO_4 [79]. MnWO_4 is a cycloidal antiferromagnet where the \mathcal{P} symmetry is broken at the onset of magnetic ordering and the helicity of the magnetic texture is in one-to-one correspondence with the direction of electric polarization [90]. In MnWO_4 , the helicity of the cycloidal magnetic structure is switched by reversal of the electric field [91]. Judging from the helimagnetic domain patterns visualized by the SHG-based imaging technique, the switching process in MnWO_4 is described by the domain-wall displacement [see Fig. 5.2(b)]. In MnWO_4 the reduction of the switching time near the Néel temperature and that in larger driving electric fields is reported [79, 51]. The similar temperature and external-field dependence of the switching time is also observed in other cycloidal ME magnets by the study of $\theta(t)$ tracked by time-resolved polarized neutron diffraction experiments [88, 89]. However, the origin of the reduction in the switching time in those ME antiferromagnets remains a matter of the speculation due to the lack of the visualization of the transient states.

5.1.2 Domain-wall velocity in driving fields

Theory in pure crystal

Driving force for a domain wall is proportional to the energy gap between two states separated by the boundary. When the two regions with $X = \eta > 0$ and $X = -\eta < 0$ are separated by the domain wall at $x = l$ as depicted in Fig. 5.3, the total energy of the system in the conjugate field Y becomes $E = \eta Y L_y L_z (L_x - 2l)$. The driving force f_{DW} on the domain wall per unit area is computed from the gradient of E as

$$f_{\text{DW}} = -\frac{1}{L_y L_z} \frac{\partial E}{\partial l} = 2\eta Y. \quad (5.6)$$

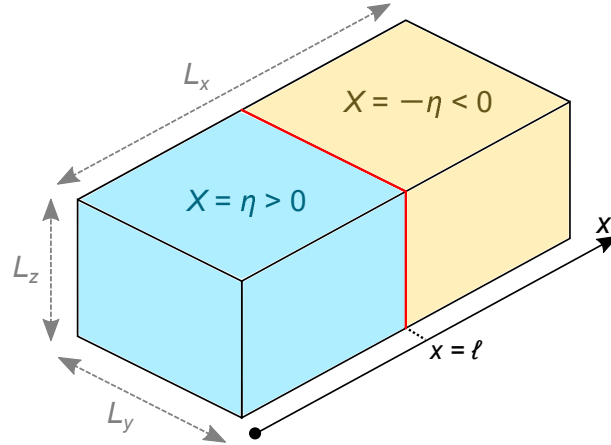


Figure 5.3: Illustration of the two domains with $X = \eta > 0$ and $X = -\eta < 0$ separated by the domain wall at $x = l$. Domain wall is depicted by a red line. $L_y L_z$ is an area of the domain wall.

The equation of motion is necessary to calculate domain-wall velocity v_{DW} from the driving force on the wall. In the following, based on the discussion in Ref. [92], we show how v_{DW} is computed for linear ME antiferromagnets. The Lagrangian density $\mathcal{L}_{\text{spin}}$ for antiferromagnets with easy-axis anisotropy is written as [93]

$$\mathcal{L}_{\text{spin}} = \frac{1}{2} (\rho |\dot{\mathbf{n}}|^2 - A |\nabla \mathbf{n}|^2 - \mathcal{K}_{zz} n_z^2), \quad (5.7)$$

where ρ , A , and \mathcal{K}_{zz} denote the mass, the exchange interaction, and the magnetic anisotropy, respectively². Here, the unit vector $\mathbf{n}(\mathbf{r}, t) = (\sin \theta \cos \phi, \sin \theta \sin \phi, \cos \theta)$ represents the direction of the Néel vector at position \mathbf{r} . Domain-wall profile in Fig. 5.3 is represented by θ and ϕ set as

$$\begin{cases} \cos \theta(x, t) = \tanh \frac{x-l(t)}{\lambda_{\text{DW}}} \\ \phi = \phi(t) \end{cases}. \quad (5.8)$$

λ_{DW} in Eq. (5.8) denotes the thickness of the domain wall placed at $x = l$. By substituting Eq. (5.8) for Eq. (5.7), we obtain the Lagrangian L_{spin} as

$$L_{\text{spin}} = \int_{-\infty}^{\infty} dx \mathcal{L}(x, t) = \frac{\rho \dot{l}^2}{\lambda_{\text{DW}}} + \rho \dot{\phi}^2 \lambda_{\text{DW}} + \text{const.} \quad (5.9)$$

As in Ref. [92], we deal with the longitudinal ME effect where electric polarization along the z axis is induced in proportion to the magnetic field along the z axis. The domain wall at $x = l$ separates two regions with $\gamma_{zz} > 0$ and $\gamma_{zz} < 0$. The potential energy V of the domain wall originating from the ME term in the free energy \mathcal{F}_{ME} [see Eq. (1.6)] is $V = 2\gamma_{zz} E_z H_z l + \text{const.}$ Using L_{spin} and V , the equation of motion of the domain wall becomes

$$\frac{2\rho}{\lambda_{\text{DW}}} \ddot{l} = -\frac{4\alpha_0 \mathcal{J}}{\lambda_{\text{DW}}} \dot{l} + 2\alpha_{\parallel} E_z H_z. \quad (5.10)$$

²In Eq. (5.7), Zeeman coupling between applied magnetic fields and electric-field induced magnetization is neglected for simplicity. This approximation is valid for the small electric field where the effect of precession of \mathbf{n} on v_{DW} is absent.

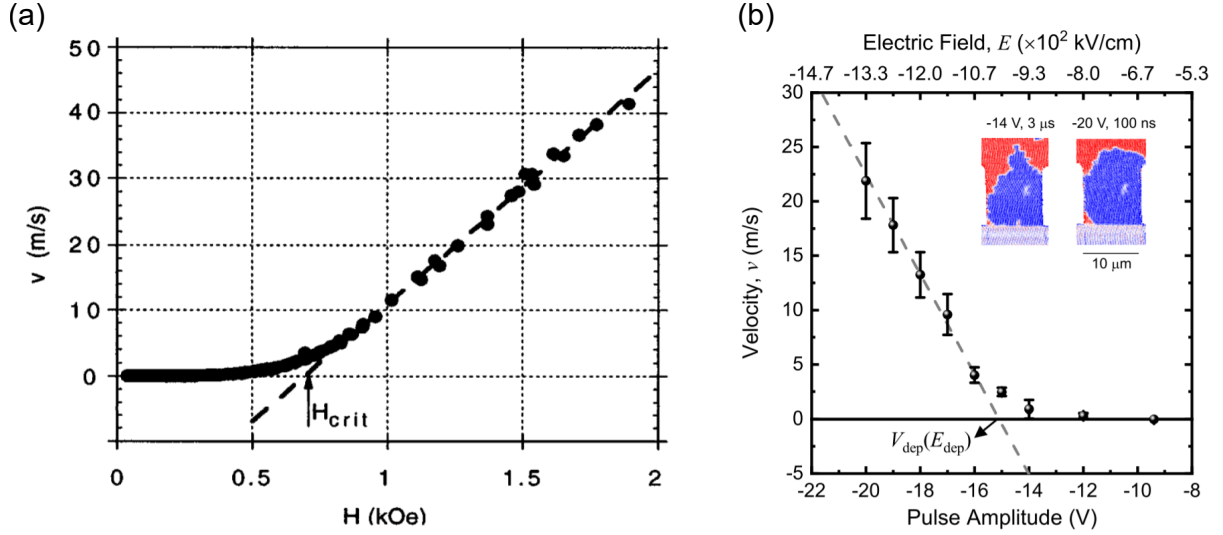


Figure 5.4: Domain-wall velocity as a function of (a) the applied magnetic field in ferromagnetic Co film and (b) as a function of the applied pulsed electric field in Cr_2O_3 . In (b), electric fields were applied in the magnetic field of $\mu_0 H_c = 4$ T and at 285 K. (a) and (b) are taken from Refs. [94] and [95], respectively.

Here the friction term $\frac{4\alpha_0\mathcal{J}}{\lambda_{\text{DW}}}\dot{l}$ originates from the viscous drag represented as

$$R = \alpha_0\mathcal{J} \int_{-\infty}^{\infty} dx |\dot{\mathbf{n}}|^2 = 2\alpha_0\mathcal{J} \left(\frac{\dot{l}^2}{\lambda_{\text{DW}}} + \dot{\phi}^2 \lambda_{\text{DW}} \right), \quad (5.11)$$

where α_0 and \mathcal{J} stand for the Gilbert damping factor and the angular momentum per unit cell, respectively. By substituting $\ddot{l} = 0$ for Eq. (5.10), we obtain the domain-wall velocity v_{DW} in the steady state as

$$v_{\text{DW}} = \frac{\gamma_{zz} H_z \lambda_{\text{DW}}}{2\alpha_0 \mathcal{J}} E_z. \quad (5.12)$$

Velocity-force relationships in disordered materials

In contrast to Eq. (5.12), the domain-wall velocity in ferroic materials is usually not linear in the driving force on the domain wall. The nonlinearity arises from the pinning force acting on the domain wall. Figure 5.4(a) shows the magnetic-field dependence of v_{DW} in a ferromagnetic Co film. As pointed out in Ref. [96], there are two regimes in the domain-wall motion in response to the applied field: creep motion and the viscous flow of the domain wall. The domain-wall creep is thermally activated motion of the domain wall for the external fields below the pinning threshold. Creep motion of the domain wall was first clearly observed in Ref. [94], where the domain-wall velocity v_{DW} in creep regime is fitted to the relation

$$v_{\text{DW}} \propto \exp \left[-\frac{U_c}{k_B T} \left(\frac{H_p}{H} \right)^\nu \right], \quad (5.13)$$

where k_B , U_c , and H_p denote the Boltzmann constant, the pinning potential, and the pinning threshold. The exponent ν is related with the dimensionality of the order parameter and of

the system. For applied fields larger than the pinning threshold, the viscous flow, or sliding motion, of the domain wall occurs. Viscous flow of the domain wall is characterized by the linear relationship between the domain-wall velocity and the applied field. For ferromagnetic domain walls driven by the magnetic field, the $v_{\text{DW}}-H$ relationship is expressed as [97]

$$v_{\text{DW}} = v_0 + \mu(H - H_p), \quad (5.14)$$

using v_0 and μ which denote the contribution from the creep motion and the domain-wall mobility, respectively.

Despite the fact that dynamic properties of domain walls cannot be understood without the investigation of the velocity-force relationship, the applied-field dependence of v_{DW} in ME antiferromagnets has rarely been studied. Figure 5.4(b) shows the electric-field dependence of v_{DW} in a linear ME antiferromagnet Cr_2O_3 measured in electric and magnetic fields both along the c axis. In the experiment [95], pulsed electric fields were applied in the magnetic field to displace the antiferromagnetic domain wall in Cr_2O_3 . v_{DW} was computed using two images recorded before and after the application of the pulsed electric field. In Fig. 5.4(b), the nonlinear relationship between v_{DW} and the applied field, which is similar to that in ferromagnetic film [see Fig. 5.4(a)], is clearly observed.

5.2 Results and discussion

5.2.1 Quasistatic domain reversal

The quasistatic switching process of antiferromagnetic states in MnTiO_3 at 64.0 K under electric and magnetic fields along the c axis is shown in Fig. 5.5. Before measurements, the sample was cooled down from 70 K ($> T_N = 65$ K) to 64.0 K in the absence of external fields to realize the multidomain state. At 64.0 K, a magnetic field of $\mu_0 H_c = 0.1$ T was applied and then the electric field was ramped up from $E_c = 0$ MV/m to 7.9 MV/m at the rate of smaller than 0.05 MV/s. After the initial sweep, E_c was swept between ± 7.9 MV/m for two cycles. The transmitted light intensity averaged over the whole image $I = \int d\mathbf{r} I(\mathbf{r}) / \int d\mathbf{r}$ is shown in Fig. 5.5(a). $\int d\mathbf{r}$ denotes the integral over a whole image. For the cyclic reversal of the electric field in the magnetic field, transmitted light intensity I shows hysteresis loops with a temporal drift. Judging from the $I-E_c$ curve in Fig. 5.5(a), the darker (brighter) antiferromagnetic state with the larger (smaller) absorption coefficient is favored in $E_c H_c > 0$ ($E_c H_c < 0$).

The quasistatic switching process at the verge of the coercive fields for the first loop of E_c is shown in Figs. 5.5(b) and 5.5(c). In Fig. 5.5(b), a darker monodomain state is realized at $E_c = -3.8$ MV/m. At $E_c = -3.9$ MV/m, the brighter domain nucleates around a crack of the sample. The brighter region expands by decreasing E_c to -4.0 MV/m, clearly evidencing an electric-and-magnetic-fields-driven motion of the antiferromagnetic domain wall in MnTiO_3 . From Fig. 5.5(b), the quasistatic domain reversal process in MnTiO_3 is composed of the nu-

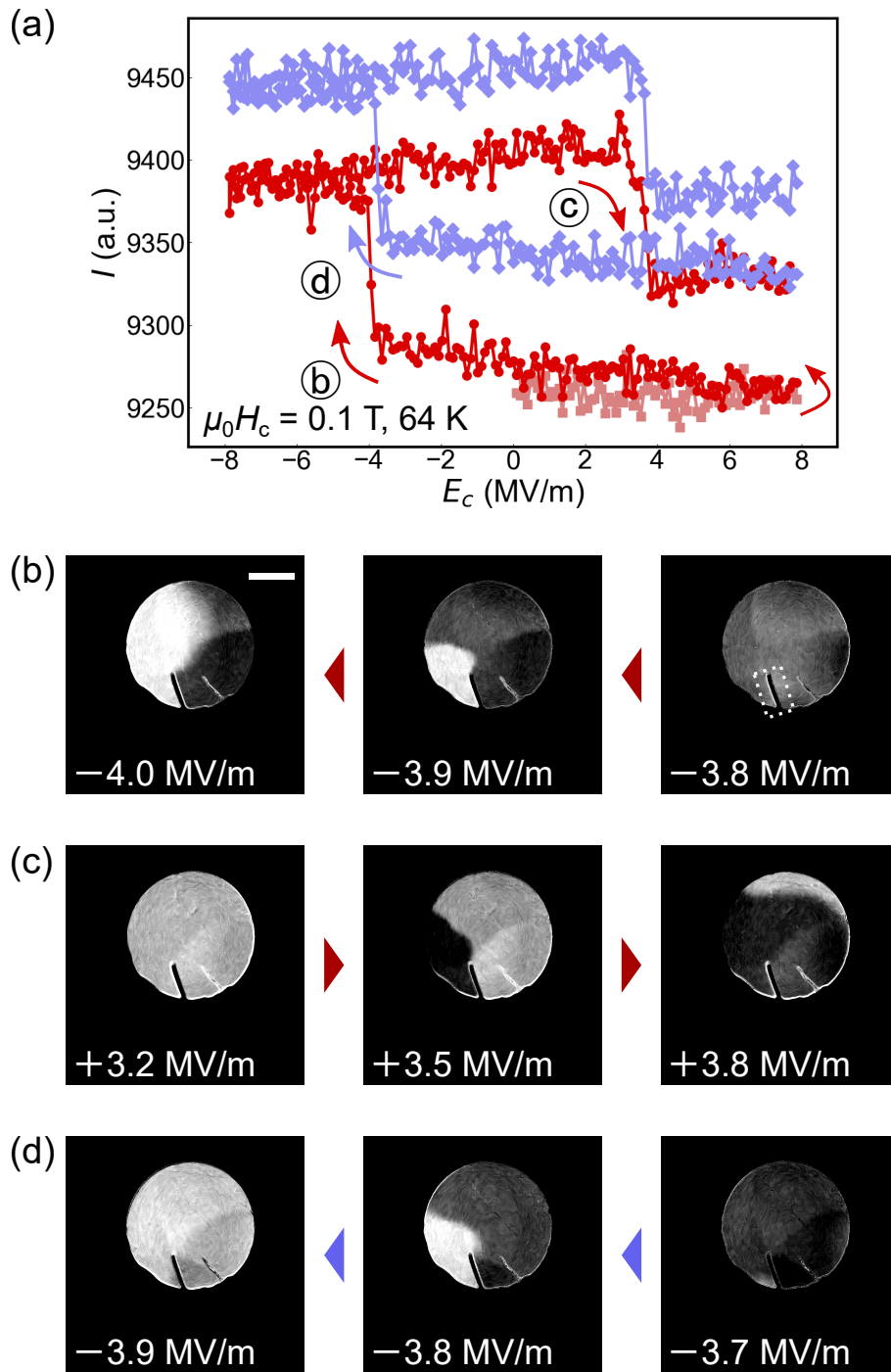


Figure 5.5: (a) Change in the averaged transmitted light intensity I with sweeping the electric field along the c axis in the magnetic field of $\mu_0 H_c = 0.1$ T at 64.0 K. Values of I in the initial sweep, the first loop, and the second loop of E_c are plotted with light-red, deep-red, and light-blue dots, respectively. (b-d) Difference c -plane images recorded at each electric field. Images at $E_c = -7.9$ MV/m in the first loop, $E_c = 7.9$ MV/m at the end of the first loop, and $E_c = -7.9$ MV/m in the second loop are used as the reference for (b), (c), and (d), respectively. The white scale bar in the left panel of (b) corresponds to 0.5 mm. Panels in (b), (c), and (d) were recorded during the first decrease, the second increase, and the second decrease in E_c . In the right panel of (b), a crack of the sample is highlighted by a dotted box.

cleation of the submillimeter-sized domain followed by the displacement of the domain wall as in several other linear ME antiferromagnets [61, 76] and not of the nucleation of the numerous domains nor the coherent rotation of magnetic moments. The switching process is similar for an E_c -increasing run. In Fig. 5.5(c), a brighter monodomain state realized at 3.2 MV/m becomes a multidomain state at 3.5 MV/m and the darker region expands by increasing E_c from 3.5 MV/m to 3.8 MV/m. Comparing Figs. 5.5(b) and 5.5(c), the switching processes in the E_c -increase and the E_c -decrease runs are slightly asymmetric; while the coercive electric field is around 4.0 MV/m for both cases, switching in the E_c -increasing run is not as steep as that in the E_c -decreasing run where a monodomain state persists up to -3.8 MV/m. Furthermore, propagation directions of the domain wall are different while the nucleation occurs at the position of the crack in both cases.

Figure 5.5(d) shows the switching process in the second loop of E_c . The transient state in the second loop of E_c is similar to that in the first loop, indicating a certain memory effect in this isothermal quasistatic switching process. The multidomain state realized at -3.8 MV/m in Fig. 5.5(d) is similar to that realized at -3.9 MV/m in the first loop in Fig. 5.5(b). The striking similarity in the domain patterns in transient states indicates the presence of the energetically favored pathway for the moving domain wall in the switching process in $E_c H_c > 0$. Such memory effect is often regarded as the consequence of the pinning effect [79].

The coexistence of several magnetic multipoles all activated by the simple collinear antiferromagnetic structure is advantageous for the present imaging study of the domain-switching dynamics in MnTiO_3 . As discussed earlier, antiferromagnetic domains are made visible by the magnetoelectric optical effect related with the \mathcal{P} -odd magnetic multipoles. Visible multipoles which interact with a transverse electromagnetic wave do not inherently couple to the DC electric and magnetic fields parallel to the propagation vector \mathbf{k} of light. For the imaging study of the field-driven motion of antiferromagnetic domains, thin plates of antiferromagnets where staggered magnetization \mathbf{L} is controllable with $\mathbf{E} \parallel \mathbf{k}$ is suitable for applying a high electric field without the compensation of a large field of view. In MnTiO_3 , antiferromagnetic domains are visualized with incident light with $\mathbf{k} \parallel \mathbf{c}$ exploiting the relation between \mathbf{L} and the toroidal moment \mathbf{T} . In addition, antiferromagnetic domains in MnTiO_3 are manipulated by the electric and magnetic fields $\mathbf{E}, \mathbf{H} \parallel \mathbf{c}$ thanks to the relation between \mathbf{L} and the γ_{\parallel} , which is related with the magnetic monopole and the q_{z2} -type quadrupole. It is of note that MCHD-based imaging experiments in the same configuration is possible in antiferromagnets with several magnetic symmetries including tetragonal $\bar{4}'$ and $4/m'$ and hexagonal $\bar{6}'$ and $6/m'$, where the toroidal moment and the magnetic monopole and quadrupole coexists in the same way as in MnTiO_3 .

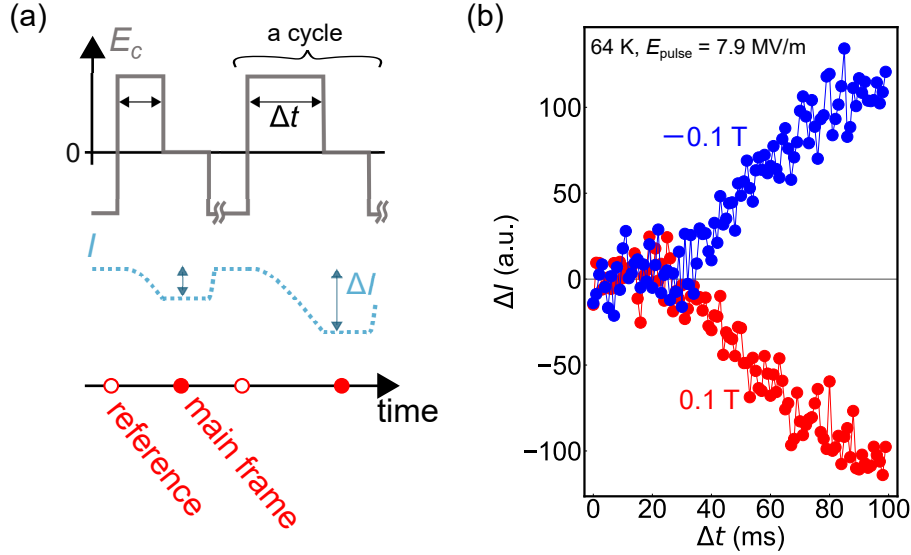


Figure 5.6: (a) Timing scheme of the repetitive imaging experiment. Reference images were recorded in every poling process. All the measurements were performed in the presence of the magnetic field along the c axis. In the positive magnetic field, the averaged transmitted light intensity (blue dotted line) takes the maximum after poling with the negative voltage and decreases by ΔI in response to the application of the positive pulsed electric field for Δt . (b) The change in the transmitted light intensity ΔI at 64 K as a function of Δt for $\mu_0 H_c = \pm 0.1$ T.

5.2.2 Dynamic domain reversal

Imaging of the millisecond dynamics

The deterministic nature in the domain reversal process enables the investigation of the dynamic switching process under the abrupt reversal of the external fields between $E_c H_c > 0$ and $E_c H_c < 0$ by repetitive imaging of domain patterns. A timing scheme of the experiment is shown in Fig. 5.6(a). All the measurements were performed in the magnetic field of $|\mu_0 H_c| = 0.1$ T. Each cycle of measurements consists of three parts: (i) First, a negative electric field of $E_{\text{pole}} = -7.9$ MV/m, which is large enough to switch antiferromagnetic states at 64.0 K [see Fig. 5.5(a)], was applied along the c axis for more than a second to realize the monodomain state. (ii) Second, a positive pulsed electric field of E_{pulse} was applied along the c axis for time Δt . The electric field was then turned off. (iii) Finally, the domain image was recorded at zero electric field. Since the driving force $f_{\text{DW}} = 2\gamma_{\parallel} E_c H_c$ for the domain wall is zero in the absence of the electric field, the domain pattern exactly at time Δt after abrupt switching of E_c from E_{pole} to E_{pulse} is recorded in the third step. The degree of the temporal evolution of the domain pattern before recording the image is controlled by changing Δt . The overall picture of the switching dynamics can be grasped by collecting images with varying Δt .

The change in the ratio between two antiferromagnetic domains caused by the application of the pulsed electric field appears as the difference between the averaged transmitted light intensity in the main frame I_{main} and that in the reference image I_{ref} . Figure 5.6(b) shows the pulse-width

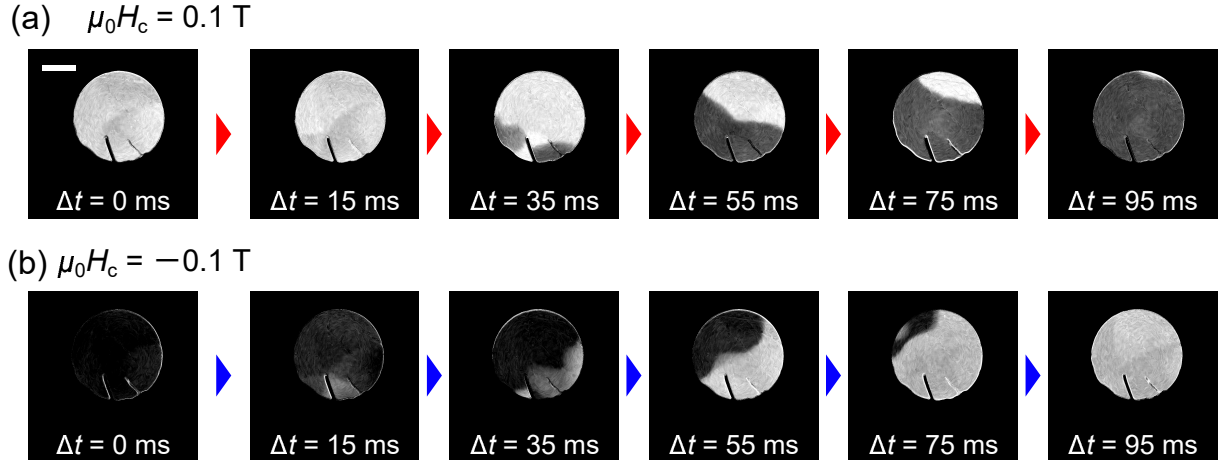


Figure 5.7: Difference images recorded at several values of Δt at 64.0 K for (a) $\mu_0 H_c = 0.1$ T and (b) -0.1 T. The white bar in (a) corresponds to 0.5 mm.

dependence of a change in the averaged transmitted light intensity $\Delta I = I_{\text{main}} - I_{\text{ref}}$ at 64.0 K for $E_{\text{pulse}} = 7.9$ MV/m. Under the magnetic field of $\mu_0 H_c = 0.1$ T, effects of application of the pulsed electric fields clearly appear in ΔI when the pulse width exceeds 30 ms. Under the positive magnetic field, the monodomain state of the brighter antiferromagnetic domain is favored in the negative electric field of $E_{\text{pole}} < 0$ [see Fig. 5.5]. The decrease in the transmitted light intensity suggests that the darker region arises in the field of view by the application of the electric field E_{pulse} for time Δt . The gradual drop in ΔI in $\mu_0 H_c = 0.1$ T for Δt of 30 ms $< \Delta t < 90$ ms indicates that the transient states is realized in the field of view, where the darker region expands in response to the application of the positive electric field. Judging from Fig. 5.5(a), the complete reversal of the antiferromagnetic domain should be characterized by $|\Delta I|$ of around 100. Such value of $|\Delta I|$ is achieved for Δt of more than 90 ms. The pulsed electric field with the pulse width shorter than 30 ms retains $\Delta I \sim 0$. Such inactiveness in the beginning of the switching process is indicative of the switching dynamics dominated by the domain wall displacement [83, 86]. The pulse-width dependence of ΔI is similar for $\mu_0 H_c = -0.1$ T except for the reversed sign of ΔI . The reversal of sign of ΔI between $\mu_0 H_c = 0.1$ T and -0.1 T is consistent with the picture that the antiferromagnetic domain is controlled by the product $E_c H_c$. The brighter (darker) antiferromagnetic state is energetically favored in negative (positive) $E_c H_c$. In the negative magnetic field, the darker monodomain state is realized in the negative poling electric field. The application of the positive pulsed electric field for time Δt gives rise to the brighter antiferromagnetic state when Δt is larger than 30 ms. Darker domain favored for $E_c H_c > 0$ is realized in the poled state for $\mu_0 H_c = -0.1$ T and brighter domain, which is realized in poled state for $\mu_0 H_c = 0.1$ T, is induced by pulsed electric field.

The transient states in the millisecond switching process are visualized in difference images at several values of Δt at 64 K in $|\mu_0 H_c| = 0.1$ T and $E_{\text{pulse}} = 7.9$ MV/m, as shown in Fig. 5.7. As pointed out in the analysis of ΔI - Δt curve in Fig. 5.6(b), for $\mu_0 H_c = 0.1$ T, the ratio

of the darker region in the field of view continuously increases by increasing Δt from 15 ms to 95 ms, while that of the brighter region increases by increasing Δt for $\mu_0 H_c = -0.1$ T. In both magnetic fields, the domain pattern continuously changes from a monodomain state to the other monodomain state. Note that the antiferromagnetic domain is poled back after every exposure. The continuous deformation in the domain pattern with varying Δt for each magnetic field indicates the existence of the memory effect in the dynamic switching process. The millisecond dynamics in the antiferromagnetic domain switching process driven by electric and magnetic fields in an ME antiferromagnet MnTiO_3 is clearly captured. The dynamic domain-switching process in the abruptly switched electric field is clearly described by the domain-wall displacement as in the quasistatic switching process. The submillimeter-sized domains observed in the transient state with Δt of 35, 55, and 75 ms is qualitatively similar in scale to those observed in the transient states of the quasistatic switching process and in multidomain state realized by zero-field cooling. The $\Delta I \sim 0$ region for $\Delta t < 30$ ms in Fig. 5.6(b) corresponds to the absence of the nucleation of the domain and the domain-wall motion for Δt of 0-15 ms in Fig. 5.7. In contrast to the case of the quasistatic switching process, the nucleation site in the field of view seems not confined at the position of a crack of the sample. The asymmetry in the switching process for $E_c H_c > 0$ and $E_c H_c < 0$ is seen in the different routes of propagating domain walls between Figs. 5.7(a) and (b); the domain wall propagates from left bottom to right top of the difference image in Fig. 5.7(a) and from right bottom to left top in Fig. 5.7(b). The almost complete monodomain state for $\Delta t = 95$ ms of Figs. 5.7(a) and (b) shows that monodomain ferrotoroidic state is realized by the application of electric and magnetic fields along the toroidal moment. Considering the coupling among the toroidal moment, the magnetic monopole and the ferroaxial degrees of freedom, we conclude that the sample is in a monodomain ferroaxial state³.

We investigate the dynamic switching process at different temperature and the pulse amplitude E_{pulse} . Figures 5.8(a) and (b) show the switching process at 63.75 K and 64.25 K, respectively. The reversal process at 63.75 K is slower than that at 64.25 K; while the complete switching of the antiferromagnetic state is achieved with the pulse width of $\Delta t = 80$ ms in Fig. 5.7(b), it takes more than 120 ms for the domain to be reversed in Fig. 5.7(a). The decrease in the strength of the pulsed electric field also slows down the reversal process [see Fig. 5.8(c) and Fig. 5.7(a)]. The slowing-down behaviors in smaller electric fields and at lower temperature is observed in the switching process in several multiferroics by the investigation of the temporal evolution of the volume fraction of the domain [87, 88, 89]. The switching processes at various conditions shown in Figs. 5.8(a)-(c) are accomplished by the domain-wall displacement. Furthermore, in all the conditions, domain walls propagates the similar routes: from bottom left to top right. Present imaging study, with which we can visualize the transient state, reveals that

³See the Appendix C for the details about the relation between the ME tensor components and the axial degree of freedom.

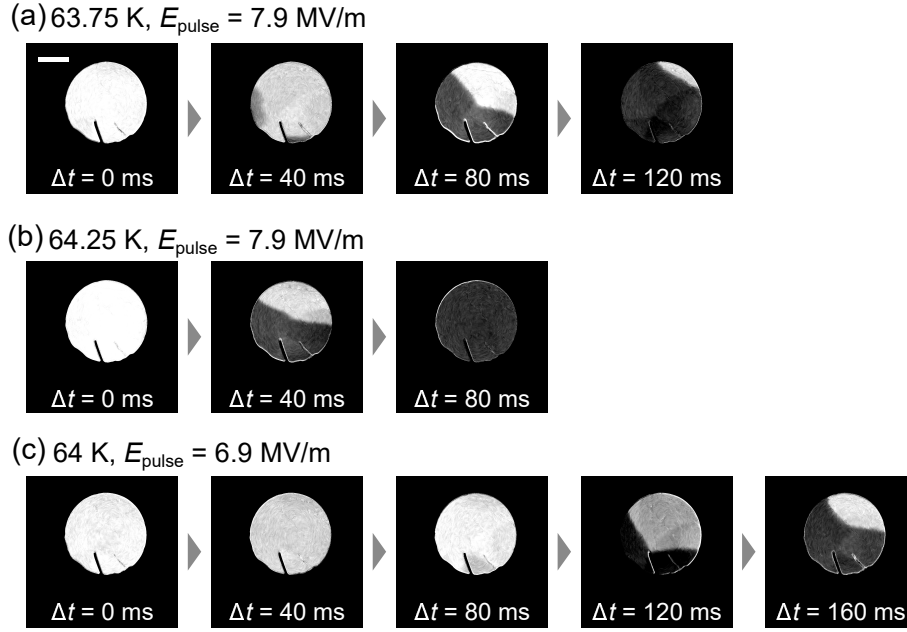


Figure 5.8: Difference images recorded at several values of Δt in the repetitive imaging experiment in $\mu_0 H_c = 0.1$ T. T and E_{pulse} is 63.75 K and 7.9 MV/m in (a), 64.25 K and 7.9 MV/m in (b), and 64.0 K and 6.9 MV/m in (c). The white bar in (a) corresponds to 0.5 mm.

the change in the switching speed of the antiferromagnetic domain reversal is attributable solely to the temperature and electric-field dependence of the domain-wall velocity, not to the change in the nucleation process and/or the route of the domain wall motion.

Dynamic properties of domain wall

To evaluate the domain wall velocity, we performed the different imaging experiment with a multidomain initial state where the domain wall is driven back and forth. Figure 5.9(a) shows timing scheme of this oscillating domain wall imaging in a fixed magnetic field of $\mu_0 H_c = 0.1$ T. Prior to the experiment, at 64.0 K, a negative electric field of $E_{\text{pole}} = -7.1$ MV/m was applied for poling and then a positive pulsed electric field with amplitude $E_{\text{DW}} = 5.7$ MV/m was applied for 400-450 ms to realize the initial multidomain state. Throughout the experiment, temperature was kept below T_N to retain the domain pattern. The domain-wall velocity v_{DW} was investigated as a function of a strength of the driving electric field $E_{\text{drive}} > 0$. For a given value of E_{drive} , two images were recorded at given temperature T to evaluate v_{DW} ; one after the application of the positive pulsed electric field with amplitude E_{pulse} for $t_{\text{pulse}} = 10$ ms, and the other after the application of the negative pulsed electric field with the same amplitude for the same duration [see Fig. 5.9(b)]. v_{DW} was simply estimated by dividing the shift in the position of domain walls between two images by t_{pulse} .

A nonlinear enhancement of v_{DW} in response to the increase of E_{drive} is observed. Figure 5.10(a) shows the E_{drive} dependence of the domain wall velocity v_{DW} at 64.0 K. In a fixed magnetic field, the driving force of the antiferromagnetic domain wall in MnTiO_3 is proportional

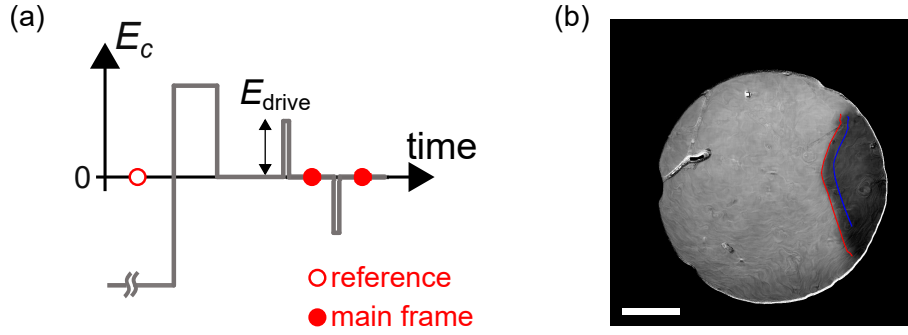


Figure 5.9: (a) Timing scheme of the oscillating domain wall imaging in a fixed magnetic field. Reference image was recorded in the poling process. (b) Difference image at 64.0 K recorded just after the application of E_{drive} of 7.1 MV/m for 10 ms at 64.0 K. The white bar corresponds to 0.5 mm. The domain-wall profile is shown by a red line. After the application of $-E_{\text{drive}}$ for 10 ms, the brighter region expands and the domain wall moves to the position denoted by a blue line.

to the electric field. The nonlinear velocity-force relationship is similar to those widely observed in other ferroic materials [94, 95]. From Fig. 5.10(b), the critical electric field E_p which separates the creep and the viscous flow regimes of the domain wall motion is roughly estimated to be around 5.5 MV/m. By fitting v_{DW} in the viscous regime to the phenomenological relationship $v_{\text{DW}} = \mu_E(E_{\text{drive}} - E_p) + v_0$ [see Eq. (5.14)], we obtain the electric-field based mobility μ_E . At 64.0 K, μ_E is estimated to be $4.56 \text{ m}^2/(\text{GV}\cdot\text{s})$ [see Fig. 5.10(a)].

Obtained domain wall velocity in the antiferromagnet MnTiO_3 is relatively small compared with that in other ferroic materials. For example, v_{DW} of 8.3 mm/s in $E_{\text{pulse}} = 7 \text{ MV/m}$ at 64.0 K in MnTiO_3 is five orders smaller than that of ferroelectric BaTiO_3 in the same electric field [98]. From Eq. (5.14), once we neglect the contribution from the creep motion, the difference in v_{DW} in the viscous regime should result from the difference in the mobility μ and the driving force f_{DW} for the domain wall. To compare the domain wall mobility of the different kinds of ferroics, we introduce the energy based mobility μ_Δ which represents the rate of the increase in v_{DW} in response to the increase in the energy gap between two states separated by the domain wall. μ_Δ in MnTiO_3 at 64.0 K is computed as $\mu_\Delta = \mu_E/(\gamma_{\parallel}\mu_0 H_c) = 4.7 \times 10^{-2} \text{ m}^4/\text{J}\cdot\text{s}$, which is comparable with μ_Δ of $10^{-3} \text{ m}^4/\text{J}\cdot\text{s}$ in BaTiO_3 . Hence, the relatively slow domain-wall dynamics in antiferromagnetic MnTiO_3 compared with that in ferroelectric BaTiO_3 is largely due to the tiny driving force even in the same electric field. Toward the faster domain wall motion, stronger E_c and H_c [95] as well as a reduction of the pinning energy at the verge of the spin-flip transition where the effective magnetic anisotropy becomes small [99] might be useful. In fact, v_{DW} of 20 m/s is achieved in the film of linear ME antiferromagnet Cr_2O_3 , where the μ_Δ is estimated to be around $5 \times 10^{-2} \text{ m}^4/\text{J}\cdot\text{s}$, in the electric and magnetic fields of 133 MV/m and 4 T, respectively [95].

The role of the strength of the magnetic field was investigated by the similar imaging experiments under several values of H_c . Figure 5.10(b) shows the $v_{\text{DW}}-E_c H_c$ relationship at 64.0 K.

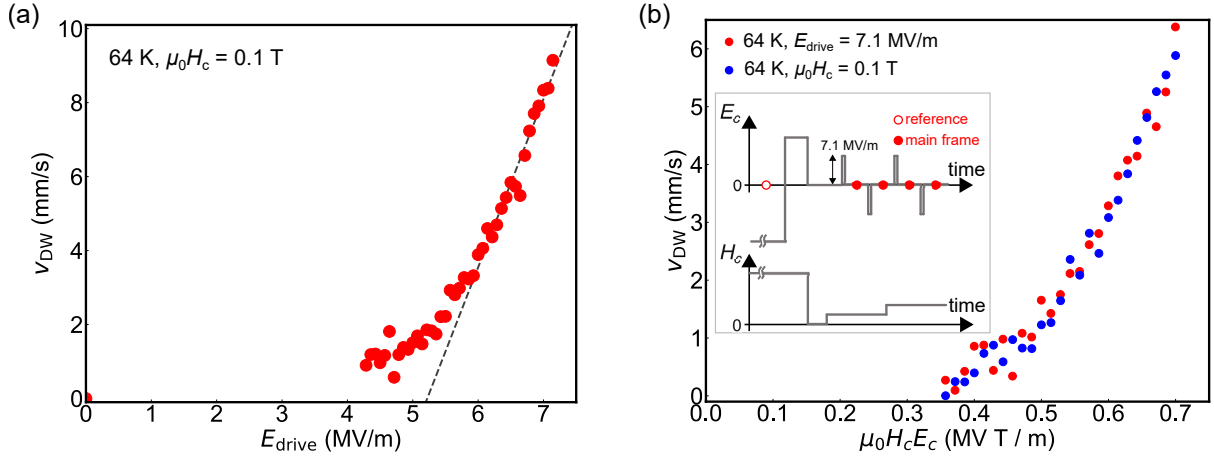


Figure 5.10: (a) E_{drive} dependence of v_{DW} at 64.0 K in $\mu_0 H_c = 0.1$ T. Dotted line shows the fitting curve $v_{\text{DW}} = \mu_E(E_{\text{drive}} - E_p) + v_0$. (b) $E_c H_c$ dependence of v_{DW} at 64.0 K obtained by two different ways. See the main text for the detail. The timing scheme for the oscillating domain wall imaging in various magnetic fields is depicted in the inset.

Blue dots were obtained by the same type of experiment as that performed to obtain Fig. 5.10(a). Red dots were obtained by the oscillating domain wall imaging experiment where E_{drive} is fixed and the magnetic field $\mu_0 H_c$ was varied [see the inset of Fig. 5.10(b)]. From the similarity between v_{DW} measured in two different ways, we conclude that the v_{DW} is surely the function of the product $E_c H_c$. The effect of the magnetic-field induced modification of the underlying magnetic texture on the domain-wall dynamics is negligible for $\mu_0 H_c$ of smaller than 0.1 T.

To elucidate the origin of the temperature-induced change in the switching speed, we investigate the temperature dependence of the dynamic properties of the domain wall. Figure 5.11(a) shows the temperature dependence of the electric-field based mobility μ_E . Divergent enhancement in μ_E , which is advantageous for the faster switching process, with approaching T_N is observed. Assuming the Gilbert constant α_0 in Eq. (5.12) to be independent of temperature and that γ_{zz} is proportional to \mathcal{J} [13], the enhancement of μ_E might be ascribed to the increase of the domain-wall thickness λ_{DW} near the T_N . We also examined the temperature dependence of the pinning field E_p . Since it is hard to clearly separate the contribution from the creep motion v_0 , we show the temperature dependence of $E_p - (v_0/\mu_E)$, which we simply regard as the pinning field in the following, in Fig. 5.11(b). The faster domain inversion at higher temperature in a fixed electric field in Figs. 5.8(a) and (b) is also attributable to the decrease in pinning field. The value and the temperature dependence of the pinning electric field is similar to that of the coercive electric field to switch domains, which is determined from the $I-E_c$ curve [see the inset of Fig. 5.11(b)]. The vanishing behavior in E_{coercive} near the critical temperature is similar to that in other linear ME materials [100, 101]. The resemblance of E_p with E_{coercive} indicates that the domain reversal occurs when the electric field reaches the threshold value where the domain wall is depinned and set to motion. The effect of the domain nucleation seems absent even in

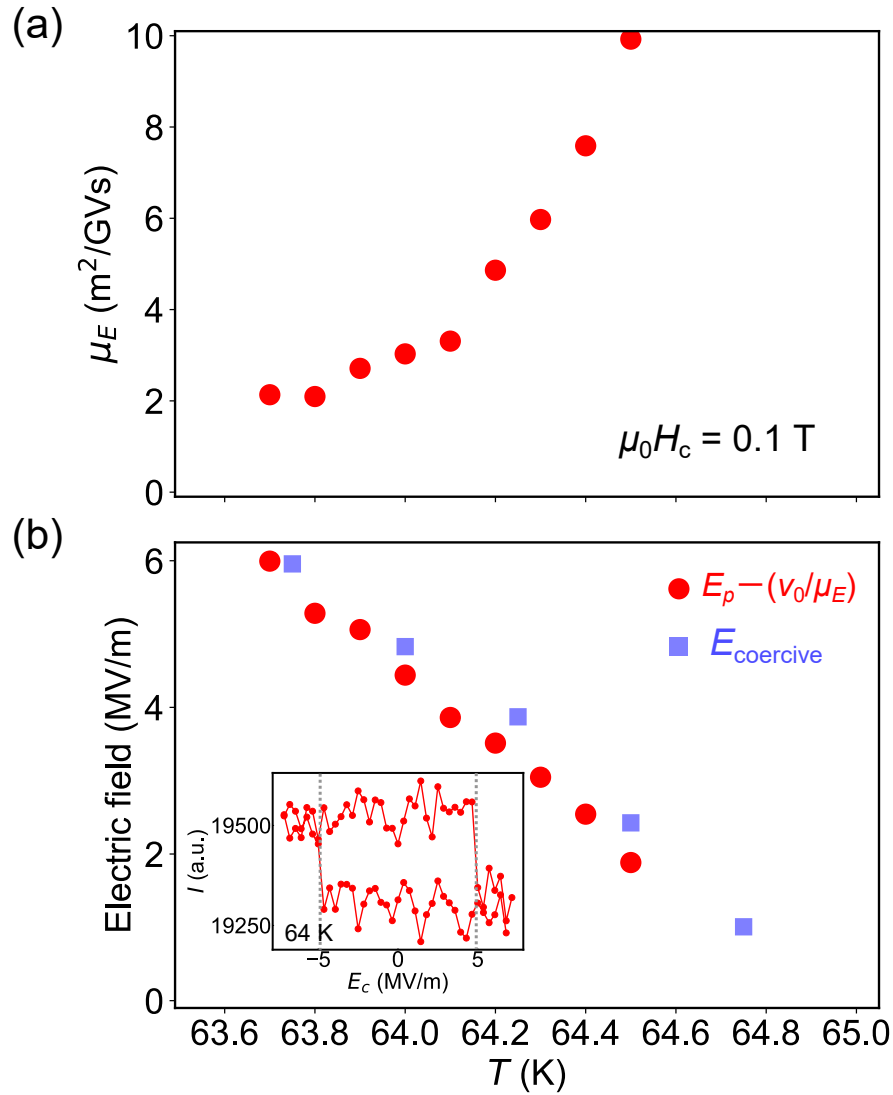


Figure 5.11: Temperature dependence of (a) μ_E and (b) E_p . Measurements were performed for the different multidomain state from Fig. 5.10. In (b), temperature dependence of the coercive electric field E_{coercive} to switch the antiferromagnetic domain is also shown. The inset of (b) shows the change in transmitted light intensity for a cycle of electric field, where the definition of E_{coercive} is graphically shown by gray dotted lines.

the determination of the coercive field.

5.3 Summary

In this chapter, we have performed an MCHD-based imaging study of the antiferromagnetic domain dynamics in a collinear antiferromagnet MnTiO_3 . Exploiting the memory effect in the domain reversal, which is clarified in the imaging of the quasistatic static switching process, we captured millisecond dynamics in the antiferromagnetic domain switching in driving electric and magnetic fields. Switching dynamics is dominated by the domain-wall displacement within the current experiment. By the detailed investigation of the domain-wall dynamics, we revealed dynamical properties of the electric and magnetic fields driven motion of the antiferromagnetic domain wall.

Chapter 6

Conclusion

In this thesis, we have studied the antiferromagnet MnTiO_3 , where the toroidal moment is activated by antiferromagnetic ordering with zero magnetization. Dynamic aspects of ME effects have been investigated by means of spectroscopic and imaging experiments. The major findings are summarized as follows.

Observation of MCHD

We observed MCHD spontaneously arising from antiferromagnetic ordering. The toroidal moment of purely antiferromagnetic origin, which gives rise to antisymmetric ME coupling in optical frequency, is shown to work as a rectifier for an unpolarized light beam. The dichroism was confirmed by the investigation of the absorption spectra with manipulating the direction of the toroidal moment. Exploiting the controllability of the toroidal moment, we achieved binary switching of color by sweeping electric and magnetic fields.

Magneto-chiral imaging of domain patterns

We demonstrated MCHD-based imaging of the antiferromagnetic domain pattern. Simultaneous breaking of \mathcal{P} and \mathcal{T} symmetries enabled us to visualize antiphase domain patterns with the linear optical effect even in the presence of \mathcal{PT} symmetry. Two antiferromagnetic states with the toroidal moment in opposite directions were distinguished by the difference in transmitted light intensity. The present imaging technique has several advantageous features such as polarization independency and exposure time less than a few seconds.

Imaging study of domain reversal dynamics

We captured millisecond dynamics in the antiferromagnetic domain reversal process under the abruptly switched electric fields. The temporal evolution of domain pattern is not accessible without imaging experiments. Both quasistatic and dynamic reversal process was found to be solely described by the domain-wall displacement in various temperature and driving fields. By the detailed investigation of the dynamic properties of domain walls, we revealed that change

in domain-wall mobility explains the observed thermal and electric-field effects on the switching speed.

The results in this thesis show that collinear antiferromagnetic ordering in an ME antiferromagnet induces the nonreciprocal optical effect in visible range and unveil static and dynamic properties of antiferromagnetic domain patterns in driving electric and magnetic fields. Observation of MCHD in the absence of magnetization should stimulate further exploration of various kinds of magnetochiral effects including nonreciprocal transport of electron, phonon, and magnon in antiferromagnetic materials. The structural simplicity of the target material MnTiO_3 allows us to apply the present MCHD-based imaging technique to investigate patterns and dynamics of antiferromagnetic domain walls, which is indispensable for the manipulation of the functional antiferromagnets.

Acknowledgement

This research was conducted under the guidance of Professor Taka-hisa Arima and Professor Yusuke Tokunaga. First and foremost, I would like to thank them for encouraging me and supporting my research continuously in every aspect. I also would like to express my gratefulness to Dr. Takashi Kurumaji for supporting the experiments at Tohoku University, which is not covered in this thesis, and helpful comments.

For the doctoral dissertation defence, I would like to thank Professor Tsuyoshi Kimura, Professor Noriaki Kida, Professor Yoshimitsu Kohama and Professor Tsuyohito Ito for acceptance to review this thesis and for valuable comments.

I am grateful to Professor Shojiro Kimura and Professor Nobuyuki Abe for supporting my research at Tohoku University. I thank my MERIT mentor, Professor Katsumoto Shingo, for useful comments on my work. I also would like to thank all the current members and many of alumni of Arima-Tokunaga Group for support for the research and life in lab.

Last, but not least, I thank very much for my parents for their continuous encouragement and support during my student life.

Appendix A

Processing for obtaining difference images

Magnetic domain patterns were analyzed based on the difference in transmitted light intensity as a function of the two-dimensional pixel position \mathbf{r} between the images obtained at a given condition I_{main} and that at a reference condition I_{ref} [see Figs. A.1(a) and (b)]. The $2L + 1 \times 2L + 1$ -pixel median filter was applied to both images as

$$\begin{cases} I_{\text{main}}(\mathbf{r}) & \xrightarrow{2L+1 \text{ pixel median filter}} I_{\text{main}}^L(\mathbf{r}) \\ I_{\text{ref}}(\mathbf{r}) & \xrightarrow{2L+1 \text{ pixel median filter}} I_{\text{ref}}^L(\mathbf{r}) \end{cases}$$

for the noise reduction. We employed $L = 10$ for original images with $S = 1024 \times 1024$ pixels. We adopted two different display methods for isothermal field-induced changes and for thermal changes.

Difference from isothermally recorded reference images

Reference images analyzed in Ch. 5 were recorded at the same temperature as main images. In this case, the difference $I_{\text{diff}}^L(\mathbf{r})$ between two images was computed as

$$I_{\text{diff}}^L(\mathbf{r}) = I_{\text{main}}^L(\mathbf{r}) - I_{\text{ref}}^L(\mathbf{r} - \boldsymbol{\rho}).$$

$\boldsymbol{\rho}$ was computed from the difference in positions of the edge of the circular field of view between two images. $\boldsymbol{\rho}$ is almost negligible for the isothermally recorded reference images. To remove contributions from inhomogeneous distribution of incident light and thickness of the sample, we obtained $\bar{I}_{\text{diff}}^L(\mathbf{r})$ as

$$\bar{I}_{\text{diff}}^L(\mathbf{r}) = \frac{I_{\text{diff}}^L(\mathbf{r})\Omega(\mathbf{r})}{I_{\text{ref}}^L(\mathbf{r} - \boldsymbol{\rho})}.$$

The denominator reflects the spatial inhomogeneity in the transmitted light intensity originating from incident light distribution and the sample thickness. Region function $\Omega(\mathbf{r})$ takes unity if \mathbf{r} is in the field of view and zero if \mathbf{r} is out of the field of view. See Fig. A.1(c) for the relation

among I_{main}^L , I_{ref}^L , and \bar{I}_{diff}^L . From $\bar{I}_{\text{diff}}^L(\mathbf{r})$, we obtained 8-bit TIFF images $\mathcal{I}^L(\mathbf{r})$ as follows;

$$\mathcal{I}^L(\mathbf{r}) = \begin{cases} 0 & \text{if } \bar{I}_{\text{diff}}^L(\mathbf{r}) < \alpha \\ 255\Omega(\mathbf{r}) \left(\frac{\bar{I}_{\text{diff}}^L(\mathbf{r}) - \alpha}{\beta - \alpha} \right) & \text{if } \alpha \leq \bar{I}_{\text{diff}}^L(\mathbf{r}) \leq \beta. \\ 255\Omega(\mathbf{r}) & \text{if } \bar{I}_{\text{diff}}^L(\mathbf{r}) > \beta \end{cases} \quad (\text{A.1})$$

Unless otherwise noticed, we employed $(\alpha, \beta) = (-0.0125, 0.00125)$ to obtain difference images where the bright monodomain state is used as references, while we did $(\alpha, \beta) = (-0.00125, 0.0125)$ where the dark monodomain state is used as reference.

Difference from reference images recorded in the paramagnetic phase

The reference images in Ch. 4 in the main text were recorded at a temperature just above T_N . To cope with the temperature dependence of the transmitted light intensity of nonmagnetic origin, we computed the difference $I_{\text{diff}}^L(\mathbf{r})$ between two normalized images as

$$I_{\text{diff}}^L(\mathbf{r}) = \frac{I_{\text{main}}^L(\mathbf{r})}{\frac{1}{S} \int d\mathbf{r} I_{\text{main}}^L(\mathbf{r})} - \frac{I_{\text{ref}}^L(\mathbf{r} - \boldsymbol{\rho})}{\frac{1}{S} \int d\mathbf{r} I_{\text{ref}}^L(\mathbf{r})}.$$

The nonmagnetic contribution to the change in intensity of transmitted light can originate from the thermal displacement of the optical stage against the light source, temperature dependence of the optical absorption irrelevant to the magnetism, and so on. Correspondingly, $\bar{I}_{\text{diff}}^L(\mathbf{r})$ here was computed as

$$\bar{I}_{\text{diff}}^L(\mathbf{r}) = \frac{I_{\text{diff}}^L(\mathbf{r})\Omega(\mathbf{r})}{\frac{I_{\text{ref}}^L(\mathbf{r} - \boldsymbol{\rho})}{\frac{1}{S} \int d\mathbf{r} I_{\text{ref}}^L(\mathbf{r})}}.$$

From this $\bar{I}_{\text{diff}}^L(\mathbf{r})$, we obtained 8-bit TIFF images $\mathcal{I}^L(\mathbf{r})$ according to Eq. (A.1). This display method is also used to obtain difference image in Fig. 5.9(b) where the temporal drift of the transmitted light intensity might occur. We employed $(\alpha, \beta) = (-0.0125, 0.0125)$ to obtain difference images.

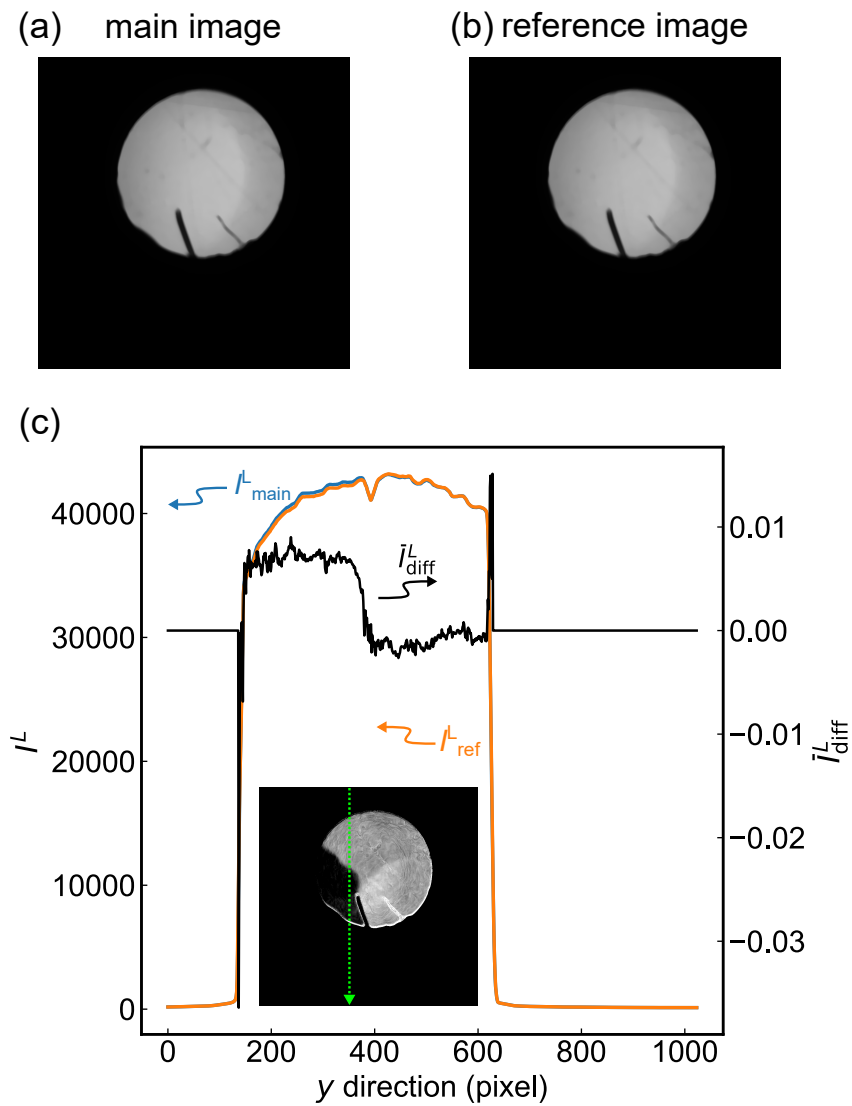


Figure A.1: Image processing to obtain the middle panel of Fig. 5.5(c). (a),(b) TIFF image obtained from (a) I^L_{main} and (b) I^L_{ref} . Scale bars are omitted. (c) Profiles of I^L_{main} , I^L_{ref} , and \bar{I}^L_{diff} along the path represented by a green arrow on the difference image in the inset.

Appendix B

Possible microscopic descriptions of the toroidal moment in MnTiO_3

Here, we propose that the on-site d - p hybridization in Mn^{2+} ions gives rise to the toroidal moment \mathbf{T} along the ordered magnetic moment in MnTiO_3 . We show that the z component of toroidal moment arises from the spatial distribution of the orbital contribution to the magnetic dipole moments when Mn^{2+} ion with the d^5 electronic configuration and easy-axis magnetic ordering is placed in a chiral environment with the point group symmetry C_3 . In this chapter, we use atomic units, where e , \hbar , and the Bohr radius a_0 are equal to one.

Model

We consider a minimal model of single Mn^{2+} ion placed in a chiral environment with the point group symmetry C_3 . The three-fold axis is oriented along the z direction. We consider the on-site hybridization between $3d$ and $4p$ orbitals. Mn^{2+} ion is characterized by the $3d^5$ electronic configuration.

Instead of dealing with multiplets composed of five electrons, we deal with five single-electron states and add up contributions from each state to calculate the toroidal moment. A single-electron state in the $3d$ orbital is uniquely determined by the set (l_z, s_z) of the z -component of the orbital and spin angular momentums. Hund's rule allows us to focus on the single-electron states with $s_z = 1/2$ because the ordered magnetic moments lie along the three-fold axis in the antiferromagnetic phase of MnTiO_3 . In the same way, a single-electron state in the $4p$ orbital is uniquely determined by the set $(l_z, s_z = 1/2)$. By $|d, l_z\rangle$ ($|p, l_z\rangle$), we denote the single-electron state in the $3d$ ($4p$) orbital with $(l_z, s_z = 1/2)$. Hereafter the matrix representation of the

operator \mathcal{O} is given as

$$\begin{pmatrix} \langle d, -2 | \mathcal{O} | d, -2 \rangle & \cdots & \langle d, -2 | \mathcal{O} | d, 2 \rangle & \langle d, -2 | \mathcal{O} | p, -1 \rangle & \cdots & \langle d, -2 | \mathcal{O} | p, 1 \rangle \\ \vdots & \ddots & \vdots & \vdots & \ddots & \vdots \\ \langle d, 2 | \mathcal{O} | d, -2 \rangle & \cdots & \langle d, 2 | \mathcal{O} | d, 2 \rangle & \langle d, 2 | \mathcal{O} | p, -1 \rangle & \cdots & \langle d, 2 | \mathcal{O} | p, 1 \rangle \\ \langle p, -1 | \mathcal{O} | d, -2 \rangle & \cdots & \langle p, -1 | \mathcal{O} | d, 2 \rangle & \langle p, -1 | \mathcal{O} | p, -1 \rangle & \cdots & \langle p, -1 | \mathcal{O} | p, 1 \rangle \\ \vdots & \ddots & \vdots & \vdots & \ddots & \vdots \\ \langle p, 1 | \mathcal{O} | d, -2 \rangle & \cdots & \langle p, 1 | \mathcal{O} | d, 2 \rangle & \langle p, 1 | \mathcal{O} | p, -1 \rangle & \cdots & \langle p, 1 | \mathcal{O} | p, 1 \rangle \end{pmatrix}. \quad (\text{B.1})$$

The Hamiltonian of our model is given by

$$\mathcal{H} = \mathcal{H}_{\text{atom}} + \mathcal{H}_{\text{SO}} + \mathcal{H}_{\text{CEF}}. \quad (\text{B.2})$$

$\mathcal{H}_{\text{atom}}$ in Eq. (B.2) describes the atomic energy difference between $3d$ and $4p$ orbitals. In the matrix form, $\mathcal{H}_{\text{atom}}$ is expressed as

$$H_{\text{atom}} = \Delta_{dp} \begin{pmatrix} 0 & \cdots & 0 & 0 & \cdots & 0 \\ \vdots & \ddots & \vdots & \vdots & \ddots & \vdots \\ 0 & \cdots & 0 & 0 & \cdots & 0 \\ 0 & \cdots & 0 & 1 & \cdots & 0 \\ \vdots & \ddots & \vdots & \vdots & \ddots & \vdots \\ 0 & \cdots & 0 & 0 & \cdots & 1 \end{pmatrix}, \quad (\text{B.3})$$

using $\Delta_{dp} > 0$.

\mathcal{H}_{SO} in Eq. (B.2) describes the atomic spin-orbit coupling. Generally, \mathcal{H}_{SO} is expressed as $\mathcal{H}_{\text{SO}} = \sum_i \xi_i \mathbf{l}_i \cdot \mathbf{s}_i$ using the coupling constant ξ_i . Here, for simplicity, we set ξ_i to be λ regardless whether the i -th electron is in the $3d$ orbital or in the $4p$ orbital. In the matrix form, \mathcal{H}_{SO} is expressed as

$$H_{\text{SO}} = \frac{\lambda}{2} \begin{pmatrix} -2 & \cdots & 0 & 0 & \cdots & 0 \\ \vdots & \ddots & \vdots & \vdots & \ddots & \vdots \\ 0 & \cdots & 2 & 0 & \cdots & 0 \\ 0 & \cdots & 0 & -1 & \cdots & 0 \\ \vdots & \ddots & \vdots & \vdots & \ddots & \vdots \\ 0 & \cdots & 0 & 0 & \cdots & 1 \end{pmatrix}. \quad (\text{B.4})$$

\mathcal{H}_{CEF} in Eq. (B.2) describes the crystalline electric field (CEF). For the atom placed at the origin, the CEF Hamiltonian is expanded by the spherical harmonics $Y_{km}(\theta, \phi)$ as,

$$\mathcal{H}_{\text{CEF}} = \sum_{k,m} A_{km} r^k C_m^{(k)}(\theta, \phi), \quad (\text{B.5})$$

where

$$C_m^{(k)}(\theta, \phi) = \sqrt{\frac{4\pi}{2k+1}} Y_{km}(\theta, \phi). \quad (\text{B.6})$$

We decompose the CEF Hamiltonian into the sum of the even-parity one $\mathcal{H}_{\text{CEF,even}}$ and the odd-parity one $\mathcal{H}_{\text{CEF,odd}}$. Hereafter, we use spherical coordinates with the polar axis parallel to the three-fold axis. With imposing the point group symmetry C_3 , $\mathcal{H}_{\text{CEF,even}}$ and $\mathcal{H}_{\text{CEF,odd}}$ become

$$\mathcal{H}_{\text{CEF,even}} = \mathcal{H}_{\text{CEF,cubic}} + \mathcal{H}_{\text{CEF,trigonal}}, \quad (\text{B.7})$$

$$\mathcal{H}_{\text{CEF,odd}} = \mathcal{H}_{\text{CEF,polar}} + \mathcal{H}_{\text{CEF,chiral}}, \quad (\text{B.8})$$

where

$$\mathcal{H}_{\text{CEF,cubic}} = -14Dq \left\{ C_0^{(4)} + \sqrt{\frac{10}{7}} (C_3^{(4)} - C_{-3}^{(4)}) \right\}, \quad (\text{B.9})$$

$$\mathcal{H}_{\text{CEF,trigonal}} = \gamma_{D_{3d}} C_0^{(2)}, \quad (\text{B.10})$$

$$\mathcal{H}_{\text{CEF,polar}} = \gamma_{\text{polar},1} C_0^{(1)} + \gamma_{\text{polar},3} C_0^{(3)} + \gamma_{\text{polar}} \left\{ C_3^{(3)} - C_{-3}^{(3)} \right\}, \quad (\text{B.11})$$

$$\mathcal{H}_{\text{CEF,chiral}} = i\tilde{\gamma}_{\text{chiral}} \left\{ C_3^{(3)} + C_{-3}^{(3)} \right\}. \quad (\text{B.12})$$

$\mathcal{H}_{\text{CEF,cubic}}$ in Eq. (B.9) describes the CEF Hamiltonian in the point group symmetry O_h . $10Dq$ represents the energy difference between so-called e_g orbitals and t_{2g} orbitals. In the matrix form, $\mathcal{H}_{\text{CEF,cubic}}$ is expressed as,

$$H_{\text{CEF,cubic}} = Dq \begin{pmatrix} -\frac{2}{3} & 0 & 0 & -\frac{10\sqrt{2}}{3} & 0 & 0 & 0 & 0 \\ 0 & \frac{8}{3} & 0 & 0 & \frac{10\sqrt{2}}{3} & & & \\ 0 & 0 & -4 & 0 & 0 & \vdots & \vdots & \vdots \\ -\frac{10\sqrt{2}}{3} & 0 & 0 & \frac{8}{3} & 0 & & & \\ 0 & \frac{10\sqrt{2}}{3} & 0 & 0 & -\frac{2}{3} & 0 & 0 & 0 \\ 0 & \dots & & & 0 & 0 & 0 & 0 \\ 0 & \dots & & & 0 & 0 & 0 & 0 \\ 0 & \dots & & & 0 & 0 & 0 & 0 \end{pmatrix}. \quad (\text{B.13})$$

$\mathcal{H}_{\text{CEF,trigonal}}$ in Eq. (B.10) describes the other \mathcal{P} -even contribution in \mathcal{H}_{CEF} . $\gamma_{D_{3d}}$ is a real coefficient. $\mathcal{H}_{\text{CEF,even}} = \mathcal{H}_{\text{CEF,cubic}} + \mathcal{H}_{\text{CEF,trigonal}}$ describes the CEF Hamiltonian in the D_{3d} site symmetry. $\mathcal{H}_{\text{CEF,trigonal}}$ originates from the elongation of the MnO_6 octahedron along the three-fold axis.

$\mathcal{H}_{\text{CEF,polar}}$ in Eq. (B.11) and $\mathcal{H}_{\text{CEF,chiral}}$ in Eq. (B.12) describe the \mathcal{P} -odd contributions in the CEF Hamiltonian \mathcal{H}_{CEF} which hybridize the $3d$ orbitals and the $4p$ orbitals. $\gamma_{\text{polar},1}$, $\gamma_{\text{polar},3}$, γ_{polar} , and $\tilde{\gamma}_{\text{chiral}}$ are real coefficients. $\mathcal{H}_{\text{CEF,polar}}$ originates from the polar distortion of the MnO_6 octahedron and $\mathcal{H}_{\text{CEF,even}} + \mathcal{H}_{\text{CEF,polar}}$ describes the CEF Hamiltonian in the C_{3v} site symmetry. $\mathcal{H}_{\text{CEF,chiral}}$ originates from the chiral twist of the MnO_6 octahedron along the three-fold axis and $\mathcal{H}_{\text{CEF,even}} + \mathcal{H}_{\text{CEF,chiral}}$ describes the CEF Hamiltonian in the D_3 site symmetry.

In the matrix form, $\mathcal{H}_{\text{CEF, chiral}}$ is expressed as,

$$\frac{3\tilde{\gamma}_{\text{chiral}}}{7} \begin{pmatrix} 0 & \cdots & 0 & 0 & 0 & -i \\ & & & 0 & 0 & 0 \\ \vdots & \ddots & \vdots & 0 & 0 & 0 \\ & & & 0 & 0 & 0 \\ 0 & \cdots & 0 & -i & 0 & 0 \\ 0 & 0 & 0 & 0 & i & 0 & 0 & 0 \\ 0 & 0 & 0 & 0 & 0 & 0 & 0 & 0 \\ i & 0 & 0 & 0 & 0 & 0 & 0 & 0 \end{pmatrix}. \quad (\text{B.14})$$

Formulation of the toroidal moment

From Eq. (1.8), the contribution from the spatial distribution of the orbital part of the magnetic dipoles $\mathbf{m}_{\mathbf{L}} = -\mu_{\text{B}}\hat{\mathbf{l}}/\hbar$ to the toroidal moment \mathbf{t} is written as

$$\mathbf{t}_{\mathbf{L}} = \frac{1}{2} \sum_i \mathbf{r}_i \times \left(-\frac{\mu_{\text{B}}}{\hbar} \mathbf{l}_i \right). \quad (\text{B.15})$$

Using the symmetrized expression [102], the z -component of $\mathbf{t}_{\mathbf{L}}$ is proportional to

$$\hat{\tau}_{\mathbf{L},z} = \frac{(\hat{x}\hat{l}_y - \hat{y}\hat{l}_x) + (\hat{x}\hat{l}_y - \hat{y}\hat{l}_x)^\dagger}{2}. \quad (\text{B.16})$$

We evaluate $\hat{\tau}_{\mathbf{L},z}$ in Eq. (B.16). Matrix representations of the position operators are calculated as

$$\langle d, m | \hat{x} | p, m' \rangle = \int_0^\infty dr \int_0^{2\pi} d\phi \int_0^\pi d\theta (r \cos \phi \sin \theta) r^2 \sin \theta R_{32}(r) Y_2^m(\theta, \phi) \left\{ R_{41}(r) Y_1^{m'}(\theta, \phi) \right\}^*, \quad (\text{B.17})$$

and

$$\langle d, m | \hat{y} | p, m' \rangle = \int_0^\infty dr \int_0^{2\pi} d\phi \int_0^\pi d\theta (r \sin \phi \sin \theta) r^2 \sin \theta R_{32}(r) Y_2^m(\theta, \phi) \left\{ R_{41}(r) Y_1^{m'}(\theta, \phi) \right\}^*, \quad (\text{B.18})$$

using

$$R_{nl}(r) = 2^{l+1} e^{-\frac{r}{n}} \sqrt{\frac{(-l+n-1)!}{n^4(l+n)!}} \left(\frac{r}{n}\right)^l L_{-l+n-1}^{2l+1} \left(\frac{2r}{n}\right), \quad (\text{B.19})$$

with the associated Laguerre polynomials L_n^k . For any set of (m, m') , $\langle d, m | \hat{x} | d, m' \rangle$ and $\langle p, m | \hat{x} | p, m' \rangle$ are zero and the same hold for \hat{y} . Since we are using basis sets which diagonalize \hat{l}_z , the matrix elements for \hat{l}_x and \hat{l}_y are computed as

$$\langle d, m | \hat{l}_x | d, m' \rangle = \frac{1}{2} (\delta_{m, m'+1} + \delta_{m+1, m'}) \sqrt{2(2+1) - mm'}, \quad (\text{B.20})$$

$$\langle d, m | \hat{l}_y | d, m' \rangle = \frac{1}{2i} (\delta_{m, m'+1} - \delta_{m+1, m'}) \sqrt{2(2+1) - mm'}, \quad (\text{B.21})$$

$$\langle p, m | \hat{l}_x | p, m' \rangle = \frac{1}{2} (\delta_{m, m'+1} + \delta_{m+1, m'}) \sqrt{1(1+1) - mm'}, \quad (\text{B.22})$$

$$\langle p, m | \hat{l}_y | p, m' \rangle = \frac{1}{2i} (\delta_{m, m'+1} - \delta_{m+1, m'}) \sqrt{1(1+1) - mm'}. \quad (\text{B.23})$$

For any set of (m, m') , $\langle d, m | \hat{l}_x | p, m' \rangle$ and $\langle d, m | \hat{l}_y | p, m' \rangle$ are zero. Using Eqs. (B.17)-(B.23), the matrix representation of $\hat{\tau}_{\mathbf{L},z}$ is computed as

$$\frac{2\sqrt{2}\mu}{\sqrt{5}} \begin{pmatrix} 0 & \dots & 0 & 0 & 0 & 0 & 0 & 0 \\ & & & -\sqrt{3}i & 0 & 0 & & \\ \vdots & \ddots & \vdots & 0 & -2i & 0 & & \\ & & & 0 & 0 & -\sqrt{3}i & & \\ 0 & \dots & 0 & 0 & 0 & 0 & 0 & 0 \\ 0 & \sqrt{3}i & 0 & 0 & 0 & 0 & 0 & 0 \\ 0 & 0 & 2i & 0 & 0 & 0 & 0 & 0 \\ 0 & 0 & 0 & \sqrt{3}i & 0 & 0 & 0 & 0 \end{pmatrix}, \quad (\text{B.24})$$

using $\mu = \frac{7962624}{5764801}$.

Results and discussions

We calculate the expectation value of $\hat{\tau}_{\mathbf{L},z}$ as

$$\langle \hat{\tau}_{\mathbf{L},z} \rangle = \sum_{j=1}^8 \langle j | \hat{\tau}_{\mathbf{L},z} | j \rangle f(\varepsilon_j). \quad (\text{B.25})$$

$|j\rangle$ and ε_j are the eigenstate and eigenvalue of \mathcal{H} . $f(\varepsilon)$ is the Fermi-Dirac distribution function. The chemical potential is set so that electron filling $\sum_{j=1}^8 f(\varepsilon_j)$ becomes five.

Figure B.1 shows the $\tilde{\gamma}_{\text{chiral}}$ dependence of $\langle \hat{\tau}_{\mathbf{L},z} \rangle$. Results are obtained for the model parameters, $\Delta_{dp} = 20$, $\lambda = 1$, $Dq = 1$, $\gamma_{D_{3d}} = \gamma_{\text{polar},1} = \gamma_{\text{polar},3} = \gamma_{\text{polar}} = 0$, and $k_{\text{B}}T = 0.1$. $\langle \hat{\tau}_{\mathbf{L},z} \rangle$ is induced in proportion to the parameter $\tilde{\gamma}_{\text{chiral}}$, which represents the strength of the chiral contribution in the CEF Hamiltonian. The result in Fig. B.1 suggests that the toroidal moment is induced parallel to the ordered magnetic moment in the presence of the chiral CEF.

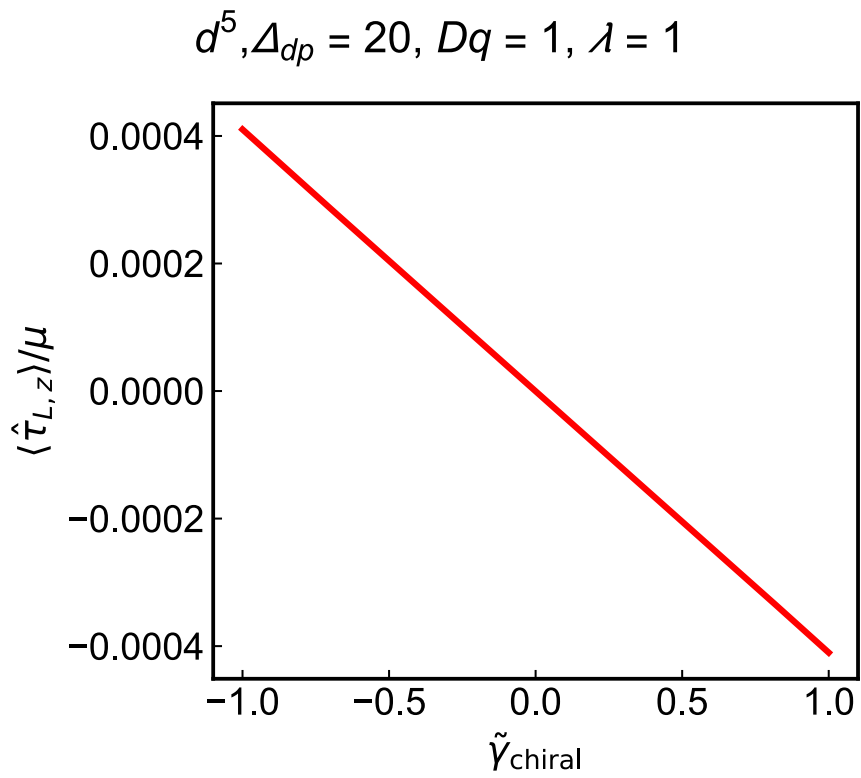


Figure B.1: $\mathcal{H}_{\text{CEF,chiral}}$ dependence of $\langle \hat{\tau}_{L,z} \rangle$ for the d^5 electric configuration. $\gamma_{D_{3d}} = \tilde{\gamma}_{\text{polar},\alpha} = \tilde{\gamma}_{\text{polar},\beta} = \gamma_{\text{polar}} = 0$ and $k_{\text{B}}T = 0.1$.

Appendix C

Axial degree of freedom in MnTiO₃

The presence of the axial moment which characterizes ferroaxial ordering is not forbidden by the point group symmetry $\bar{3}$ in MnTiO₃. The ferroaxial moment \mathcal{A} is a \mathcal{T} -even axial vector. Microscopically, \mathcal{A} is computed as

$$\mathcal{A} = \frac{1}{2} \sum_i \mathbf{r}_i \times \mathbf{p}(\mathbf{r}_i), \quad (\text{C.1})$$

using electric dipoles \mathbf{p} at positions \mathbf{r}_i . In the ilmenite structure with the point group symmetry $\bar{3}$, the c component \mathcal{A}_c of \mathcal{A} is not zero while the in-plane components \mathcal{A}_a and \mathcal{A}_{b^*} are absent due to the three-fold symmetry. In the absence of external fields, $\mathcal{A}_c > 0$ and $\mathcal{A}_c < 0$ states are energetically degenerated.

The sign of the coupling constant g_t/g_{\parallel} [see Eq. 3.7] which connects the antisymmetric term γ_t in the ME tensor with diagonal term γ_{\parallel} is determined by the sign of \mathcal{A}_c . Let us assume that the ME tensor γ for the $L_c > 0$ and $\mathcal{A}_c > 0$ state is given as

$$\gamma(L_c > 0, \mathcal{A}_c > 0) = \begin{pmatrix} a_1 & a_2 & 0 \\ -a_2 & a_1 & 0 \\ 0 & 0 & a_3 \end{pmatrix}, \quad (\text{C.2})$$

using constants a_1 , a_2 , and a_3 . Since the ME tensor is odd under \mathcal{T} operation which inverts the direction of \mathbf{L} , γ for the $L_c < 0$ and $\mathcal{A}_c > 0$ state becomes

$$\gamma(L_c < 0, \mathcal{A}_c > 0) = \hat{\mathcal{T}}^\dagger \gamma(L_c > 0, \mathcal{A}_c > 0) \hat{\mathcal{T}} = \begin{pmatrix} -a_1 & -a_2 & 0 \\ a_2 & -a_1 & 0 \\ 0 & 0 & -a_3 \end{pmatrix}. \quad (\text{C.3})$$

Judging from Eq. (C.1), the ferroaxial moment \mathcal{A} is odd under the two-fold rotation operation along the axis perpendicular to \mathcal{A} . By applying the two-fold rotation operation around the a axis $\hat{C}_{2,a}$ to $\gamma(L_c > 0, \mathcal{A}_c > 0)$ in Eq. (C.2), we obtain

$$\gamma(L_c > 0, \mathcal{A}_c < 0) = \hat{C}_{2,a}^\dagger \gamma(L_c > 0, \mathcal{A}_c > 0) \hat{C}_{2,a} = \begin{pmatrix} a_1 & -a_2 & 0 \\ a_2 & a_1 & 0 \\ 0 & 0 & a_3 \end{pmatrix}. \quad (\text{C.4})$$

Here we assume that $\mathbf{L} \parallel \mathbf{c}$ is invariant under the two-fold rotation. Using Eq. (C.4), $\gamma(L_c < 0, \mathcal{A}_c < 0)$ is computed as

$$\gamma(L_c < 0, \mathcal{A}_c < 0) = \hat{\mathcal{T}}^\dagger \gamma(L_c > 0, \mathcal{A}_c < 0) \hat{\mathcal{T}} = \begin{pmatrix} -a_1 & a_2 & 0 \\ -a_2 & -a_1 & 0 \\ 0 & 0 & -a_3 \end{pmatrix}. \quad (\text{C.5})$$

From Eqs. (C.2)-(C.5), we can see that values of $g_t/g_{\parallel} = \gamma_{\parallel}/\gamma_t$ is a_3/a_2 for the $\mathcal{A}_c > 0$ state and $-a_3/a_2$ for the $\mathcal{A}_c < 0$ state.

Poling of ferrotoroidic domains by electric and magnetic fields along the c axis in Ch. 5 evidences that the MnTiO₃ samples are in the ferroaxial monodomain state. Since MCHD is caused by the toroidal moment acting like a rectifier for light beam, the present imaging technique based on MCHD in principle visualizes the distribution of T^c . Judging from the monocolored difference image taken in the external fields larger than the coercive fields [e.g. see the right panel of Fig. 5.5(b)], the sample is in ferrotoroidic monodomain state. In the ferrotoroidic monodomain state, the sign of γ_t is homogeneous over the sample [see Eq. 3.8]. Since the $\gamma_{\parallel} > 0$ ($\gamma_{\parallel} < 0$) state is energetically favored in the external fields with $E_c H_c > 0$ ($E_c H_c < 0$), the sign of γ_{\parallel} should be also homogenous over the sample in external electric and magnetic fields along the c axis larger than coercive fields. Considering the relation between the signs of \mathcal{A}_c and $\gamma_{\parallel}/\gamma_t$, we can conclude that the direction of the ferroaxial moment $\mathbf{A} \parallel \mathbf{c}$ is aligned in the same direction in the observed ferrotoroidic state realized in electric and magnetic fields along the c axis.

When a MnTiO₃ sample is in a ferroaxial multidomain state, ferrotoroidic domains are not poled by the application of electric and magnetic fields along the c axis. In such case, MCHD-based imaging in electric and magnetic fields along the c axis larger than coercive fields visualizes the distribution of \mathcal{A}_c . If we assume a_3 in Eqs. (C.2)-(C.5) to be positive, the $L_c > 0$ and $\mathcal{A}_c > 0$ state and the $L_c > 0$ and $\mathcal{A}_c < 0$ state are favored by external fields with $E_c H_c > 0$. Since the sign of γ_t is opposite, these two states with \mathcal{A}_c in opposite signs should be distinguished with the MCHD-based imaging technique. The absence of ferroaxial domain wall in MnTiO₃ would be related with the absence of the ferroaxial phase transition $\bar{3}m \rightarrow \bar{3}$ [103] below the melting point in MnTiO₃, in sharp contrast with the case of NiTiO₃ [104] with the same crystallographic structure.

References

- [1] L. D. Landau and E. M. Lifshitz, *Electrodynamics of continuous media*, Butterworth-Heinemann (1984).
- [2] H. Schmid, *Ferroelectrics* **162**, 317 (1994).
- [3] N. A. Spaldin, M. Fiebig, and M. Mostovoy, *J. Phys. Condens. Matter* **20**, 434203 (2008).
- [4] Y. Gao, D. Vanderbilt, and D. Xiao, *Phys. Rev. B* **97**, 134423 (2018).
- [5] A. Shitade, H. Watanabe, and Y. Yanase, *Phys. Rev. B* **98**, 020407 (2018).
- [6] D. N. Astrov, *Sov. Phys. JETP* **13**, 729 (1961).
- [7] I. E. Dzyaloshinskii, *Sov. Phys. JETP* **10**, 628 (1960).
- [8] E. Fischer, G. Gorodetsky, and R. M. Hornreich, *Sol. Stat. Comm.* **10**, 1127 (1972).
- [9] N. D. Khanh, N. Abe, H. Sagayama, A. Nakao, T. Hanashima, R. Kiyonagi, Y. Tokunaga, and T. Arima, *Phys. Rev. B* **93**, 075117 (2016).
- [10] N. Lee, D. G. Oh, S. Choi, J. Y. Moon, J. H. Kim, H. J. Shin, K. Son, J. Nuss, V. Kiryukhin, and Y. J. Choi, *Sci. Rep.* **10**, 12362 (2020).
- [11] A. Maignan and C. Martin, *Phys. Rev. B* **97**, 161106 (2018).
- [12] S. N. Panja, L. Harnagea, J. Kumar, P. K. Mukharjee, R. Nath, A. K. Nigam, and S. Nair, *Phys. Rev. B* **98**, 024410 (2018).
- [13] N. Mufti, G. R. Blake, M. Mostovoy, S. Riyadi, A. A. Nugroho, and T. T. M. Palstra, *Phys. Rev. B* **83**, 104416 (2011).
- [14] S. Mishra, P. Yanda, and A. Sundaresan, *Phys. Rev. B* **103**, 214443 (2021).
- [15] G. T. Rado, *Phys. Rev. Lett.* **13**, 335 (1964).
- [16] S. C. Abrahams, J. M. Reddy, and J. L. Bernstein, *J. Chem. Phys.* **42**, 3957 (1965).
- [17] T. Arima, D. Higashiyama, Y. Kaneko, J. P. He, T. Goto, S. Miyasaka, T. Kimura, K. Oikawa, T. Kamiyama, R. Kumai, *et al.*, *Phys. Rev. B* **70**, 064426 (2004).

- [18] L. D. Barron, *Chirality* **24**, 879 (2012).
- [19] S. Hayami and H. Kusunose, *J. Phys. Soc. Jpn.* **87**, 033709 (2018).
- [20] T. Kimura, T. Goto, H. Shintani, K. Ishizaka, T.-h. Arima, and Y. Tokura, *Nature* **426**, 55 (2003).
- [21] M. Kenzelmann, A. B. Harris, S. Jonas, C. Broholm, J. Schefer, S. B. Kim, C. L. Zhang, S.-W. Cheong, O. P. Vajk, and J. W. Lynn, *Phys. Rev. Lett.* **95**, 087206 (2005).
- [22] R. Hornreich and S. Shtrikman, *Phys. Rev.* **161**, 506 (1967).
- [23] N. Hur, S. Park, P. A. Sharma, J. S. Ahn, S. Guha, and S.-W. Cheong, *Nature* **429**, 392 (2004).
- [24] Y. J. Choi, H. T. Yi, S. Lee, Q. Huang, V. Kiryukhin, and S.-W. Cheong, *Phys. Rev. Lett.* **100**, 047601 (2008).
- [25] T.-h. Arima, *J. Phys. Soc. Jpn.* **76**, 073702 (2007).
- [26] T.-h. Arima, *J. Phys. Soc. Jpn.* **80**, 052001 (2011).
- [27] H. Katsura, N. Nagaosa, and A. V. Balatsky, *Phys. Rev. Lett.* **95**, 057205 (2005).
- [28] L. D. Barron, *Molecular light scattering and optical activity*, Cambridge University Press, Cambridge (2009).
- [29] I. Kézsmárki, N. Kida, H. Murakawa, S. Bordács, Y. Onose, and Y. Tokura, *Phys. Rev. Lett.* **106**, 057403 (2011).
- [30] M. Saito, K. Taniguchi, and T.-h. Arima, *J. Phys. Soc. Jpn.* **77**, 013705 (2008).
- [31] S. Toyoda, N. Abe, S. Kimura, Y. H. Matsuda, T. Nomura, A. Ikeda, S. Takeyama, and T. Arima, *Phys. Rev. Lett.* **115**, 267207 (2015).
- [32] S. Toyoda, N. Abe, and T. Arima, *Phys. Rev. B* **93**, 201109 (2016).
- [33] S. Toyoda, N. Abe, and T. Arima, *Phys. Rev. Lett.* **123**, 077401 (2019).
- [34] V. Baltz, A. Manchon, M. Tsoi, T. Moriyama, T. Ono, and Y. Tserkovnyak, *Rev. Mod. Phys.* **90**, 015005 (2018).
- [35] A. Iyama and T. Kimura, *Phys. Rev. B* **87**, 180408 (2013).
- [36] Y. Yamasaki, H. Sagayama, T. Goto, M. Matsuura, K. Hirota, T. Arima, and Y. Tokura, *Phys. Rev. Lett.* **98**, 147204 (2007).
- [37] T. Martin and J. e. Anderson, *IEEE Trans. Magn.* **2**, 446 (1966).

- [38] T. Kosub, M. Kopte, R. Hühne, P. Appel, B. Shields, P. Maletinsky, R. Hübner, M. O. Liedke, J. Fassbender, O. G. Schmidt, *et al.*, *Nat. Commun.* **8**, 13985 (2017).
- [39] N. B. Baranova, Y. V. Bogdanov, and B. Y. Zel'Dovich, *Opt. Commun.* **22**, 243 (1977).
- [40] G. Wagnière and A. Meier, *Chem. Phys. Lett.* **93**, 78 (1982).
- [41] L. D. Barron and J. Vrbancich, *Mol. Phys.* **51**, 715 (1984).
- [42] D. Mitcov, M. Platunov, C. D. Buch, A. Reinholdt, A. R. Døssing, F. Wilhelm, A. Rogalev, and S. Piligkos, *Chem. Sci.* **11**, 8306 (2020).
- [43] G. L. J. A. Rikken and E. Raupach, *Phys. Rev. E* **58**, 5081 (1998).
- [44] G. L. J. A. Rikken and E. Raupach, *Nature* **390**, 493 (1997).
- [45] C. A. Beevers and H. Lipson, *Zeitschrift für Kristallographie - Cryst. Mater.* **83**, 123 (1932).
- [46] C. Train, R. Gheorghe, V. Krstic, L.-M. Chamoreau, N. S. Ovanesyan, G. L. J. A. Rikken, M. Gruselle, and M. Verdaguer, *Nat. Mater.* **7**, 729 (2008).
- [47] J. H. Jung, M. Matsubara, T. Arima, J. P. He, Y. Kaneko, and Y. Tokura, *Phys. Rev. Lett.* **93**, 037403 (2004).
- [48] Y. F. Popov, A. M. Kadomtseva, D. V. Belov, G. P. Vorob'ev, and A. K. Zvezdin, *JETP Lett.* **69**, 330 (1999).
- [49] B. B. Van Aken, J.-P. Rivera, H. Schmid, and M. Fiebig, *Nature* **449**, 702 (2007).
- [50] E. Ressouche, M. Loire, V. Simonet, R. Ballou, A. Stunault, and A. Wildes, *Phys. Rev. B* **82**, 100408 (2010).
- [51] M. Baum, K. Schmalzl, P. Steffens, A. Hiess, L. P. Regnault, M. Meven, P. Becker, L. Bohatý, and M. Braden, *Phys. Rev. B* **88**, 024414 (2013).
- [52] V. Kocsis, K. Penc, T. Rõöm, U. Nagel, J. Vít, J. Romhányi, Y. Tokunaga, Y. Taguchi, Y. Tokura, I. Kézsmárki, *et al.*, *Phys. Rev. Lett.* **121**, 057601 (2018).
- [53] N. Nakagawa, N. Abe, S. Toyoda, S. Kimura, J. Zaccaro, I. Gautier-Luneau, D. Luneau, Y. Kousaka, A. Sera, M. Sera, *et al.*, *Phys. Rev. B* **96**, 121102 (2017).
- [54] M. O. Yokosuk, H.-S. Kim, K. D. Hughey, J. Kim, A. V. Stier, K. R. O'Neal, J. Yang, S. A. Crooker, K. Haule, S.-W. Cheong, *et al.*, *npj Quantum Mater.* **5**, 20 (2020).
- [55] W. F. Brown Jr, S. Shtrikman, and D. Treves, *J. Appl. Phys.* **34**, 1233 (1963).
- [56] G. Shirane, S. J. Pickart, and Y. Ishikawa, *J. Phys. Soc. Jpn.* **14**, 1352 (1959).

- [57] H. Yamauchi, H. Hiroyoshi, M. Yamada, H. Watanabe, and H. Takei, *J. Magn. Magn. Mater.* **31**, 1071 (1983).
- [58] B. N. Brockhouse, *J. Chem. Phys.* **21**, 961 (1953).
- [59] T. R. McGuire, E. J. Scott, and F. H. Grannis, *Phys. Rev.* **102**, 1000 (1956).
- [60] T. Sato, N. Abe, S. Kimura, Y. Tokunaga, and T.-h. Arima, *Phys. Rev. Lett.* **124**, 217402 (2020).
- [61] A. S. Zimmermann, D. Meier, and M. Fiebig, *Nat. Commun.* **5**, 4796 (2014).
- [62] J. G. Cherian, T. D. Tokumoto, H. Zhou, E. S. Choi, and S. A. McGill, *Phys. Rev. B* **87**, 214411 (2013).
- [63] D. R. Huffman, R. L. Wild, and M. Shinmei, *J. Chem. Phys.* **50**, 4092 (1969).
- [64] V. Grasso, S. Santangelo, and M. Piacentini, *Sol. Stat. Ion.* **20**, 9 (1986).
- [65] A. Nogami, T. Suzuki, and T. Katsufuji, *J. Phys. Soc. Jpn.* **77**, 115001 (2008).
- [66] Y. Tanabe and S. Sugano, *J. Phys. Soc. Jpn.* **9**, 766 (1954).
- [67] M. Atzori, H. Ludowieg, Á. Valentín-Pérez, M. Cortijo, I. Breslavetz, K. Paillot, P. Rosa, C. Train, J. Autschbach, E. A. Hillard, *et al.*, *Sci. Adv.* **7**, eabg2859 (2021).
- [68] M. Bode, E. Y. Vedmedenko, K. Von Bergmann, A. Kubetzka, P. Ferriani, S. Heinze, and R. Wiesendanger, *Nat. Mater.* **5**, 477 (2006).
- [69] P. Schoenherr, L. M. Giraldo, M. Lilienblum, M. Trassin, D. Meier, and M. Fiebig, *Materials* **10**, 1051 (2017).
- [70] P. Appel, B. J. Shields, T. Kosub, N. Hedrich, R. Hubner, J. Faßbender, D. Makarov, and P. Maletinsky, *Nano Lett.* **19**, 1682 (2019).
- [71] P. G. Evans, E. D. Isaacs, G. Aeppli, Z. Cai, and B. Lai, *Science* **295**, 1042 (2002).
- [72] H. Ueda, Y. Tanaka, Y. Wakabayashi, and T. Kimura, *Phys. Rev. B* **98**, 134415 (2018).
- [73] S. A. Werner, A. Arrott, and H. Kendrick, *Phys. Rev.* **155**, 528 (1967).
- [74] W. L. Roth, *J. Appl. Phys.* **31**, 2000 (1960).
- [75] M. Fiebig, D. Fröhlich, G. Sluyterman v. L, and R. V. Pisarev, *Appl. Phys. Lett.* **66**, 2906 (1995).
- [76] K. Kimura, T. Katsuyoshi, Y. Sawada, S. Kimura, and T. Kimura, *Commun. Mater.* **1**, 39 (2020).

- [77] M. Fiebig, D. Fröhlich, B. B. Krichevtsov, and R. V. Pisarev, *Phys. Rev. Lett.* **73**, 2127 (1994).
- [78] M. Fiebig, T. Lottermoser, D. Fröhlich, A. V. Goltsev, and R. V. Pisarev, *Nature* **419**, 818 (2002).
- [79] T. Hoffmann, P. Thielen, P. Becker, L. Bohatý, and M. Fiebig, *Phys. Rev. B* **84**, 184404 (2011).
- [80] M. Matsubara, S. Manz, M. Mochizuki, T. Kubacka, A. Iyama, N. Aliouane, T. Kimura, S. L. Johnson, D. Meier, and M. Fiebig, *Science* **348**, 1112 (2015).
- [81] K. Kimura, M. Toyoda, P. Babkevich, K. Yamauchi, M. Sera, V. Nassif, H. M. Rønnow, and T. Kimura, *Phys. Rev. B* **97**, 134418 (2018).
- [82] R. H. Wade, *Proc. Phys. Soc.* **79**, 1237 (1962).
- [83] E. Fatuzzo, *Phys. Rev.* **127**, 1999 (1962).
- [84] E. Fatuzzo and W. J. Merz, *Phys. Rev.* **116**, 61 (1959).
- [85] M. Avrami, *J. Chem. Phys.* **8**, 212 (1940).
- [86] M. Labrune, S. Andrieu, F. Rio, and P. Bernstein, *J. Magn. Magn. Mater.* **80**, 211 (1989).
- [87] M. Baum, J. Leist, T. Finger, K. Schmalzl, A. Hiess, L. P. Regnault, P. Becker, L. Bohatý, G. Eckold, and M. Braden, *Phys. Rev. B* **89**, 144406 (2014).
- [88] S. Biesenkamp, D. Gorkov, W. Schmidt, K. Schmalzl, Y. Sidis, P. Becker, L. Bohatý, and M. Braden, *Phys. Rev. B* **104**, 174405 (2021).
- [89] J. Stein, S. Biesenkamp, T. Cronert, T. Fröhlich, J. Leist, K. Schmalzl, A. C. Komarek, and M. Braden, *Phys. Rev. Lett.* **127**, 097601 (2021).
- [90] K. Taniguchi, N. Abe, T. Takenobu, Y. Iwasa, and T. Arima, *Phys. Rev. Lett.* **97**, 097203 (2006).
- [91] H. Sagayama, K. Taniguchi, N. Abe, T.-h. Arima, M. Soda, M. Matsuura, and K. Hirota, *Phys. Rev. B* **77**, 220407 (2008).
- [92] K. D. Belashchenko, O. Tchernyshyov, A. A. Kovalev, and O. A. Tretiakov, *Appl. Phys. Lett.* **108**, 132403 (2016).
- [93] F. D. M. Haldane, *Phys. Rev. Lett.* **50**, 1153 (1983).
- [94] S. Lemerle, J. Ferré, C. Chappert, V. Mathet, T. Giamarchi, and P. Le Doussal, *Phys. Rev. Lett.* **80**, 849 (1998).

-
- [95] Y. Shiratsuchi, H. Yoshida, Y. Kotani, K. Toyoki, T. V. A. Nguyen, T. Nakamura, and R. Nakatani, *APL Mater.* **6**, 121104 (2018).
- [96] W. Kleemann, *Annu. Rev. Mater. Res.* **37**, 415 (2007).
- [97] A. Kirilyuk, J. Ferré, V. Grolier, J. P. Jamet, and D. Renard, *J. Magn. Magn. Mater.* **171**, 45 (1997).
- [98] W. J. Merz, *Phys. Rev.* **95**, 690 (1954).
- [99] F. Kagawa, M. Mochizuki, Y. Onose, H. Murakawa, Y. Kaneko, N. Furukawa, and Y. Tokura, *Phys. Rev. Lett.* **102**, 057604 (2009).
- [100] T. V. A. Nguyen, Y. Shiratsuchi, A. Kobane, S. Yoshida, and R. Nakatani, *J. Appl. Phys.* **122**, 073905 (2017).
- [101] V. Kocsis, Y. Tokunaga, Y. Tokura, and Y. Taguchi, *Phys. Rev. B* **104**, 054426 (2021).
- [102] S. Hayami, M. Yatsushiro, Y. Yanagi, and H. Kusunose, *Phys. Rev. B* **98**, 165110 (2018).
- [103] M. Lerch, H. Boysen, R. Neder, F. Frey, and W. Laqua, *J. Phys. Chem. Sol.* **53**, 1153 (1992).
- [104] T. Hayashida, Y. Uemura, K. Kimura, S. Matsuoka, D. Morikawa, S. Hirose, K. Tsuda, T. Hasegawa, and T. Kimura, *Nat. Commun.* **11**, 4582 (2020).